Article

Immunity

Stress induces behavioral abnormalities by increasing expression of phagocytic receptor MERTK in astrocytes to promote synapse phagocytosis

Graphical abstract

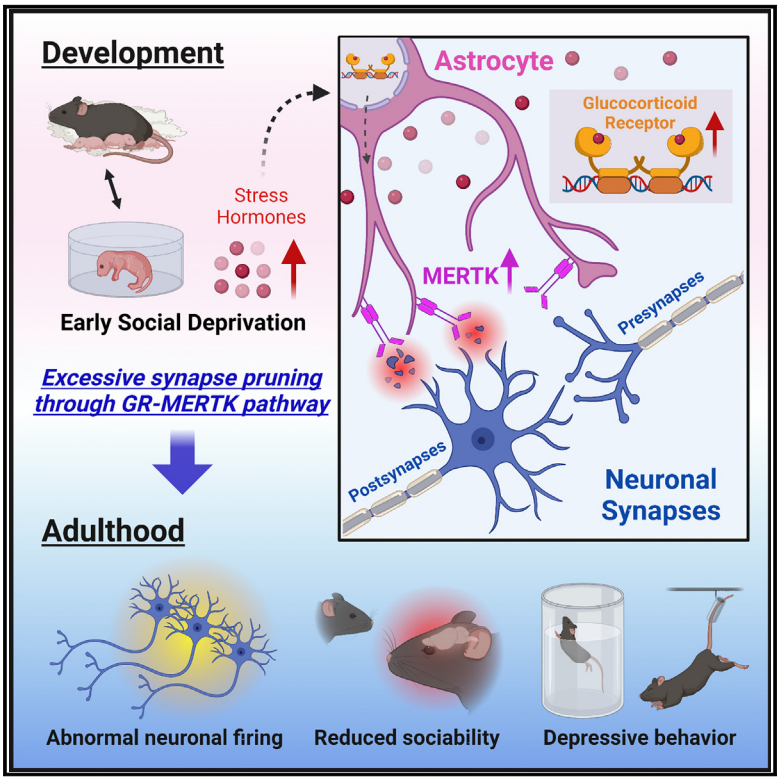

Highlights

- Stress hormones induce astrocyte-mediated phagocytosis through GR-MERTK activation
- Astrocytic GR-MERTK activation induces excitatory synapse loss in ESD model mice
- ESD model mice show abnormal behaviors with increased cortical neuronal firing
- Ablating GR-MERTK in astrocytes prevents ESD-evoked synapse loss and behavior symptoms

Authors

Youkyeong Gloria Byun, Nam-Shik Kim, Gyuri Kim, ..., Ki-Jun Yoon, Seung-Hee Lee, Won-Suk Chung

Correspondence

wonsuk.chung@kaist.ac.kr

In brief

Early social deprivation induces synaptic and behavioral deficits by unknown mechanisms. Byun et al. reveal that stress hormones induce excessive excitatory synapse elimination via the astrocytic GR-MERTK pathway. Ablating GR-MERTK from astrocytes prevents the loss of excitatory synapses, abnormal neuronal firing, and behavioral symptoms in ESD mice, emphasizing the critical roles of astrocytic phagocytosis in brain physiology and animal behavior.

Byun et al., 2023, Immunity *56*, 2105–2120
September 12, 2023 © 2023 The Authors. Published by Elsevier Inc.
https://doi.org/10.1016/j.immuni.2023.07.005

CellPress

Immunity

CellPress
OPEN ACCESS

Article

Stress induces behavioral abnormalities by increasing expression of phagocytic receptor MERTK in astrocytes to promote synapse phagocytosis

Youkyeong Gloria Byun,[1,2,5] Nam-Shik Kim,[1,2,5] Gyuri Kim,[1,2,5] Yi-Seon Jeon,[1,3] Jong Bin Choi,[1,2,4] Chan-Woo Park,[1,2] Kyungdeok Kim,[1,3] Hyunsoo Jang,[1,2] Jinkyeong Kim,[1,3] Eunjoon Kim,[1,3] Yong-Mahn Han,[1,2,4] Ki-Jun Yoon,[1,2] Seung-Hee Lee,[1,3] and Won-Suk Chung[1,2,6,*]

[1]Department of Biological Sciences, Korea Advanced Institute of Science and Technology, Daejeon 34141, Republic of Korea
[2]KAIST Stem Cell Center, Korea Advanced Institute of Science and Technology, Daejeon 34141, Republic of Korea
[3]Center for Synaptic Brain Dysfunctions, Institute for Basic Science, Korea Advanced Institute of Science and Technology, Daejeon 34141, Republic of Korea
[4]Graduate School of Medical Science and Engineering, KAIST, Daejeon 34141, Republic of Korea
[5]These authors contributed equally
[6]Lead contact
*Correspondence: wonsuk.chung@kaist.ac.kr
https://doi.org/10.1016/j.immuni.2023.07.005

SUMMARY

Childhood neglect and/or abuse can induce mental health conditions with unknown mechanisms. Here, we identified stress hormones as strong inducers of astrocyte-mediated synapse phagocytosis. Using *in vitro*, *in vivo*, and human brain organoid experiments, we showed that stress hormones increased the expression of the *Mertk* phagocytic receptor in astrocytes through glucocorticoid receptor (GR). In post-natal mice, exposure to early social deprivation (ESD) specifically activated the GR-MERTK pathway in astrocytes, but not in microglia. The excitatory post-synaptic density in cortical regions was reduced in ESD mice, and there was an increase in the astrocytic engulfment of these synapses. The loss of excitatory synapses, abnormal neuronal network activities, and behavioral abnormalities in ESD mice were largely prevented by ablating GR or MERTK in astrocytes. Our work reveals the critical roles of astrocytic GR-MERTK activation in evoking stress-induced abnormal behaviors in mice, suggesting GR-MERTK signaling as a therapeutic target for stress-induced mental health conditions.

INTRODUCTION

Individuals who experience childhood abuse and emotional neglect are much more likely to develop various mental health conditions, such as depression and schizophrenia, later in life.[1,2] Although multiple factors can be involved in this process, recent studies have shown that abnormal synapse loss and neural circuit wiring are frequently observed in the individuals living with mental health conditions.[3–5] However, the underlying mechanisms by which early-life stress induces synaptic and behavioral deficits are not fully understood.

Previously, we showed that astrocytes, the most abundant cells in the brain, express various phagocytic receptors, including *Megf10* and *Mertk*.[6] *Megf10* is a homolog of drosophila Draper, which plays essential roles in the phagocytosis of degenerating axons,[7] apoptotic cells,[8] and synapses,[9] while *Mertk* is a member of the TAM (*Tyro3*, *Axl*, and *Mertk*) tyrosine kinase receptor family, which recognizes phosphatidylserine as an "eat-me" signal through bridging molecules, such as *Gas6* and *Pros1* in initiating phagocytosis of apoptotic cells.[10] By recognizing and eliminating redundant synaptic connections from retinal ganglia cells through MEGF10 and MERTK phagocytic receptors, astrocytes are shown to play an active role in remodeling developmental neural circuits in response to neural activity.[6]

After this initial finding in the developing retinogeniculate system, we have also recently revealed that astrocytes and microglia play distinct roles in eliminating excitatory versus inhibitory synapses in the adult brains. First, by developing adeno-associated virus (AAV)-based synapse phagocytosis reporters, we showed that astrocytes constantly eliminate unnecessary excitatory synaptic connections in the adult hippocampus through *Megf10* and that this astrocytic function is critical for the homeostasis of circuit connectivity important for cognitive functions.[11] Second, by manipulating phosphatidylserine exposure in mature neurons through deleting *Cdc50a*, an upstream modulator of flippase, we showed that microglia have the capacity to control the number of inhibitory synapses by eliminating them through MERTK-dependent phagocytosis.[12] CDC50A deletion induces phosphatidylserine exposure preferentially in neuronal soma, thereby specifically inducing engulfment of

This is an open access article under the CC BY license (http://creativecommons.org/licenses/by/4.0/).

inhibitory post-synapses from soma and proximal dendrites by microglial phagocytosis, without affecting excitatory synapses. Thus, our studies indicate that mechanisms of synapse elimination can be distinct depending on which glial cells participate in the process. Revealing these distinct roles of glia-mediated synapse elimination in various neural circuits during development and diseased conditions would be important not only for understanding the basic mechanisms of synapse remodeling but also for developing therapeutic strategies for modulating synapse elimination.

In this work, we discovered that glucocorticoids, the stress hormones, enhance astrocytic phagocytosis. Treating glucocorticoid receptor (GR) antagonists or deleting MERTK in cultured astrocytes effectively blocks glucocorticoid-induced astrocytic phagocytosis, indicating that GR-induced MERTK transcriptional activation is responsible for this process. By adapting early social deprivation (ESD) mouse model to mimic childhood stress condition, we found that the expression of astrocytic GR and MERTK as well as the amount of LAMP2^{+} lysosomes in astrocytes were highly increased under ESD condition in various cortical regions. Furthermore, we observed that astrocytes in ESD mice engulf much more PSD95-positive synapses on GABAergic neurons, resulting in the decreased excitatory synaptic density as well as the excitatory-inhibitory imbalance. The loss of excitatory synapses, abnormal neuronal network activities, and behavioral phenotypes in ESD mice were substantially prevented by either ablating MERTK or GR specifically from astrocytes. Overall, our work shows that stress hormones activate excessive excitatory synapse elimination by MERTK-mediated astrocytic phagocytosis. This work also suggests that GR-MERTK signaling pathway can be modulated as a potential therapeutic target for the brain disorders induced by stress.

RESULTS

Stress hormones induce phagocytosis by cultured astrocytes

To identify factors that control astrocytic phagocytosis, we assessed the effects of 2,261 FDA-approved clinical compounds on astrocytic uptake of synaptosomes by utilizing an *in vitro* live imaging phagocytosis assay (Figure S1A).[6,13] In this assay, we measured phagocytic index by quantifying the area of bright red fluorescence emitted from phagocytosed pH-sensitive dye (pHrodo red, succinimidyl ester)-conjugated synaptosomes (pHrodo-Syns) normalized to the area of astrocytes. Following three independent experiments, we identified 38 and 15 out of 2,261 compounds that enhanced and suppressed astrocytic phagocytosis, respectively (Figures 1A and 1A′; Table S1).

Among the compounds that enhanced astrocytic phagocytosis, we found that 32% of them were synthetic glucocorticoids (Figures 1A and 1A′). Glucocorticoids are stress hormones secreted from the adrenal glands upon stressful events. These stress hormones travel through the bloodstream and regulate various cellular responses by binding to stress hormone receptors, such as mineralocorticoid receptor (MR) and GR, which can function as transcription factors upon ligand binding.[14,15] To validate our screening results and investigate which receptor is responsible for stress-hormone-induced astrocytic phagocytosis, we treated cultured rat astrocytes, which were purified using the immunopanning method,[16] with the MR-specific antagonist eplerenone or GR-specific antagonist mifepristone in the presence of corticosterone. This experiment showed that mifepristone substantially blocked corticosterone-induced astrocytic phagocytosis, to the similar phagocytic index level of the control group (Figures 1B and 1C).

To determine how corticosterone-induced GR activation affects the expression of genes related to phagocytosis in astrocytes, we measured the changes in the mRNA expression of GR (*Nr3c1*), MR (*Nr3c2*), lysosome biogenesis gene, transcription factor EB (*Tfeb*) as well as various phagocytic receptors known to be expressed in astrocytes after treatment of corticosterone with or without mifepristone.[17] The mRNA expression of the GR and MR was transiently decreased upon corticosterone treatment, as previously reported,[18] and this effect was effectively blocked by mifepristone treatment (Figure S1B). However, *Tfeb* expression was not changed upon corticosterone or mifepristone treatment (Figure S1B).

In contrast, we found that the *Mertk* mRNA was highly increased 24 h after corticosterone treatment (Figure S1C) and remained high at 48 h (Figure 1D). Furthermore, cotreatment of GR antagonist, mifepristone with corticosterone normalized the corticosterone-induced upregulation of *Mertk* mRNA expression (Figures 1D and S1C). The mRNAs of other phagocytic receptors, such as *Megf10* and *Axl*, were not changed upon either corticosterone treatment or corticosterone and GR antagonist cotreatment (Figures 1D and S1C), suggesting that the phagocytic receptor, MERTK, rather than MEGF10 or AXL, is a major contributor for active astrocytic phagocytosis initiated by corticosterone treatment. Indeed, we applied corticosterone to cultured *Mertk* and *Megf10* knockout (KO) astrocytes purified from the cortices of *Mertk*$^{-/-}$ and *Megf10*$^{-/-}$ mice and found that corticosterone failed to induce phagocytic capacity in *Mertk*$^{-/-}$ astrocytes (Figure 1E), but not in *Megf10*$^{-/-}$ astrocytes (Figure S1D). Conversely, we overexpressed MERTK in purified astrocytes with a lentivirus (LV) encoding *GfaABC$_1$D* promoter (a truncated version of *Gfap* promoter)-driven MERTK-IRES-ZsGreen (Figures 1F, 1G, and S1E). This experiment showed that MERTK overexpression was sufficient to increase the synaptosome uptake by astrocytes in the DMSO control and abrogate the effects of corticosterone as well as GR antagonist treatments (Figures 1H and S1F), suggesting that corticosterone and GR induce phagocytosis of astrocytes through MERTK. Although it is not well understood how the MERTK expression in astrocytes is regulated[19], studies have shown that it is upregulated in microglia during stroke[20,21] and Alzheimer's diseases.[22] Previous reports also showed that GR can regulate *Mertk* expression in monocyte-derived macrophages and dendritic cells,[23–25] consistent with our findings.

Stress hormones induce astrocyte-mediated synapse elimination in ESD model mice

Stress has been shown to elicit a decrease in the number of excitatory synaptic connections and impair their functions.[26] Although this effect can result from defects in synaptic remodeling and turnover, the potential roles of glial cells in early-life-stress-induced synaptic loss have not been adequately investigated. To test our hypothesis that stress triggers excessive synaptic

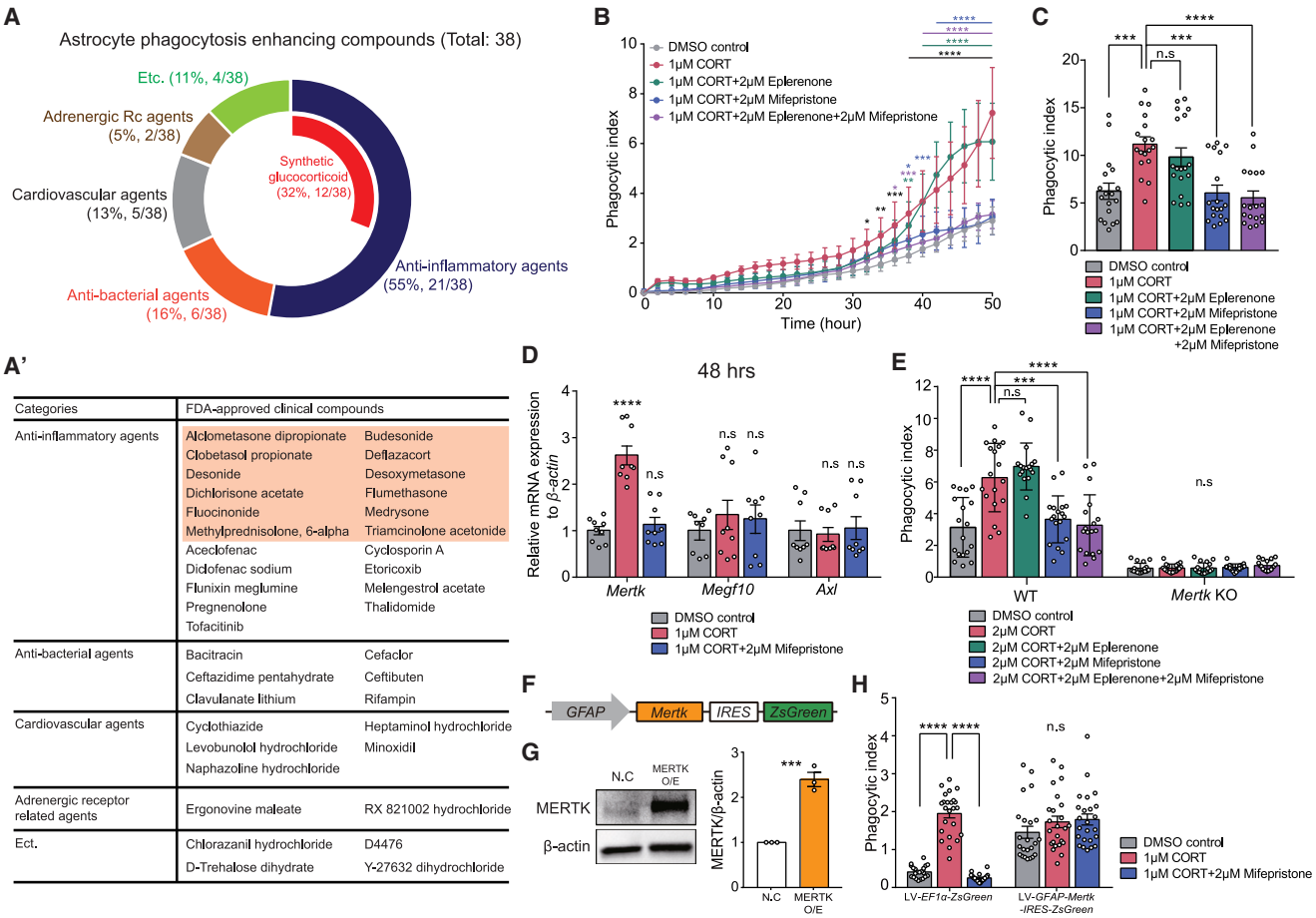

Figure 1. Stress hormones enhance astrocytic phagocytosis through the GR-MERTK pathway *in vitro*

(A and A') The circle graph (A) and table (A') showing the categorized compounds that enhance astrocytic phagocytosis of pHrodo-Syns. The red box (A') indicates the list of synthetic glucocorticoids.

(B) A representative graph showing the live uptake kinetics of pHrodo-Syns after pretreatment with corticosterone (CORT) along with a GR antagonist (mifepristone) and/or a MR antagonist (eplerenone). The phagocytic index was calculated by measuring the total area of engulfed pHrodo-Syns normalized to the astrocytic area in the imaging fields.

(C) Bar graphs showing the phagocytic index of rat astrocytes 50 h after pHrodo-Syns application and pretreatment with CORT along with mifepristone and/or eplerenone.

(D) Quantitative PCR data showing the mRNA of phagocytic receptors (*Mertk*, *Megf10*, and *Axl*) in cultured rat astrocytes treated with CORT and mifepristone along with pH-Syns for 48 h.

(E) Bar graphs showing the phagocytic index of WT and *Mertk*$^{-/-}$ mouse astrocytes treated with CORT along with mifepristone and/or eplerenone for 40 h.

(F) Schematic illustration of the LV vector for overexpressing *Mertk* in astrocytes.

(G) Western blot images and bar graphs showing the MERTK protein expression (n = 3 and 3).

(H) Bar graphs showing the phagocytic index of astrocytes infected with either control or *Mertk* overexpression LV 60 h after pHrodo-Syns application and pretreatment with CORT with or without mifepristone.

7- to 10-day-old male and female littermates were used. (C–E and H) Representative data from three or four independent experiments. Six data points were obtained from each independent experiment.

Data are shown as mean ± SEM. ***p < 0.001, ****p < 0.0001, ns, non-significant (p > 0.05); one-way ANOVA with Tukey's multiple comparisons test and two-way ANOVA with Tukey's multiple comparisons test (B). See also Figure S1 and Table S1.

loss through activation of the astrocytic GR-MERTK pathway, we utilized a mouse model of ESD by separating newborn pups from their dams.[27] This protocol can disrupt maternal-infant social bonding and induce stress responses during the early post-natal period (Figure 2A).

First, to assess the changes in phagocytic events by astrocytes in ESD model mice, we examined the amount of LAMP2^{+} lysosomes in astrocytes in various brain regions, including areas that were previously implicated in stress-mediated behavior changes.[28] We found that in the brains of post-natal day 14 (P14) ESD model mice, the amount of LAMP2^{+} lysosomes in astrocytes was highly increased in specific cortical regions, including the somatosensory cortex (SSC), dysgranular zone of the primary somatosensory cortex (S1DZ), primary motor cortex (M1), dorsal agranular insular cortex (AID), and lateral orbital and ventral orbital cortex (LO and VO) (Figures 2B, 2C, and S2A). In

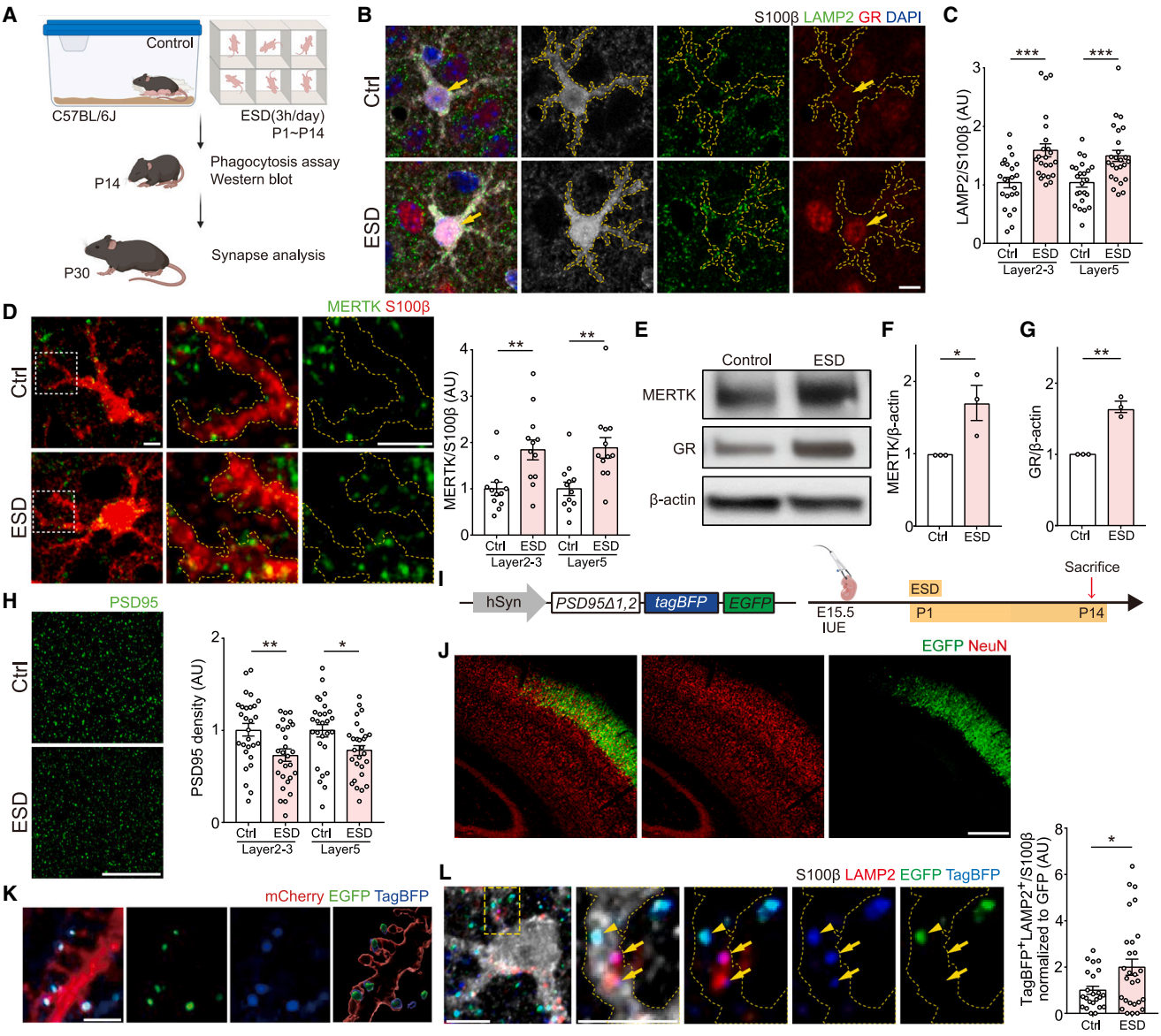

Figure 2. Stress hormones induce excitatory synapse loss by astrocytic phagocytosis

(A) Schematic illustration of the ESD experiments.

(B) Representative confocal z stack images of GR (red, yellow arrow), lysosomes (LAMP2, green), and DAPI (blue) in astrocytes (S100β, white) from the SSCs of control and ESD model mice. The yellow dotted lines outline astrocytes. Scale bars, 10 μm.

(C) Bar graphs showing the amount of lysosomes in astrocytes in layers 2, 3, and 5 of the SSC in control and ESD model mice (n = 7 and 7).

(D) Representative confocal z stack (left) and magnified images of MERTK (green) in astrocytes (S100β, red) from the SSCs of control and ESD model mice. The yellow dotted lines outline magnified astrocytic processes in the white dotted boxes. Bar graphs showing MERTK expression in astrocytes in layers 2, 3, and 5 of the SSC in ESD model mice (n = 3 and 3). Scale bars, 5 μm.

(E–G) Western blot images (E) and bar graphs (F: MERTK, G: GR) showing MERTK and GR protein expression in astrocytes purified from control and ESD mouse cortices (n = 3 and 3).

(H) Representative confocal z stack images and bar graphs showing the PSD95 density in the SSCs of control and ESD model mice (n = 7 and 7). Scale bars, 10 μm.

(I) Schematic illustration of the IUE and ESD experiments using the synapse elimination reporter.

(J) Representative single-plane images showing layers 2 and 3 of the SSC labeled with hSyn-PSD95Δ1,2-tagBFP-EGFP (green) costained with NeuN (red) in P14 mice after IUE. Scale bars, 1,000 μm.

(K) Representative confocal z stack and 3D reconstructed images showing PSD95Δ1,2-tagBFP-EGFP (blue and green) in the tips of dendritic spines (mCherry, red). Scale bars, 2.5 μm.

(L) Representative confocal z stack (left) and magnified images showing phagocytosed PSD95Δ1.2-tagBFP-EGFP^{+} puncta (TagBFP alone: blue, yellow arrows; TagBFP^{+}EGFP^{+}: blue + green, yellow arrowheads) in astrocytes (S100β, white) costained with LAMP2 (red). The yellow dotted lines outlined the magnified

(legend continued on next page)

contrast, except for the dorsal lateral geniculate nucleus (dLGN) and dentate gyrus (DG), there were no significant changes in the phagocytic activity of astrocytes in other brain regions including the medial prefrontal cortex (anterior cingulate cortex [ACC] and prelimbic and infralimbic cortex [PrL and IL]), hippocampus (CA1), striatum, bed nucleus of the stria terminals (BNSTs), lateral septum and periventricular nucleus of the thalamus (PVT) after ESD (Figure S2A), indicating that there are regional differences in ESD-induced astrocytic responses in the early post-natal brain. In particular, astrocytes in cortical regions, such as the SSC, were more susceptible to ESD-induced lysosomal activation than those in other brain regions, therefore we further characterized the glial responses in the SSC after ESD.

We found that a significant amount of GR protein was translocated to the astrocytic nucleus in ESD model mice (Figure 2B, yellow arrow). In astrocytes in which GR was activated, the localization of the MERTK protein and the amount of lysosomes were highly increased (Figures 2B–2D). To further validate the increase in the amount of GR and MERTK proteins in astrocytes after ESD, we performed western blotting using astrocytes purified from the cortices of P14 control and ESD model mice and found that GR and MERTK protein were highly increased in astrocytes from ESD model mice (Figures 2E–2G). Moreover, when we measured GR and MERTK from individual astrocytes, we found positive correlation between the amount of GR and MERTK protein expression in astrocytes (Figure S2B).

Next, to determine whether ESD-induced astrocytic phagocytosis mediates abnormal synaptic loss during developmental synaptic pruning, we measured the excitatory and inhibitory synaptic density in P30 control and ESD model mice. We found that the numbers of VGLUT1$^+$ excitatory pre-synapse, VGAT$^+$ inhibitory pre-synapse, and Gephyrin$^+$ inhibitory post-synapse puncta in layers 2 and 3 and layer 5 of the SSC were not different between ESD model mice and control mice (Figure S2C). However, the number of PSD95$^+$ excitatory post-synapse puncta was substantially reduced in both layers 2 and 3 and layer 5 of the SSC in ESD model mice (Figure 2H).

To directly observe and compare excitatory synapse phagocytosis by astrocytes after ESD, we utilized our previously developed synapse elimination reporter with minor modifications.[11] The reporter vector encodes PSD95Δ1,2 (PSD95 that has a deletion of PDZ, PSD95 [post synaptic density protein 95], DlgA [Drosophila disc large tumor suppressor], and zo-1 [zonula occludens-1 protein], domain)-tagBFP-EGFP driven by the human Synapsin (hSyn) promoter (Figure 2I),[29,30] which utilizes different pKa values of tagBFP and EGFP (e.g., tagBFP fluorescence is preserved while the EGFP signal is lost in low-pH lysosomes). After inducing the expression of the reporter in the SSCs of embryonic day (E) 15.5 mice by *in utero* electroporation (IUE), the mice were subjected to ESD, and the degree of synapse engulfment by astrocytes at P14 was analyzed (Figure 2I). In the *in utero* electroporated mice, we observed that the transduced post-synaptic proteins were well localized in the tips of dendritic spines in layers 2 and 3 of the SSC (Figures 2J and 2K). When we examined TagBFP$^+$ synaptic puncta originating from excitatory post-synapses on hSyn$^+$ neurons, we found that the amount of tagBFP alone puncta inside astrocytic lysosomes was highly increased in the SSC from ESD model mice compared with control mice (Figure 2L), demonstrating that ESD induces excessive excitatory synapse phagocytosis by astrocytes.

Although we utilized S100 calcium-binding protein beta (S100β) as a marker for astrocytes,[31] S100β is also expressed in oligodendrocyte precursor cells (OPCs), which has been shown to possess phagocytic capacity.[32] To exclude this possibility, we quantified the amount of lysosomes in S100β$^+$ OPCs by co-staining with LAMP2 and neuron-glial antigen 2 (NG2), another OPC marker. We found that 12.7% of S100β$^+$ cells were NG2$^+$ OPCs (Figure S2D). However, the amount of lysosomes in NG2$^+$S100β$^+$ OPCs was not changed under ESD condition compared with control (Figure S2E), indicating that the increased phagocytosis of excitatory post-synapses by S100β$^+$ cells was due to astrocytes.

Chronic stress in adulthood has been shown to induce brain inflammation along with reactive gliosis and changes in glial function.[33,34] However, we found no signs of reactive gliosis after ESD, as measured by immunostaining of reactive astrocytes and microglia with GFAP and IBA1, respectively (Figures S2F and S2G). Microglia has been also known to participate in synapse elimination during post-natal brain development.[35,36] However, in microglia, the amount of CD68$^+$ lysosomes and MERTK expression were not different between ESD model mice and control mice (Figures S2H and S2I). We also found that the amount of engulfed PSD95$^+$ puncta inside microglial lysosomes was unchanged upon ESD (Figure S2J). Lastly, to identify why microglial phagocytosis was unaffected upon ESD, we measured GR in the microglial nucleus and found that the amount of microglial GR in control as well as ESD mice was much lower than those of astrocytes (Figure S2K), suggesting that ESD-induced excessive glial phagocytosis is mostly mediated by astrocytes but not by microglia due to the low GR expression in microglia.

Stress hormones induce astrocyte-mediated synapse elimination in human brain organoids

Next, to investigate whether our findings can be applied to human astrocytes, we treated 320-day-old human cortical organoids (hCOs), which have been reported to closely mimic the neo-natal human brain (Figure 3A),[37] with cortisol. We found that cortisol treatment for a week upregulated GR in astrocytes (Figure 3B) as well as MERTK protein expression in hCOs, as measured by western blotting and immunohistochemistry (IHC) (Figures 3C, 3D, and 3H). However, consistent with our data (Figures 1D and S1C), the MEGF10 and AXL expression in the hCOs were not changed after cortisol treatment (Figures 3C, 3E, and 3F). Moreover, we found that both the amounts of LAMP2$^+$ lysosomes in astrocytes and PSD95$^+$ synaptic puncta engulfed by astrocytes were highly increased (Figures 3I–3K)

astrocytic processes in the yellow dotted boxes. Bar graphs showing the amount of tagBFP alone puncta in astrocytic lysosomes in control and ESD model mice (n = 4 and 5). Scale bars, 5 μm.

(B–D) 14-day-old and (H) 30-day-old male littermates were used. (E–G and I–L) 14-day-old male and female littermates were used. (C, D, H, and L) n values represent the number of mice per each group. Four data points were obtained from each mouse, and outliers were removed. Data are shown as mean ± SEM. *p < 0.05, **p < 0.005, ***p < 0.001, ns, non-significant (p > 0.05); unpaired t test and two-way ANOVA with Sidak's multiple comparisons test. See also Figure S2.

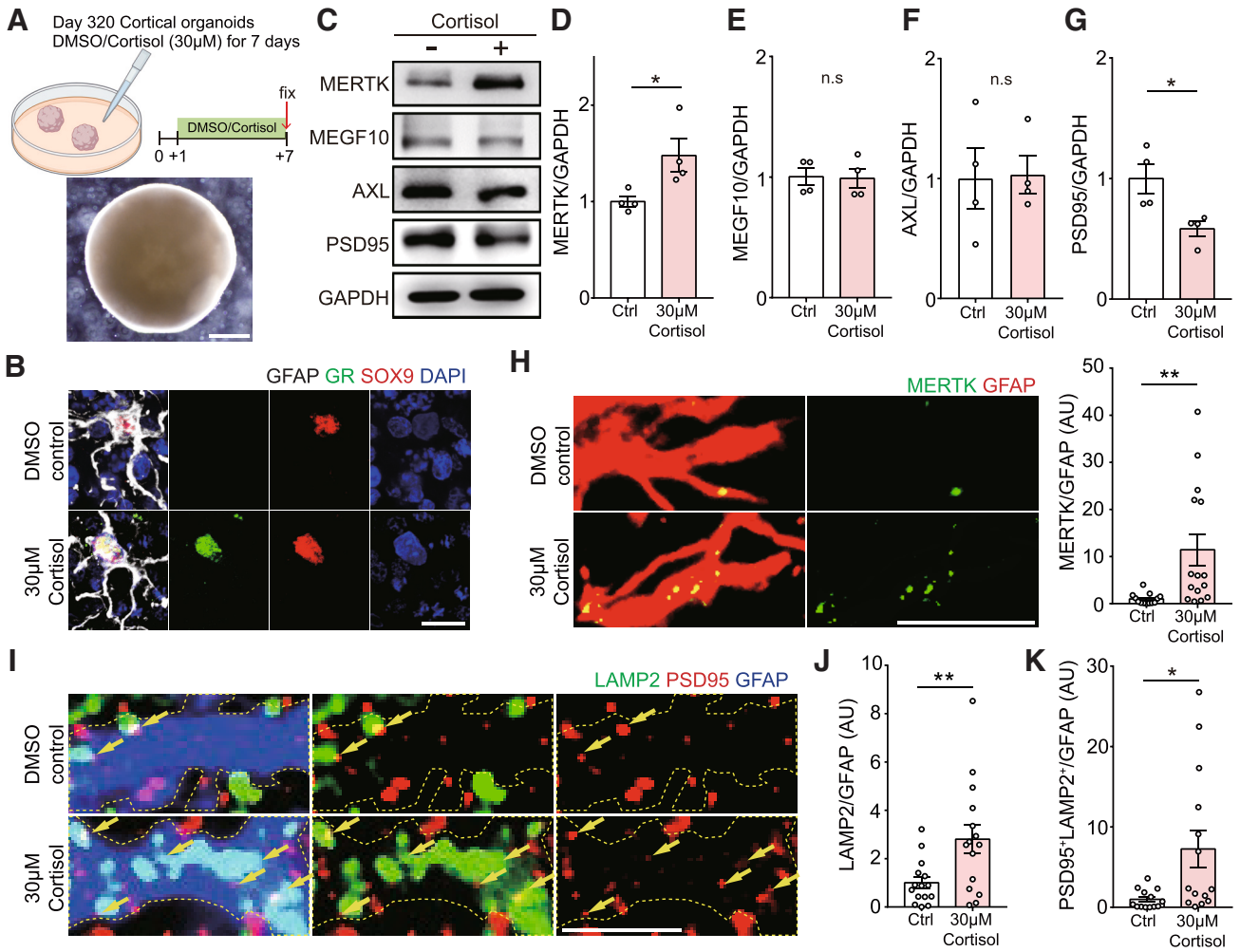

Figure 3. Stress hormones induce excitatory synapse loss in human brain organoids

(A) Schematic illustration of the experiments in which human cortical organoids (hCOs) were treated with cortisol. Scale bars, 200 μm.

(B) Representative confocal z stack images showing GR (green) activation in nucleus (Sox9, red) of astrocyte (GFAP, white) in cortisol-treated hCOs costained with DAPI (blue). Scale bars, 10 μm.

(C–G) Western blot images (C) and bar graphs (D: MERTK, E: MEGF10, F: AXL, and G: PSD95) showing the expression of phagocytic receptors and PSD95 in control and cortisol-treated hCOs (n = 4 and 4).

(H) Representative confocal z stack images and bar graphs showing MERTK (green) expression in control and hCOs astrocytes (GFAP, red) (n = 4 and 4). Scale bars, 1 μm.

(I) Representative confocal z stack images showing phagocytosed PSD95^{+} synapses (red, yellow arrows) in lysosomes (LAMP2, green) in DMSO-treated and cortisol-treated hCO astrocytes (GFAP, blue). The yellow dotted lines outline astrocytic processes. Scale bars, 5 μm.

(J) Bar graphs showing the amount of lysosomes in control and cortisol-treated hCO astrocytes (n = 4 and 4).

(K) Bar graphs showing the amount of phagocytosed PSD95^{+} synapse puncta inside astrocytic lysosomes (n = 4 and 4).

(H–J) n values represent the number of hCOs per group. Four data points were obtained from each hCO, and outliers were removed.

Data are shown as mean ± SEM. *p < 0.05, **p < 0.005, ***p < 0.001; unpaired t test.

and global PSD95 protein expression was conversely decreased (Figures 3C and 3G) in cortisol-treated hCOs. These results indicate that the effects of stress hormones in inducing excessive synapse elimination by astrocytes can be conserved between rodents and humans.

Astrocytic GR activation induces ESD-mediated synapse elimination

To genetically prove our hypothesis that astrocytic GR is responsible for ESD-induced synaptic loss, we generated astrocyte-specific inducible GR conditional KO (AGR cKO) mice by crossing *Aldh1l1-creERT2* mice with *loxP*-floxed *Nr3c1* (*Nr3c1$^{f/f}$*) mice. Then, we eliminated astrocytic GR by injecting 4-hydroxy tamoxifen (4-OHT) into P5 pups for 3 consecutive days, and subjected Cre^{-} and Cre^{+} AGR cKO mice to ESD (Figure 4A). The IHC data showed that although ESD induced GR activation in astrocytes in the brains of Cre^{-} mice subjected to ESD, GR in astrocytes was not activated in the brains of AGR cKO mice subjected to ESD (Figures 4B and S4A).

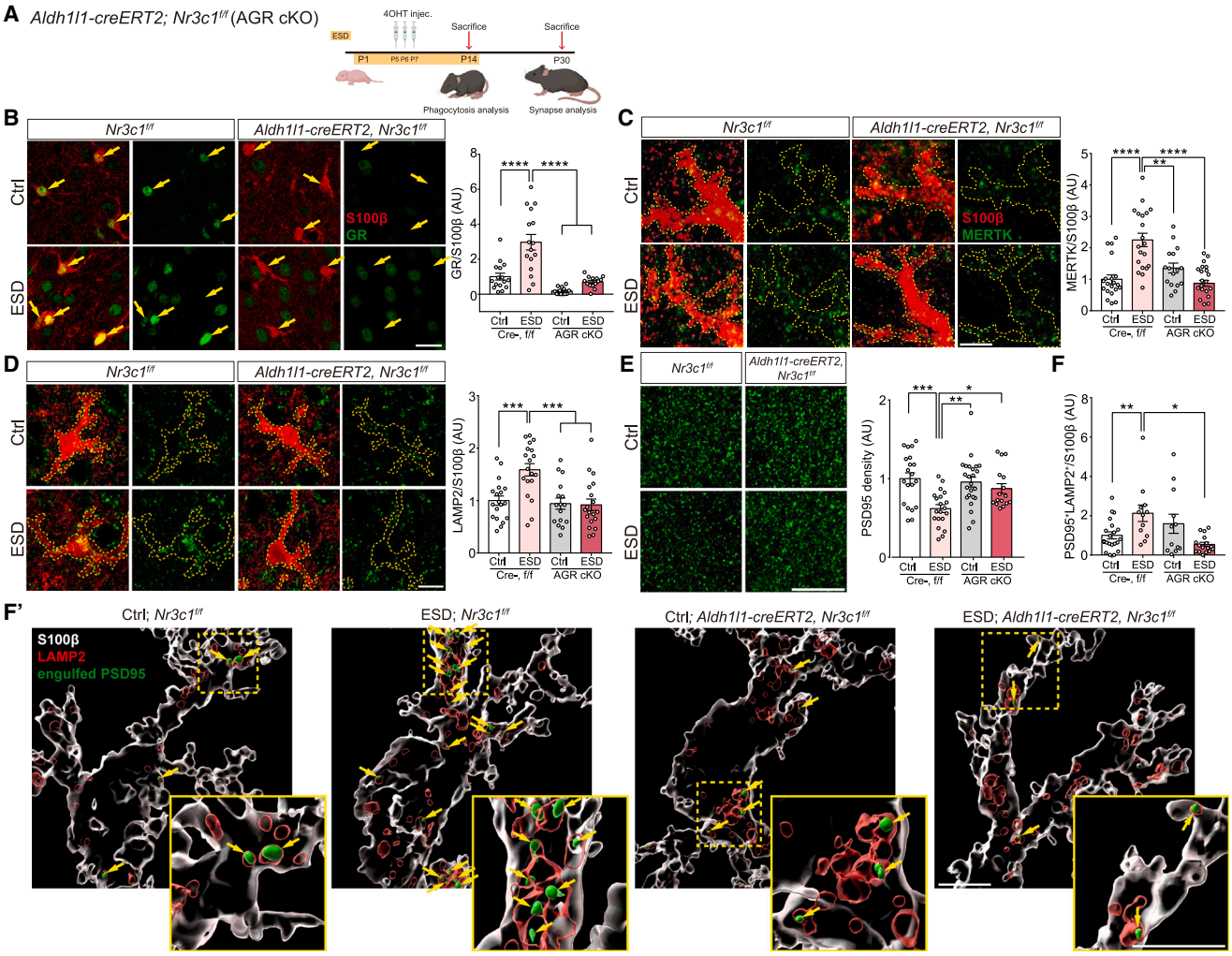

Figure 4. Astrocyte-specific GR ablation prevents ESD-induced excitatory synapse loss

(A) Schematic illustration of the ESD experiments using *Aldh1l1-creERT2; Nr3c1-flox* (AGR cKO) mice.

(B) Representative confocal z stack images of GR (green, yellow arrows) in astrocytes (S100β, red) in layers 2 and 3 of the SSC in the four groups (Cre$^-$ control, Cre$^-$ ESD, AGR cKO control, and AGR cKO ESD). Bar graphs showing GR activation in astrocytes (n = 4 for each group). S100β$^-$ cells with GR activation appear to be neurons, based on larger nucleus size. Scale bars, 20 μm.

(C) Representative confocal z stack images and bar graphs of MERTK (green) of astrocytes (S100β, red) in layers 2 and 3 of the SSC. The yellow dotted lines outline astrocytic processes. (n = 5, 5, 4, and 5). Scale bars, 5 μm.

(D) Representative confocal z stack images of lysosomes (LAMP2, green) in astrocytes (S100β, red) in layers 2 and 3 of the SSC. The yellow dotted lines outline astrocytes. Bar graphs showing the amount of lysosomes in astrocytes from four different groups (n = 5, 5, 4, and 5). Scale bars, 10 μm.

(E) Representative confocal z stack images and bar graphs showing the PSD95 (green) density in layers 2 and 3 of the SSC from four different groups (n = 7, 5, 6, and 6). Scale bars, 10 μm.

(F and F′) Bar graphs and representative confocal 3D reconstructed images showing the amount of phagocytosed PSD95$^+$ puncta (green, yellow arrows) inside lysosomes (LAMP2, red) in astrocytes (S100β, white) from layers 2 and 3 of the SSC (n = 4, 3, 3, and 4). The yellow boxes indicate the magnified 3D reconstructed areas. Scale bars, 5 μm.

(B–D and F) 14-day-old and (E) 30-day-old male littermates were used. (B–F) n values represent the number of mice per each group. Four data points were obtained from each mouse, and outliers were removed. Data are shown as mean ± SEM. *p < 0.05, **p < 0.005, ***p < 0.001, ****p < 0.0001; two-way ANOVA with Tukey's multiple comparisons test. See also Figures S3 and S4 and Tables S2, S3, and S4.

To assess the changes in astrocytic gene expression in control and AGR cKO mice after ESD, we performed RNA sequencing (RNA-seq) (Tables S2, S3, and S4) using purified astrocytes from the cortices of P14 mice from four different groups (control Cre$^-$ mice: Cre$^-$ control, Cre$^-$ mice exposed to ESD: Cre$^-$ ESD, control AGR cKO mice: AGR cKO control, AGR cKO mice exposed to ESD: AGR cKO ESD). One-way hierarchical clustering and multidimensional scaling showed high reproducibility between biological replicates (Figures S3A and S3B). In addition, analysis of the expression of cell-type-specific marker genes confirmed that astrocyte-specific genes were highly enriched in our samples (Figure S3C). We confirmed that *Nr3c1* (GR) mRNA expression was reduced from both AGR cKO control mice and AGR cKO ESD mice compared with astrocytes from

Cre$^-$ control mice and Cre$^-$ ESD mice (Figure S3D). However, the expression of astrocyte reactive genes, genes related to homeostasis and lactate production, and astrocytic receptors/channels was not different among these four different groups (Figures S3E and S3F). Moreover, the expression of astrocytic molecules that have been implicated in synapse formation and nonphagocytic elimination were not changed (Figure S3G).[38] Among the astrocytic genes involved in phagocytosis and engulfment,[17] the *Mertk* mRNA transcript showed an increased FPKM value in astrocytes from Cre$^-$ ESD compared with astrocytes from Cre$^-$ control mice (Figures S3H and S3I), which is consistent with our *in vitro* data (Figures 1D and S1C). Conversely, *Mertk* mRNA expression was highly decreased in astrocytes from both AGR cKO control mice and AGR cKO ESD mice compared with astrocytes from Cre$^-$ ESD mice, indicating that *Mertk* transcription is not increased in astrocytes lacking GR, even after ESD (Figures S3H and S3I). GO enrichment analysis showed that the expression of phagocytosis- and phagocytic-cup-related genes was upregulated in astrocytes from Cre$^-$ ESD mice compared with astrocytes from Cre$^-$ control mice (Figures S3J and S3K). To understand the transcriptional changes upon GR KO in astrocytes, we compared mRNA expression between AGR cKO control mice and Cre$^-$ control mice. We found that microtubule-based/cilium movement, response to external stimulus-, phagocytosis-, and chemotaxis-related genes were changed in AGR cKO control mice compared with Cre$^-$ control mice (Figure S3L). Moreover, phagocytosis-related genes such as *Baiap2*, *Gas6*, *Ptprj*, *Elmo1*, *Fcer1g*, and *Tyrobp* were commonly downregulated in astrocytes from both AGR cKO control and AGR cKO ESD mice compared with astrocytes from Cre$^-$ control and Cre$^-$ ESD mice (Figure S3M). In contrast, in GR KO astrocytes, the mRNA expression of *Mfge8*, a bridging molecule for integrin-mediated phagocytosis,[39] as well as other phagocytic receptors including *Megf10* and *Axl*, were not changed (Figures S3I and S3M), which is consistent with our *in vitro* data (Figures 1D and S1C). Therefore, our RNA-seq data support the notions that GR regulates specific sets of genes related to phagocytosis in astrocytes and that among those phagocytic components, *Mertk* is the major downstream phagocytic receptor.

Consistent with our transcriptomic profiling in astrocytes, we found that the ESD-induced changes in MERTK expression and lysosomal density in astrocytes were effectively blocked in AGR cKO mice (Figures 4C, 4D, and S4A). There were no changes in VGLUT1$^+$ excitatory pre-synapse, VGAT$^+$ inhibitory pre-synapse and Gephyrin$^+$ inhibitory post-synapse puncta between four different groups (Figures S4B–S4D). However, the reduction in the PSD95$^+$ excitatory post-synaptic density, as well as the increase in the amount of PSD95$^+$ synaptic puncta engulfed by astrocytes observed in Cre$^-$ ESD mice, were substantially attenuated in AGR cKO ESD mice (Figures 4E, 4F′, and S4E). Furthermore, as an independent excitatory post-synaptic marker, we used Homer1 and found that Homer1$^+$ synaptic density (Figure S4F) and the amount of Homer1$^+$ synaptic puncta engulfed by astrocytes (Figures S4G and S4G′) showed consistent changes with PSD95. These findings suggest that astrocytic GR activation plays a major role in regulating stress-induced astrocytic MERTK expression and excitatory synapse loss. We did not observe any compensatory upregulation of microglial phagocytosis in AGR cKO mice, as there were no changes in GR activation and the amount of CD68$^+$ lysosomes in microglia between the brains of Cre$^-$ ESD and AGR cKO ESD mice (Figures S2K and S4H).

Astrocytic GR mediates ESD-induced behavioral symptoms and abnormal neuronal firing

Next, to investigate whether eliminating GR specifically in astrocytes can reduce behavioral abnormalities elicited by ESD, we performed various behavior tests using 4-month-old male Cre$^-$ control mice, Cre$^-$ ESD mice, AGR cKO control mice, and AGR cKO ESD mice (Figure 5A).[40] Consistent with previous study,[41] total traveled distance for 30 min test session was increased in Cre$^-$ ESD mice compared with Cre$^-$ control mice, indicating that ESD induces higher locomotor activity (Figure 5B). In the elevated plus-maze (EPM) test, which is used as a readout for anxiety-like behaviors in animals, Cre$^-$ ESD mice showed no significant difference, despite a trend of spending more time in the open arms (Figure S5A). Along with hyperactivity symptoms, Cre$^-$ ESD mice displayed a significant deficit in general sociability (session 1) in the three-chamber social interaction test, in which the mice were allowed to interact with cages with or without an age- and sex-matched C57BL/6 mouse (Figure 5C). However, in AGR cKO ESD mice, these hyperactive behaviors as well as the reduction in sociability were substantially normalized (Figures 5B and 5C). Notably, Cre$^-$ ESD mice showed highly increased immobility time in the tail suspension test (TST) (Figure 5D) and forced swim test (FST) (Figure 5E), and these phenotypes in TST and FST were also substantially reduced by astrocyte-specific ablation of GR.

On the other hand, Cre$^-$ ESD mice displayed normal social novelty preference (session 2) (Figure S5B) and cognitive function in the novel object recognition (NOR) test (Figure S5C). Independent behavioral experiments performed using 4-month-old female mice showed similar attenuation effects in AGR cKO ESD mice (Figures S5D–S5J).

To better elucidate the brain areas and neuronal networks involved in ESD-induced behavioral deficits, we further examined synaptic density in the other brain areas than SSC, such as the PrL and IL, S1DZ, and LO and VO regions. Consistently with our previous data (Figure S2A), we found no differences in PSD95 density after ESD in the PrL and IL (Figure S5K), which are implicated in goal-directed behaviors as well as recognition memory.[42,43] In contrast, we observed a highly decreased PSD95 density in the S1DZ, and LO and VO regions (Figures S5L and S5M), which are implicated in sociability and social engagement.[44–46] Astrocytic GR was also activated in the LO and VO after ESD (Figure S5N). However, these abnormal changes in GR activation as well as PSD95 density after ESD were largely normalized in AGR cKO mouse background (Figures S5L–S5N), indicating that GR regulates astrocytic phagocytosis and abnormal excitatory synapse loss found in various cortical regions, such as SSC, S1DZ, LO, and VO.

Then, we directly measured neuronal activity in the LO and VO in 4-month-old Cre$^-$ control mice, Cre$^-$ ESD mice, AGR cKO control mice, and AGR cKO ESD mice by *in vivo* multichannel recording while the mice interacted with either objects or sex-matched C57BL/6 mice that were 2 weeks younger (Figures 5F and S5P). We measured neural activity −3 to +5 s from sniff onset

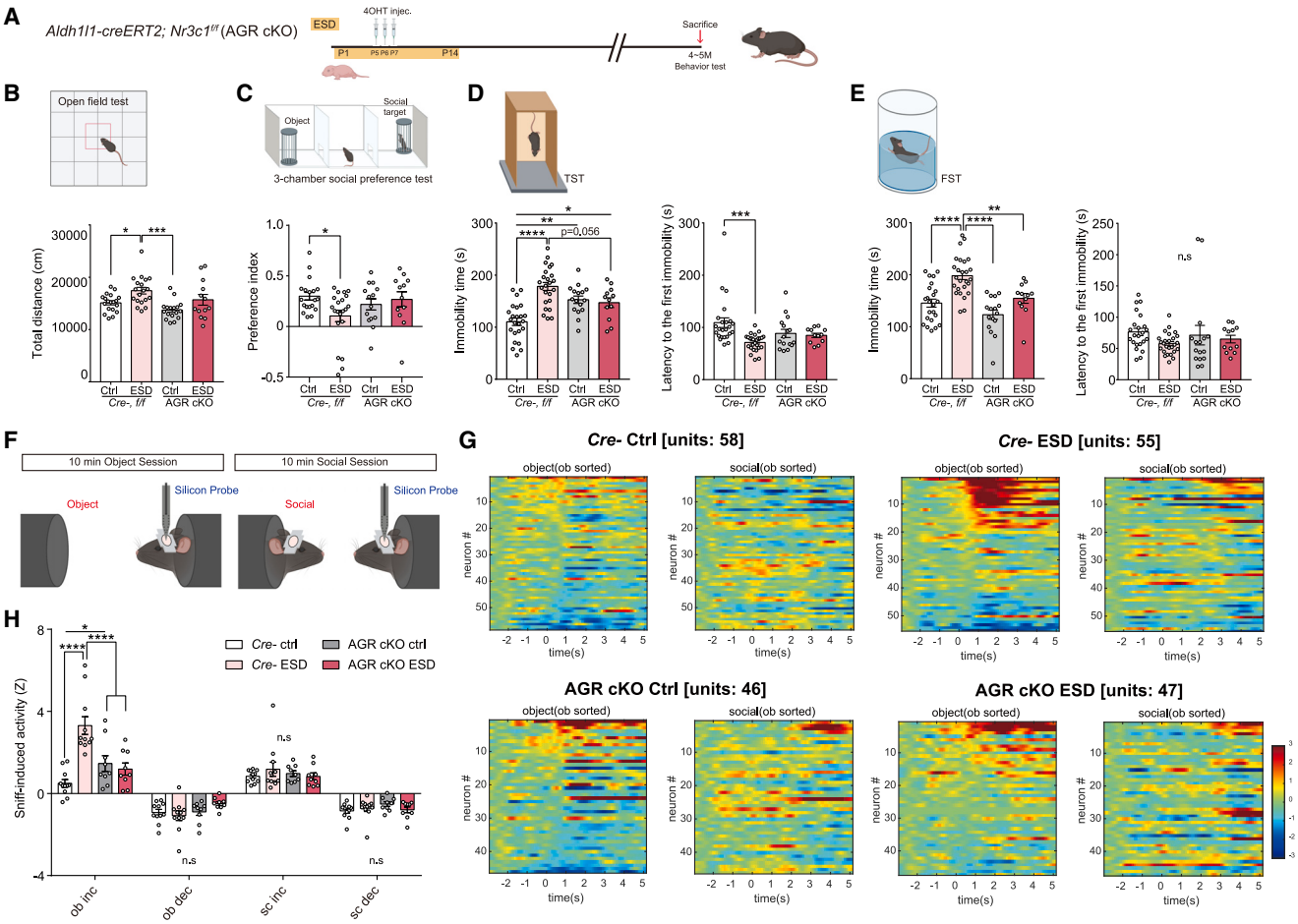

Figure 5. Astrocyte-specific GR ablation attenuates ESD-induced behavioral symptoms and abnormal neuronal activity

(A) Schematic illustration of the ESD experiments and behavioral tests using *Aldh1l1-creERT2; Nr3c1-flox* (AGR cKO) mice.

(B–E) Schematic illustration of the behavioral tests and bar graph showing the results from Cre$^-$ control, Cre$^-$ ESD, AGR cKO control, and AGR cKO ESD groups. Basal locomotor activity measured by the open field test (B), sociability measured by the three-chamber social preference test (C), and depressive behaviors measured by the TST (D: mean duration of immobility [left] and mean latency to the first immobility episode [right]) and FST (E: mean duration of immobility [left] and mean latency to the first immobility episode [right]). Note that all behavioral symptoms observed in Cre$^-$ ESD mice were substantially normalized in the AGR cKO ESD mice. n = 19 (B), 19 (C), 24 (D), and 23 (E) for Cre$^-$ control mice; n = 19 (B), 21 (C), 24 (D), and 26 (E) for Cre$^-$ ESD mice; n = 17 (B), 14 (C), 16 (D), and 16 (E) for AGR cKO control mice; n = 13 (B), 12 (C), 12 (D), and 12 (E) for AGR cKO ESD mice.

(F) Schematic illustration of the protocol used for *in vivo* multichannel recording from the LO and VO.

(G) Heatmaps showing the neuronal activities that responded to object- or social-associated sniffing (Cre$^-$ control mice: n = 3, 58 units; Cre$^-$ ESD mice: n = 4, 55 units; AGR cKO control mice: n = 3, 46 units; AGR cKO ESD mice: n = 4, 47 units). Note that neurons in the heat map were sorted according to the size of responses during object sniffing (ob sorted).

(H) Bar graphs showing average sniff-induced activity (*Z* score) of the top 20% of responding neurons 0–2 s after the onset of object or social sniffing. ob inc, object-induced increase; ob dec, object-induced decrease; sc inc, social-induced increase; sc dec, social-induced decrease.

16- to 19-week-old male littermates were used. n values represent the number of mice per each group. Data are shown as mean ± SEM. *p < 0.05, **p < 0.005, ***p < 0.001, ****p < 0.00001, ns, non-significant (p > 0.05); two-way ANOVA with Tukey's multiple comparisons test. See also Figures S5 and S6.

during the 10-min object and social sessions and found that neuronal responses and corresponding sniff-induced Z activity during the object session were highly increased in Cre$^-$ ESD mice compared with Cre$^-$ control mice (Figures 5G and 5H). Sniff-induced Z activity during the social session was not different between Cre$^-$ control mice and Cre$^-$ ESD mice, supporting our behavioral data showing impaired sociability but normal social novelty preference upon ESD (Figures 5C and S5B). However, the abnormal neural firing observed in Cre$^-$ ESD mice was substantially prevented in AGR cKO ESD mice (Figures 5G and 5H). Consistent with our *in vivo* recording data, we further found that compared with Cre$^-$ control mice, Cre$^-$ ESD mice showed a substantially upregulated c-Fos expression in the LO and VO neurons after interacting with objects, but not with social targets. Importantly, these object-induced increase in c-Fos expression was highly attenuated in AGR cKO ESD mice (Figures S5O and S5O′). Taken together, our behavior, *in vivo* recording, and c-Fos expression data show that hyperactivation of astrocytic GR upon ESD is responsible for evoking abnormal neuronal network activities and behavior symptoms.

GABAergic excitatory post-synapses are preferentially eliminated in ESD model mice

To better understand how excitatory post-synapse loss induces the hyper-neuronal activity and increased c-Fos expression in ESD mice, we tested our hypothesis that excitatory synapses on glutamatergic or GABAergic neurons may be eliminated differentially by astrocytes upon ESD. Thus, instead of using the hSyn promoter, which is active in both glutamatergic and GABAergic neurons, we expressed our mCherry-based synapse elimination reporter, PSD95Δ1,2-mCherry-EGFP with CaMKIIα (calcium/calmodulin-dependent protein kinase II alpha) or GAD67 (glutamic acid decarboxylase 67) promoters to label excitatory post-synapses on glutamatergic or GABAergic neurons, respectively (Figure S6A). This mCherry-EGFP reporter system utilizes the different pKa values of mCherry and EGFP, similar to PSD95Δ1,2-tagBFP-EGFP system (Figures 2I–2L) and we expressed them also in the SSCs by performing IUE with E15.5 mice (Figures S6B and S6C). We found that the amount of CaMKIIα$^+$ glutamatergic neuron-derived mCherry alone puncta in astrocytic lysosomes did not show any changes between the ESD and control SSC (Figure S6D). However, in sharp contrast, the amount of mCherry alone puncta inside astrocytic lysosomes was highly increased in the ESD SSC (Figure S6E), when they originated from GAD67$^+$ GABAergic neurons. Unlike astrocytes, microglia did not show this increase in the amount of engulfed mCherry alone puncta derived from GAD67$^+$ GABAergic neurons (Figure S6F). Taken together, these data raise the possibility that the increased neuronal firing and c-Fos expression in the LO and VO neurons in ESD mice upon interacting with objects may partially stem from the excitatory-inhibitory imbalance,[47] created by the preferential astrocytic phagocytosis of excitatory post-synapses on GABAergic neurons.

Roles of astrocytic MERTK in ESD-mediated synapse elimination

Since our *in vitro* results and RNA-seq data from AGR cKO ESD mice strongly suggest that astrocytic MERTK can be a critical downstream component of ESD-induced GR activation, we generated astrocyte-specific inducible *Mertk* cKO (AMer cKO) mice by breeding *Aldh1l1-creERT2* mice with *loxP*-floxed *Mertk* (*Mertk$^{f/f}$*) mice (Figure 6A). To eliminate astrocytic *Mertk*, we injected 4-OHT into P5 pups for 3 consecutive days and exposed Cre$^-$ and Cre$^+$ AMer cKO mice to ESD (Figure 6A). We found that MERTK expression in astrocytes was highly reduced in AMer cKO mice compared with Cre$^-$ ESD mice (Figures 6C and S7A). As in Cre$^-$ ESD mice, GR activation in astrocytes was successfully induced in AMer cKO ESD mice (Figures 6B, S7A, and S7B), supporting our data that MERTK functions as a downstream component of GR activation in this process.

Using AMer cKO mice, we found that the increased amount of astrocytic lysosomes and the decreased PSD95$^+$ excitatory post-synaptic density observed in Cre$^-$ ESD mice were substantially restored in AMer cKO ESD mice to those in the Cre$^-$ control mice (Figures 6D, 6E, S7A, and S7C), indicating that stress-induced astrocytic *Mertk* expression is necessary to drive excessive excitatory synapse loss. However, we found no changes in VGLUT1$^+$ excitatory pre-synaptic density between four different groups (Cre$^-$ control, Cre$^-$ ESD, AMer cKO control, and AMer cKO ESD) (Figure S7D).

In the mammalian brain, MERTK is highly expressed not only in astrocytes but also in microglia.[48] Therefore, we next examined whether MERTK depletion in astrocytes induced a compensatory increase of microglial phagocytosis. However, there were no changes in the amount of CD68$^+$ microglial lysosomes in AMer cKO mice compared with Cre$^-$ mice either in control or ESD conditions (Figure S7E). To further examine the potential roles of microglial MERTK in the loss of excitatory synapses induced by ESD, we generated microglia-specific *Mertk* cKO (MMer cKO) mice using *Cx3cr1-creERT2* mice. After injecting 4-OHT into P5–P7 MMer cKO pups, we confirmed that MERTK was eliminated specifically in microglia (Figure S7F). However, microglia-specific MERTK ablation failed to prevent the excitatory synapse loss induced by ESD in both layers 2 and 3 and layer 5 of SSC (Figures 6F and S7G), suggesting that microglial MERTK does not participate in excessive excitatory synapse elimination induced by ESD.

Roles of astrocytic MERTK in ESD-induced behavioral symptoms

Finally, we performed behavioral tests using Cre$^-$ control mice, Cre$^-$ ESD mice, AMer cKO control mice, and AMer cKO ESD mice with the same experimental strategies that we used for AGR cKO mice (Figure 7A). As expected, compared with Cre$^-$ control mice, the Cre$^-$ ESD mice showed significant abnormal symptoms in the open field (Figure 7B), sociability (Figure 7C), TST (Figure 7D), and FST (Figure 7E) tests. In addition, ESD did not result in defects in EPM (Figure S7H), social novelty (Figure S7I), and cognitive function (Figure S7J). Female mice showed behavioral phenotypes similar to those of male mice (Figures S7K–S7Q). We found that all of the behavioral deficits observed in Cre$^-$ ESD mice were substantially normalized in AMer cKO ESD mice (Figures 7B–7E).

To determine whether astrocytic MERTK directly participates in evoking abnormal neural activity upon ESD, we again performed *in vivo* multichannel recording in the LO and VO of 4-month-old Cre$^-$ control mice, Cre$^-$ ESD mice, AMer cKO control mice, and AMer cKO ESD mice (Figures 7F and S7R). Consistent with our data from AGR cKO ESD mice (Figures 5G and 5H), we observed that the abnormal neuronal firing in Cre$^-$ ESD mice during the object session was substantially prevented in AMer cKO ESD mice (Figures 7G and 7H), indicating that astrocytic MERTK is responsible for evoking behavioral deficits as well as hyper-neuronal responses of LO and VO neurons in ESD mice.

DISCUSSION

In this study, we demonstrate that early-life stress induces excessive excitatory synapse elimination via the astrocytic GR-MERTK pathway. This event appears to preferentially occur on GABAergic neurons, permanently reshaping neural circuits through astrocytic synapse elimination during post-natal development and making animals much prone to developing abnormal behaviors in adulthood. Deleting GR or MERTK in astrocytes was sufficient to prevent stress-induced brain abnormalities, suggesting that GR-MERTK pathway in astrocytes is largely responsible for stress-induced abnormal behaviors.

Our data show that microglia do not participate in stress-hormone-induced synapse elimination in the ESD mouse model.

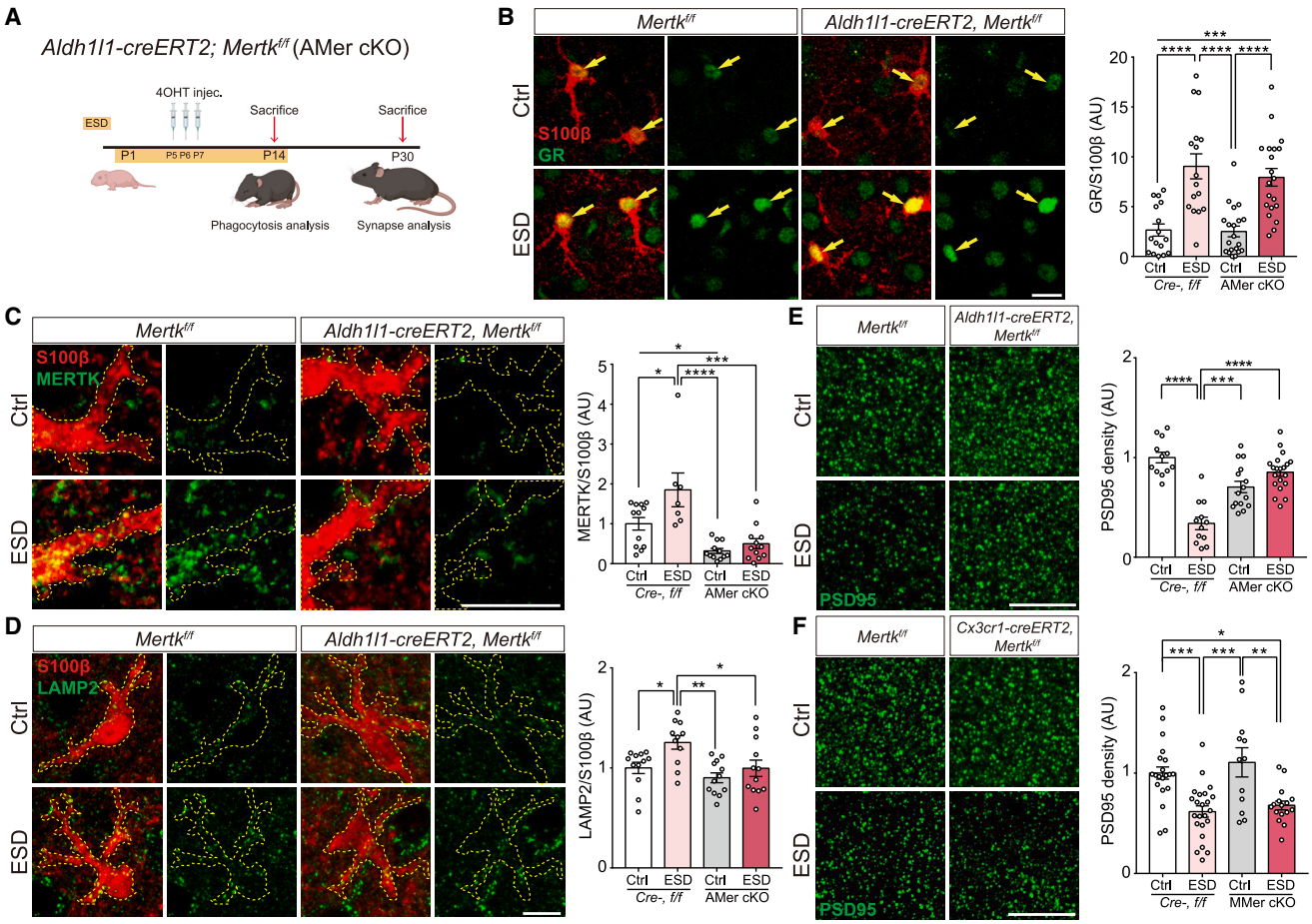

Figure 6. Astrocytic MERTK is a downstream effector of ESD/GR-induced synaptic loss

(A) Schematic illustration of the ESD experiments and behavioral tests using *Aldh1l1-creERT2; Mertk-flox* (AMer cKO) mice.

(B) Representative confocal z stack images of GR (green, yellow arrows) in astrocytes (S100β, red) in layers 2 and 3 of the SSC in the four groups (Cre$^-$ control, Cre$^-$ ESD, AMer cKO control, and AMer cKO ESD). Bar graphs showing GR activation in astrocytes from four different groups (n = 4, 4, 5, and 5). S100β$^-$ cells with GR activation appear to be neurons, based on larger nucleus size. Scale bars, 20 μm.

(C) Representative confocal z stack images of MERTK (green) in astrocytes (S100β, red) in layers 2 and 3 of the SSC. The yellow dotted lines outline astrocytic processes. Bar graph showing MERTK expression in astrocytes from the four groups (n = 4 for each group). Scale bars, 5 μm.

(D) Representative confocal z stack images and bar graphs showing the amount of lysosomes (LAMP2, green) in astrocytes (S100β, red) in layers 2 and 3 of the SSC from the four groups. The yellow dotted lines outline astrocytes (n = 3 for each group). Scale bars, 10 μm.

(E and F) Representative confocal z stack images and bar graphs showing the PSD95 (green) density in layers 2 and 3 of the SSC in AMer (E) and MMer (F, microglia-specific *Mertk* deletion) cKO mice (AMer n = 3, 3, 4, and 4; MMer n = 5, 6, 3, and 4). Scale bars, 10 μm.

(B–D) 14- and (E and F) 30-day-old male littermates were used. (B–F) n values represent the number of mice per each group. Four data points were obtained from each mouse, and outliers were removed. Data are shown as mean ± SEM. *p < 0.05, **p < 0.005, ***p < 0.001, ****p < 0.0001; two-way ANOVA with Tukey's multiple comparisons test. See also Figure S7.

This work together with our previous finding showing that astrocytes play major roles in adult hippocampal synapse elimination for circuit homeostasis,[11] challenge the general consensus that microglia are the primary synapse phagocytes that control synapse number in the developing and adult brains. The primacy of astrocytes over microglia in this work could be due to low GR expression in microglia during early post-natal development, preventing microglia from responding to the increased stress hormones during the critical window for ESD-induced circuit changes.

Through *in vitro*, *in vivo*, and brain organoid experiments, we demonstrate that astrocyte is the major mediator in eliminating excitatory synapses in response to early stress, adding up to the growing evidence that astrocytic phagocytosis play critical roles in brain physiology and animal behaviors. Unlike its role in developmental synapse pruning in the retinogeniculate system,[6] genetic deletion of *Mertk* in astrocytes in control animals did not yield changes in the number of cortical synapses, indicating that at least in the normal developing cortex, astrocytic *Mertk* plays a dispensable role for the developmental synapse pruning. However, when external factors such as stress hormones upregulate *Mertk* expression in astrocytes, this event is sufficient to evoke excessive synapse elimination by astrocytes and cause behavioral abnormalities in the adult animals. Knocking out astrocytic

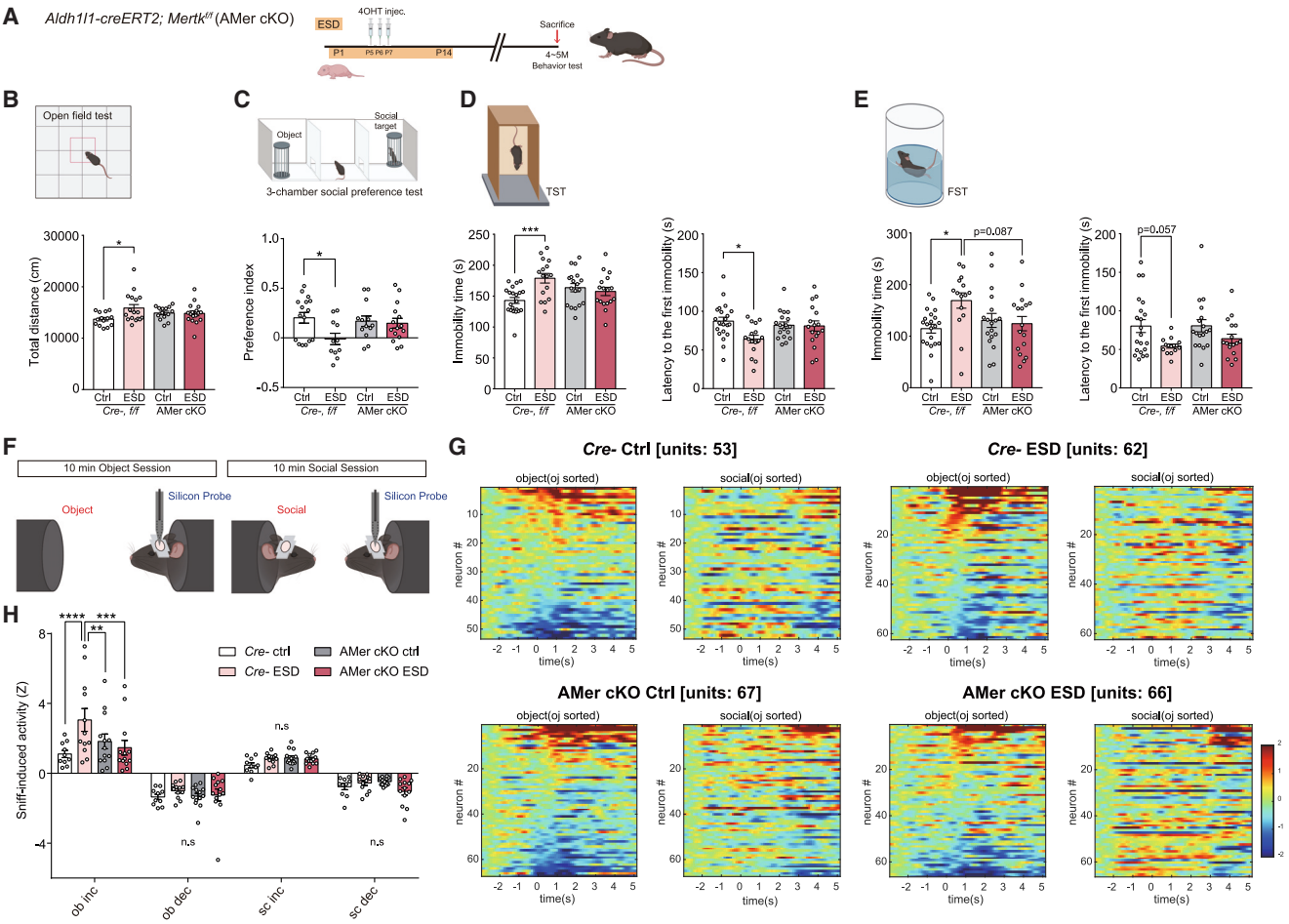

Figure 7. Astrocyte-specific MERTK ablation attenuates ESD-induced behavioral symptoms

(A) Schematic illustration of the ESD experiments and behavioral tests using *Aldh1l1-creERT2; Mertk-flox* (AMer cKO) mice.

(B–E) Bar graph showing the results from behavioral tests Cre$^-$ control, Cre$^-$ ESD, AMer cKO control, and AMer cKO ESD groups. Basal locomotor activity measured by the open field test (B), sociability measured by the three-chamber social preference test (C), and depressive behaviors measured by the TST (D: mean duration of immobility [left] and mean latency to the first immobility episode [right]) and FST (E: mean duration of immobility [left] and mean latency to the first immobility episode [right]). Note that all behavioral symptoms observed in Cre$^-$ ESD mice were substantially normalized in AMer cKO ESD mice. n = 14 (B), 16 (C), 21 (D), and 21 (E) for Cre$^-$ control mice; n = 17 (B), 11 (C), 16 (D), and 15 (E) for Cre$^-$ ESD mice; n = 14 (B), 13 (C), 18 (D), and 18 (E) for AMer cKO control mice; n = 17 (B), 15 (C), 17 (D), and 17 (E) for AMer cKO ESD mice.

(F) Schematic illustration of the protocol used for *in vivo* multichannel recording from the LO and VO.

(G) Heatmaps showing the neuronal activities that responded to object- or social-associated sniffing (Cre$^-$ control mice: n = 1, 53 units; Cre$^-$ ESD mice: n = 3, 62 units; AMer cKO control mice: n = 2, 67 units; AMer cKO ESD mice: n = 3, 66 units).

(H) Bar graphs showing average sniff-induced activity (*Z* score) of the top 20% of responding neurons 0–2 s after the onset of object or social sniffing. ob inc, object-induced increase; ob dec, object-induced decrease; sc inc, social-induced increase; sc dec, social-induced decrease.

16- to 19-week-old male littermates were used. n values represent the number of mice per each group. Data are shown as mean ± SEM. *p < 0.05, **p < 0.005, ***p < 0.001, ****p < 0.0001, ns, non-significant (p > 0.05); two-way ANOVA with Tukey's multiple comparisons test. See also Figures S6 and S7.

Mertk substantially attenuated excessive synapse elimination and corresponding behavioral abnormalities, indicating that manipulating the expression of phagocytic receptors in astrocytes may serve as a therapeutic strategy or preventive care for the stress-induced brain disorders.

Our findings raise many additional questions. First, why are only excitatory but not inhibitory synapses affected by stress-induced astrocytic phagocytosis? Previously, we have shown that when phosphatidylserine is exposed to the outer neuronal membrane by deleting CDC50a, microglia recognize synaptic phosphatidylserine as an eat-me signal and phagocytose inhibitory synapses through MERTK.[12] In this experimental design with CDC50a deletion, astrocytes failed to participate in eliminating phosphatidylserine-exposing inhibitory synapses, despite that astrocytes do express phosphatidylserine recognizing receptors, such as MERTK and AXL. Therefore, it is plausible that astrocytic MERTK may be specialized in eliminating excitatory synapses, but not inhibitory synapses.

Second, our study suggests the possibility that astrocytic GR-MERTK pathway could be responsible for brain disorders

induced by other types of stress. For example, it has been suggested that the exposure to extremely stressful events during pregnancy or even adolescent stages increases the risk of schizophrenia. Activated MERTK transcription by stress hormones during the critical embryonic or adolescent developmental stages could damage synapses that transiently expose phosphatidylserine,[49] reducing their numbers and disrupting neuronal network activity. Although our present work focuses on developmental synapse elimination by astrocytes, we have previously shown that astrocytes constantly eliminate synapses in the adult[11] as well as aged brains.[50] Therefore, it would be extremely interesting to test whether stressful events or direct stress hormone injection can induce MERTK-dependent synapse loss in the adult and aged brains. Such events may play a synergistic role with the conditions where synapses become vulnerable for phagocytic elimination during brain injuries and/or neurodegenerative diseases, which may exacerbate disease-induced synapse loss and neurological outcomes.

Third, our study raises a potential warning whether astrocytic GR-MERTK pathway could be activated upon synthetic glucocorticoid/corticosteroids administration during childhood. Currently, many children are being prescribed synthetic glucocorticoid/corticosteroids to treat inflammation caused by various diseases[51] including brain tumor[52] and meningitis.[53,54] It would be worth critically re-evaluating these types of treatments since long-term use of synthetic glucocorticoid/corticosteroids during critical periods of brain plasticity may evoke excessive synapse elimination by astrocytes and eventual abnormal behaviors when they grow up.

A previous genome-wide association study (GWAS) revealed that variations in complement *C4* gene copy number can serve as a generic risk factor for schizophrenia.[55] After this initial discovery, it has been shown that microglia-like cells differentiated from inducible pluripotent stem cells derived from schizophrenia patients showed stronger phagocytic capacity compared with control groups.[56] Recently, it has also been shown that overexpressing C4A in mice resulted in the reduced synaptic density and abnormal behaviors,[57] indicating that excessive microglia-mediated synapse elimination is also a potential risk factor for behavioral abnormalities.

Along with genetic risk factors, environmental factors, such as stress, have been thought to strongly contribute to the initiation of depression and schizophrenia. Our study indicates that astrocytic phagocytosis plays a major role in the initiation of stress-induced behavior abnormalities. Whether astrocytic GR-MERTK play synergistic roles with known genetic risk factors, such as C4A in inducing mental disorders and schizophrenia would be fascinating subjects for future studies.

Limitations of the study

Our data suggest that even among excitatory synaptic population, excitatory synapses on GABAergic, but not glutamatergic neurons are preferentially engulfed by astrocytes upon ESD, suggesting that the functional impairment of interneurons may play central roles in initiating abnormal neuronal firing and behavioral symptoms in our study.[47,58] This sophisticated degree of specificity may be regulated by multiple factors, such as the presentation of synaptic eat-me and "do not eat-me" signals,[59–61] changes in maturation status of interneurons as well as the expression levels of astrocytic MERTK upon ESD. Since our current data heavily rely on synapse phagocytosis reporters with CaMKIIα or GAD67 promoters, future experiments will be required to validate our observation and reveal the exact mechanisms of this preferential elimination.

STAR★METHODS

Detailed methods are provided in the online version of this paper and include the following:

- KEY RESOURCES TABLE
- RESOURCE AVAILABILITY
  - Lead contact
  - Materials availability
  - Data and code availability
- EXPERIMENTAL MODEL AND STUDY PARTICIPANT DETAILS
  - Mice
- METHOD DETAILS
  - Synaptosome purification and pHrodo conjugation
  - *In vitro* live-imaging phagocytosis assay for compound screening
  - *In vitro* live-imaging phagocytosis assay for stress hormones
  - Astrocyte-Conditioned Medium (ACM)
  - Real-time PCR (qPCR)
  - Lentivirus (LV) production
  - Maintenance of human embryonic stem cells
  - Development of cortical organoids from human embryonic stem cells
  - *In utero* electroporation (IUE)
  - Early social deprivation (ESD) protocol and 4-hydroxytamoxifen (4-OHT) injection
  - Immunohistochemistry (IHC) and image analysis
  - Western blotting
  - Sample preparation for RNA sequencing
  - RNA sequencing data analysis
  - Differentially expressed genes (DEGs) analysis
  - Experimental design for c-Fos analysis
  - Behavior analysis
  - *In vivo* multichannel (extracellular) recording
  - Illustrations
- QUANTIFICATION AND STATISTICAL ANALYSIS

SUPPLEMENTAL INFORMATION

Supplemental information can be found online at https://doi.org/10.1016/j.immuni.2023.07.005.

ACKNOWLEDGMENTS

We thank all members of the Chung laboratory and Seongwan Park (S.P.) for helpful discussion. We especially thank Y.-J.C. and C.-H.S. for providing the MERTK overexpression plasmid and synaptic phagocytosis reporter plasmids. We also thank S.Y.L. for providing LV-EF1α-ZsGreen and M.K. for technical support. Assistance with Imaris software was provided by the KAIST Bio Core Center. This work was supported by National Research Foundation of Korea (NRF) grant funded by the Korean Government (Ministry of Science and ICT, MSIT) 2020M3E5D9079912, 2021R1A2C3005704, and 2022M3E5E8081188 (to W.-S.C.); The Korea Health Technology R&D Project through

the Korea Health Industry Development Institute (KHIDI) and Korea Dementia Research Center (KDRC) HU20C0290 (to W.-S.C.); Institute for Basic Science IBS-R002-D1 (to E.K.); Institute for Basic Science IBS-R002-A2 and NRF grant 2021R1A2C3012159 (to S.-H.L.); NRF grants 2019R1C1C1006600 and 2020M3A9E4039670 (to K.-J.Y.); and Brain Pool Program from MSIT 2019H1D3A2A020616052 (to N.-S.K.).

AUTHOR CONTRIBUTIONS

W.-S.C., Y.G.B., and N.-S.K. designed the projects and wrote the manuscript. Y.G.B. performed compound screening, the *in vitro* experiments with primary astrocytes, qPCR, western blotting, lentivirus production, the *in vivo* experiments, confocal imaging, data analysis, and sample preparation for RNA sequencing. N.-S.K. performed the behavioral experiments, behavioral data analysis and sample preparation for RNA sequencing. G.K. performed the *in vivo* experiments, confocal imaging, and data analysis. Y.-S.J. and S.-H.L. performed the *in vivo* recording and data analysis. J.B.C. and Y.-M.H. maintained hCOs and performed western blotting, confocal imaging, and data analysis. C.-W.P. and K.-J.Y. performed *in utero* electroporation. K.K., H.J., J.K., and E.K. provided support for the experiments.

DECLARATION OF INTERESTS

The authors declare no competing interests.

Received: December 16, 2022
Revised: May 9, 2023
Accepted: July 6, 2023
Published: July 31, 2023

REFERENCES

1. Heim, C., and Nemeroff, C.B. (2001). The role of childhood trauma in the neurobiology of mood and anxiety disorders: preclinical and clinical studies. Biol. Psychiatry *49*, 1023–1039. https://doi.org/10.1016/s0006-3223(01)01157-x.
2. Carr, C.P., Martins, C.M., Stingel, A.M., Lemgruber, V.B., and Juruena, M.F. (2013). The role of early life stress in adult psychiatric disorders: a systematic review according to childhood trauma subtypes. J. Nerv. Ment. Dis. *201*, 1007–1020. https://doi.org/10.1097/NMD.0000000000000049.
3. Penzes, P., Cahill, M.E., Jones, K.A., VanLeeuwen, J.E., and Woolfrey, K.M. (2011). Dendritic spine pathology in neuropsychiatric disorders. Nat. Neurosci. *14*, 285–293. https://doi.org/10.1038/nn.2741.
4. Hall, J., Trent, S., Thomas, K.L., O'Donovan, M.C., and Owen, M.J. (2015). Genetic risk for schizophrenia: convergence on synaptic pathways involved in plasticity. Biol. Psychiatry *77*, 52–58. https://doi.org/10.1016/j.biopsych.2014.07.011.
5. Coyle, J.T., Ruzicka, W.B., and Balu, D.T. (2020). Fifty years of research on schizophrenia: the ascendance of the glutamatergic synapse. Am. J. Psychiatry *177*, 1119–1128. https://doi.org/10.1176/appi.ajp.2020.20101481.
6. Chung, W.S., Clarke, L.E., Wang, G.X., Stafford, B.K., Sher, A., Chakraborty, C., Joung, J., Foo, L.C., Thompson, A., Chen, C., et al. (2013). Astrocytes mediate synapse elimination through MEGF10 and MERTK pathways. Nature *504*, 394–400. https://doi.org/10.1038/nature12776.
7. MacDonald, J.M., Beach, M.G., Porpiglia, E., Sheehan, A.E., Watts, R.J., and Freeman, M.R. (2006). The Drosophila cell corpse engulfment receptor Draper mediates glial clearance of severed axons. Neuron *50*, 869–881. https://doi.org/10.1016/j.neuron.2006.04.028.
8. Wu, H.H., Bellmunt, E., Scheib, J.L., Venegas, V., Burkert, C., Reichardt, L.F., Zhou, Z., Fariñas, I., and Carter, B.D. (2009). Glial precursors clear sensory neuron corpses during development via Jedi-1, an engulfment receptor. Nat. Neurosci. *12*, 1534–1541. https://doi.org/10.1038/nn.2446.
9. Tasdemir-Yilmaz, O.E., and Freeman, M.R. (2014). Astrocytes engage unique molecular programs to engulf pruned neuronal debris from distinct subsets of neurons. Genes Dev. *28*, 20–33. https://doi.org/10.1101/gad.229518.113.
10. Lemke, G., and Rothlin, C.V. (2008). Immunobiology of the TAM receptors. Nat. Rev. Immunol. *8*, 327–336. https://doi.org/10.1038/nri2303.
11. Lee, J.H., Kim, J.Y., Noh, S., Lee, H., Lee, S.Y., Mun, J.Y., Park, H., and Chung, W.S. (2021). Astrocytes phagocytose adult hippocampal synapses for circuit homeostasis. Nature *590*, 612–617. https://doi.org/10.1038/s41586-020-03060-3.
12. Park, J., Choi, Y., Jung, E., Lee, S.H., Sohn, J.W., and Chung, W.S. (2021). Microglial MERTK eliminates phosphatidylserine-displaying inhibitory post-synapses. EMBO J. *40*, e107121. https://doi.org/10.15252/embj.2020107121.
13. Byun, Y.G., and Chung, W.S. (2018). A novel in vitro live-imaging assay of astrocyte-mediated phagocytosis using pH indicator-conjugated synaptosomes. J. Vis. Exp. https://doi.org/10.3791/56647.
14. Yau, J.L., and Seckl, J.R. (2012). Local amplification of glucocorticoids in the aging brain and impaired spatial memory. Front. Aging Neurosci. *4*, 24. https://doi.org/10.3389/fnagi.2012.00024.
15. Gray, J.D., Kogan, J.F., Marrocco, J., and McEwen, B.S. (2017). Genomic and epigenomic mechanisms of glucocorticoids in the brain. Nat. Rev. Endocrinol. *13*, 661–673. https://doi.org/10.1038/nrendo.2017.97.
16. Foo, L.C., Allen, N.J., Bushong, E.A., Ventura, P.B., Chung, W.S., Zhou, L., Cahoy, J.D., Daneman, R., Zong, H., Ellisman, M.H., et al. (2011). Development of a method for the purification and culture of rodent astrocytes. Neuron *71*, 799–811. https://doi.org/10.1016/j.neuron.2011.07.022.
17. Cahoy, J.D., Emery, B., Kaushal, A., Foo, L.C., Zamanian, J.L., Christopherson, K.S., Xing, Y., Lubischer, J.L., Krieg, P.A., Krupenko, S.A., et al. (2008). A transcriptome database for astrocytes, neurons, and oligodendrocytes: a new resource for understanding brain development and function. J. Neurosci. *28*, 264–278. https://doi.org/10.1523/JNEUROSCI.4178-07.2008.
18. Carter, B.S., Meng, F., and Thompson, R.C. (2012). Glucocorticoid treatment of astrocytes results in temporally dynamic transcriptome regulation and astrocyte-enriched mRNA changes in vitro. Physiol. Genomics *44*, 1188–1200. https://doi.org/10.1152/physiolgenomics.00097.2012.
19. Clarke, L.E., Liddelow, S.A., Chakraborty, C., Münch, A.E., Heiman, M., and Barres, B.A. (2018). Normal aging induces A1-like astrocyte reactivity. Proc. Natl. Acad. Sci. USA *115*, E1896–E1905. https://doi.org/10.1073/pnas.1800165115.
20. Neher, J.J., Emmrich, J.V., Fricker, M., Mander, P.K., Théry, C., and Brown, G.C. (2013). Phagocytosis executes delayed neuronal death after focal brain ischemia. Proc. Natl. Acad. Sci. USA *110*, E4098–E4107. https://doi.org/10.1073/pnas.1308679110.
21. Shi, X., Luo, L., Wang, J., Shen, H., Li, Y., Mamtilahun, M., Liu, C., Shi, R., Lee, J.H., Tian, H., et al. (2021). Stroke subtype-dependent synapse elimination by reactive gliosis in mice. Nat Commun *12*, 6943. https://doi.org/10.1038/s41467-021-27248-x.
22. Huang, Y., Happonen, K.E., Burrola, P.G., O'Connor, C., Hah, N., Huang, L., Nimmerjahn, A., and Lemke, G. (2021). Microglia use TAM receptors to detect and engulf amyloid beta plaques. Nat Immunol *22*, 586–594. https://doi.org/10.1038/s41590-021-00913-5.
23. Cabezón, R., Carrera-Silva, E.A., Flórez-Grau, G., Errasti, A.E., Calderón-Gómez, E., Lozano, J.J., España, C., Ricart, E., Panés, J., Rothlin, C.V., et al. (2015). MERTK as negative regulator of human T cell activation. J. Leukoc. Biol. *97*, 751–760. https://doi.org/10.1189/jlb.3A0714-334R.
24. Heideveld, E., Hampton-O'Neil, L.A., Cross, S.J., van Alphen, F.P.J., van den Biggelaar, M., Toye, A.M., and van den Akker, E. (2018). Glucocorticoids induce differentiation of monocytes towards macrophages that share functional and phenotypical aspects with erythroblastic island macrophages. Haematologica *103*, 395–405. https://doi.org/10.3324/haematol.2017.179341.
25. Adomati, T., Cham, L.B., Hamdan, T.A., Bhat, H., Duhan, V., Li, F., Ali, M., Lang, E., Huang, A., Naser, E., et al. (2020). Dead cells induce innate anergy via Mertk after acute viral infection. Cell Rep. *30*, 3671–3681.e5. https://doi.org/10.1016/j.celrep.2020.02.101.

26. Duman, R.S., Aghajanian, G.K., Sanacora, G., and Krystal, J.H. (2016). Synaptic plasticity and depression: new insights from stress and rapid-acting antidepressants. Nat. Med. *22*, 238–249. https://doi.org/10.1038/nm.4050.

27. Shin, S., Pribiag, H., Lilascharoen, V., Knowland, D., Wang, X.Y., and Lim, B.K. (2018). Drd3 signaling in the lateral septum mediates early life stress-induced social dysfunction. Neuron *97*, 195–208.e6. https://doi.org/10.1016/j.neuron.2017.11.040.

28. Zhang, G.W., Shen, L., Tao, C., Jung, A.H., Peng, B., Li, Z., Zhang, L.I., and Tao, H.W. (2021). Medial preoptic area antagonistically mediates stress-induced anxiety and parental behavior. Nat. Neurosci. *24*, 516–528. https://doi.org/10.1038/s41593-020-00784-3.

29. Arnold, D.B., and Clapham, D.E. (1999). Molecular determinants for subcellular localization of PSD-95 with an interacting K+ channel. Neuron *23*, 149–157. https://doi.org/10.1016/s0896-6273(00)80761-8.

30. Hayashi-Takagi, A., Yagishita, S., Nakamura, M., Shirai, F., Wu, Y.I., Loshbaugh, A.L., Kuhlman, B., Hahn, K.M., and Kasai, H. (2015). Labelling and optical erasure of synaptic memory traces in the motor cortex. Nature *525*, 333–338. https://doi.org/10.1038/nature15257.

31. Raponi, E., Agenes, F., Delphin, C., Assard, N., Baudier, J., Legraverend, C., and Deloulme, J.C. (2007). S100B expression defines a state in which GFAP-expressing cells lose their neural stem cell potential and acquire a more mature developmental stage. Glia *55*, 165–177. https://doi.org/10.1002/glia.20445.

32. Auguste, Y.S.S., Ferro, A., Kahng, J.A., Xavier, A.M., Dixon, J.R., Vrudhula, U., Nichitiu, A.S., Rosado, D., Wee, T.L., Pedmale, U.V., et al. (2022). Oligodendrocyte precursor cells engulf synapses during circuit remodeling in mice. Nat. Neurosci. *25*, 1273–1278. https://doi.org/10.1038/s41593-022-01170-x.

33. Jauregui-Huerta, F., Ruvalcaba-Delgadillo, Y., Gonzalez-Castañeda, R., Garcia-Estrada, J., Gonzalez-Perez, O., and Luquin, S. (2010). Responses of glial cells to stress and glucocorticoids. Curr. Immunol. Rev. *6*, 195–204. https://doi.org/10.2174/157339510791823790.

34. Calcia, M.A., Bonsall, D.R., Bloomfield, P.S., Selvaraj, S., Barichello, T., and Howes, O.D. (2016). Stress and neuroinflammation: a systematic review of the effects of stress on microglia and the implications for mental illness. Psychopharmacol. (Berl.) *233*, 1637–1650. https://doi.org/10.1007/s00213-016-4218-9.

35. Paolicelli, R.C., Bolasco, G., Pagani, F., Maggi, L., Scianni, M., Panzanelli, P., Giustetto, M., Ferreira, T.A., Guiducci, E., Dumas, L., et al. (2011). Synaptic pruning by microglia is necessary for normal brain development. Science *333*, 1456–1458. https://doi.org/10.1126/science.1202529.

36. Schafer, D.P., Lehrman, E.K., Kautzman, A.G., Koyama, R., Mardinly, A.R., Yamasaki, R., Ransohoff, R.M., Greenberg, M.E., Barres, B.A., and Stevens, B. (2012). Microglia sculpt postnatal neural circuits in an activity and complement-dependent manner. Neuron *74*, 691–705. https://doi.org/10.1016/j.neuron.2012.03.026.

37. Gordon, A., Yoon, S.J., Tran, S.S., Makinson, C.D., Park, J.Y., Andersen, J., Valencia, A.M., Horvath, S., Xiao, X., Huguenard, J.R., et al. (2021). Long-term maturation of human cortical organoids matches key early postnatal transitions. Nat. Neurosci. *24*, 331–342. https://doi.org/10.1038/s41593-021-00802-y.

38. Boisvert, M.M., Erikson, G.A., Shokhirev, M.N., and Allen, N.J. (2018). The aging astrocyte transcriptome from multiple regions of the mouse brain. Cell Rep. *22*, 269–285. https://doi.org/10.1016/j.celrep.2017.12.039.

39. Hanayama, R., Tanaka, M., Miwa, K., Shinohara, A., Iwamatsu, A., and Nagata, S. (2002). Identification of a factor that links apoptotic cells to phagocytes. Nature *417*, 182–187. https://doi.org/10.1038/417182a.

40. Chun, S., Du, F., Westmoreland, J.J., Han, S.B., Wang, Y.D., Eddins, D., Bayazitov, I.T., Devaraju, P., Yu, J., Mellado Lagarde, M.M., et al. (2017). Thalamic miR-338-3p mediates auditory thalamocortical disruption and its late onset in models of 22q11.2 microdeletion. Nat. Med. *23*, 39–48. https://doi.org/10.1038/nm.4240.

41. Cui, Y., Cao, K., Lin, H., Cui, S., Shen, C., Wen, W., Mo, H., Dong, Z., Bai, S., Yang, L., et al. (2020). Early-life stress induces depression-like behavior and synaptic-plasticity changes in a maternal separation rat model: gender difference and metabolomics study. Front. Pharmacol. *11*, 102. https://doi.org/10.3389/fphar.2020.00102.

42. Padilla-Coreano, N., Bolkan, S.S., Pierce, G.M., Blackman, D.R., Hardin, W.D., Garcia-Garcia, A.L., Spellman, T.J., and Gordon, J.A. (2016). Direct ventral hippocampal-prefrontal input is required for anxiety-related neural activity and behavior. Neuron *89*, 857–866. https://doi.org/10.1016/j.neuron.2016.01.011.

43. Elliott, E., Manashirov, S., Zwang, R., Gil, S., Tsoory, M., Shemesh, Y., and Chen, A. (2016). Dnmt3a in the medial prefrontal cortex regulates anxiety-like behavior in adult mice. J. Neurosci. *36*, 730–740. https://doi.org/10.1523/JNEUROSCI.0971-15.2016.

44. Jennings, J.H., Kim, C.K., Marshel, J.H., Raffiee, M., Ye, L., Quirin, S., Pak, S., Ramakrishnan, C., and Deisseroth, K. (2019). Interacting neural ensembles in orbitofrontal cortex for social and feeding behaviour. Nature *565*, 645–649. https://doi.org/10.1038/s41586-018-0866-8.

45. Walton, E., Hibar, D.P., van Erp, T.G.M., Potkin, S.G., Roiz-Santiañez, R., Crespo-Facorro, B., Suarez-Pinilla, P., van Haren, N.E.M., de Zwarte, S.M.C., Kahn, R.S., et al. (2018). Prefrontal cortical thinning links to negative symptoms in schizophrenia via the ENIGMA consortium. Psychol. Med. *48*, 82–94. https://doi.org/10.1017/S0033291717001283.

46. Shin Yim, Y., Park, A., Berrios, J., Lafourcade, M., Pascual, L.M., Soares, N., Yeon Kim, J., Kim, S., Kim, H., Waisman, A., et al. (2017). Reversing behavioural abnormalities in mice exposed to maternal inflammation. Nature *549*, 482–487. https://doi.org/10.1038/nature23909.

47. Selten, M., van Bokhoven, H., and Nadif Kasri, N. (2018). Inhibitory control of the excitatory/inhibitory balance in psychiatric disorders. F1000Res *7*, 23. https://doi.org/10.12688/f1000research.12155.1.

48. Zhang, Y., Sloan, S.A., Clarke, L.E., Caneda, C., Plaza, C.A., Blumenthal, P.D., Vogel, H., Steinberg, G.K., Edwards, M.S., Li, G., et al. (2016). Purification and characterization of progenitor and mature human astrocytes reveals transcriptional and functional differences with mouse. Neuron *89*, 37–53. https://doi.org/10.1016/j.neuron.2015.11.013.

49. Brown, G.C., and Neher, J.J. (2014). Microglial phagocytosis of live neurons. Nat Rev Neurosci *15*, 209–216. https://doi.org/10.1038/nrn3710.

50. Lee, E., Jung, Y.J., Park, Y.R., Lim, S., Choi, Y.J., Lee, S.Y., Kim, C.H., Mun, J.Y., and Chung, W.S. (2022). A distinct astrocyte subtype in the aging mouse brain characterized by impaired protein homeostasis. Nat Aging *2*, 726–741. https://doi.org/10.1038/s43587-022-00257-1.

51. Ferrara, G., Petrillo, M.G., Giani, T., Marrani, E., Filippeschi, C., Oranges, T., Simonini, G., and Cimaz, R. (2019). Clinical Use and Molecular Action of Corticosteroids in the Pediatric Age. Int J Mol Sci *20*. https://doi.org/10.3390/ijms20020444.

52. Hwang, E.I., Sayour, E.J., Flores, C.T., Grant, G., Wechsler-Reya, R., Hoang-Minh, L.B., Kieran, M.W., Salcido, J., Prins, R.M., Figg, J.W., et al. (2022). The current landscape of immunotherapy for pediatric brain tumors. Nat Cancer *3*, 11–24. https://doi.org/10.1038/s43018-021-00319-0.

53. Wilkinson, R.J., Rohlwink, U., Misra, U.K., van Crevel, R., Mai, N.T.H., Dooley, K.E., Caws, M., Figaji, A., Savic, R., Solomons, R., et al. (2017). Tuberculous meningitis. Nat. Rev. Neurol. *13*, 581–598. https://doi.org/10.1038/nrneurol.2017.120.

54. Gundamraj, S., and Hasbun, R. (2020). The use of adjunctive steroids in central nervous infections. Front. Cell. Infect. Microbiol. *10*, 592017. https://doi.org/10.3389/fcimb.2020.592017.

55. Sekar, A., Bialas, A.R., de Rivera, H., Davis, A., Hammond, T.R., Kamitaki, N., Tooley, K., Presumey, J., Baum, M., Van Doren, V., et al. (2016). Schizophrenia risk from complex variation of complement component 4. Nature *530*, 177–183. https://doi.org/10.1038/nature16549.

56. Sellgren, C.M., Gracias, J., Watmuff, B., Biag, J.D., Thanos, J.M., Whittredge, P.B., Fu, T., Worringer, K., Brown, H.E., Wang, J., et al. (2019). Increased synapse elimination by microglia in schizophrenia patient-derived models of synaptic pruning. Nat Neurosci *22*, 374–385. https://doi.org/10.1038/s41593-018-0334-7.

57. Yilmaz, M., Yalcin, E., Presumey, J., Aw, E., Ma, M., Whelan, C.W., Stevens, B., McCarroll, S.A., and Carroll, M.C. (2021). Overexpression of schizophrenia susceptibility factor human complement C4A promotes excessive synaptic loss and behavioral changes in mice. Nat Neurosci *24*, 214–224. https://doi.org/10.1038/s41593-020-00763-8.

58. Marín, O. (2012). Interneuron dysfunction in psychiatric disorders. Nat. Rev. Neurosci. *13*, 107–120. https://doi.org/10.1038/nrn3155.

59. Lehrman, E.K., Wilton, D.K., Litvina, E.Y., Welsh, C.A., Chang, S.T., Frouin, A., Walker, A.J., Heller, M.D., Umemori, H., Chen, C., et al. (2018). CD47 protects synapses from excess microglia-mediated pruning during development. Neuron *100*, 120–134.e6. https://doi.org/10.1016/j.neuron.2018.09.017.

60. Li, T., Chiou, B., Gilman, C.K., Luo, R., Koshi, T., Yu, D., Oak, H.C., Giera, S., Johnson-Venkatesh, E., Muthukumar, A.K., et al. (2020). A splicing isoform of GPR56 mediates microglial synaptic refinement via phosphatidylserine binding. EMBO J. *39*, e104136. https://doi.org/10.15252/embj.2019104136.

61. Scott-Hewitt, N., Perrucci, F., Morini, R., Erreni, M., Mahoney, M., Witkowska, A., Carey, A., Faggiani, E., Schuetz, L.T., Mason, S., et al. (2020). Local externalization of phosphatidylserine mediates developmental synaptic pruning by microglia. EMBO J. *39*, e105380. https://doi.org/10.15252/embj.2020105380.

62. Bansal, R., and Pfeiffer, S.E. (1989). Reversible inhibition of oligodendrocyte progenitor differentiation by a monoclonal antibody against surface galactolipids. Proc. Natl. Acad. Sci. USA *86*, 6181–6185. https://doi.org/10.1073/pnas.86.16.6181.

63. van der Doelen, R.H., Calabrese, F., Guidotti, G., Geenen, B., Riva, M.A., Kozicz, T., and Homberg, J.R. (2014). Early life stress and serotonin transporter gene variation interact to affect the transcription of the glucocorticoid and mineralocorticoid receptors, and the co-chaperone FKBP5, in the adult rat brain. Front. Behav. Neurosci. *8*, 355. https://doi.org/10.3389/fnbeh.2014.00355.

64. Liddelow, S.A., Guttenplan, K.A., Clarke, L.E., Bennett, F.C., Bohlen, C.J., Schirmer, L., Bennett, M.L., Münch, A.E., Chung, W.S., Peterson, T.C., et al. (2017). Neurotoxic reactive astrocytes are induced by activated microglia. Nature *541*, 481–487. https://doi.org/10.1038/nature21029.

65. Kim, J.H., Ma, D.H., Jung, E., Choi, I., and Lee, S.H. (2021). Gated feedforward inhibition in the frontal cortex releases goal-directed action. Nat. Neurosci. *24*, 1452–1464. https://doi.org/10.1038/s41593-021-00910-9.

66. Gilles, J.F., Dos Santos, M., Boudier, T., Bolte, S., and Heck, N. (2017). DiAna, an ImageJ tool for object-based 3D co-localization and distance analysis. Methods *115*, 55–64. https://doi.org/10.1016/j.ymeth.2016.11.016.

67. Dunkley, P.R., Jarvie, P.E., and Robinson, P.J. (2008). A rapid Percoll gradient procedure for preparation of synaptosomes. Nat. Protoc. *3*, 1718–1728. https://doi.org/10.1038/nprot.2008.171.

68. Foo, L.C. (2013). Purification of rat and mouse astrocytes by immunopanning. Cold Spring Harb. Protoc. *2013*, 421–432. https://doi.org/10.1101/pdb.prot074211.

69. Thomson, J.A., Itskovitz-Eldor, J., Shapiro, S.S., Waknitz, M.A., Swiergiel, J.J., Marshall, V.S., and Jones, J.M. (1998). Embryonic stem cell lines derived from human blastocysts. Science *282*, 1145–1147. https://doi.org/10.1126/science.282.5391.1145.

70. Paşca, A.M., Sloan, S.A., Clarke, L.E., Tian, Y., Makinson, C.D., Huber, N., Kim, C.H., Park, J.Y., O'Rourke, N.A., Nguyen, K.D., et al. (2015). Functional cortical neurons and astrocytes from human pluripotent stem cells in 3D culture. Nat. Methods *12*, 671–678. https://doi.org/10.1038/nmeth.3415.

71. Yoon, K.J., Ringeling, F.R., Vissers, C., Jacob, F., Pokrass, M., Jimenez-Cyrus, D., Su, Y., Kim, N.S., Zhu, Y., Zheng, L., et al. (2017). Temporal control of mammalian cortical neurogenesis by m(6)A methylation. Cell *171*, 877–889.e17. https://doi.org/10.1016/j.cell.2017.09.003.

72. Kim, D., Langmead, B., and Salzberg, S.L. (2015). HISAT: a fast spliced aligner with low memory requirements. Nat. Methods *12*, 357–360. https://doi.org/10.1038/nmeth.3317.

73. Pertea, M., Pertea, G.M., Antonescu, C.M., Chang, T.C., Mendell, J.T., and Salzberg, S.L. (2015). StringTie enables improved reconstruction of a transcriptome from RNA-seq reads. Nat. Biotechnol. *33*, 290–295. https://doi.org/10.1038/nbt.3122.

74. Pertea, M., Kim, D., Pertea, G.M., Leek, J.T., and Salzberg, S.L. (2016). Transcript-level expression analysis of RNA-seq experiments with HISAT, StringTie and Ballgown. Nat. Protoc. *11*, 1650–1667. https://doi.org/10.1038/nprot.2016.095.

75. Love, M.I., Huber, W., and Anders, S. (2014). Moderated estimation of fold change and dispersion for RNA-seq data with DESeq2. Genome Biol. *15*, 550. https://doi.org/10.1186/s13059-014-0550-8.

76. Wu, X., Morishita, W., Beier, K.T., Heifets, B.D., and Malenka, R.C. (2021). 5-HT modulation of a medial septal circuit tunes social memory stability. Nature *599*, 96–101. https://doi.org/10.1038/s41586-021-03956-8.

77. Qin, H., Fu, L., Jian, T., Jin, W., Liang, M., Li, J., Chen, Q., Yang, X., Du, H., Liao, X., et al. (2022). REM sleep-active hypothalamic neurons may contribute to hippocampal social-memory consolidation. Neuron *110*, 4000–4014.e6. https://doi.org/10.1016/j.neuron.2022.09.004.

78. Jeon, Y.S., Jeong, D., Kweon, H., Kim, J.H., Kim, C.Y., Oh, Y., Lee, Y.H., Kim, C.H., Kim, S.G., Jeong, J.W., et al. (2023). Adolescent parvalbumin expression in the left orbitofrontal cortex shapes sociability in female mice. J. Neurosci. *43*, 1555–1571. https://doi.org/10.1523/JNEUROSCI.0918-22.2023.

STAR★METHODS

KEY RESOURCES TABLE

REAGENT or RESOURCE	SOURCE	IDENTIFIER
Antibodies		
rat anti-CD68, clone FA-11 (1:500)	Bio-Rad	Cat# MCA1957; RRID:AB_322219
rabbit anti-Gephyrin (1:500)	Synaptic System	Cat# 147 008; RRID:AB_2619834
chicken anti-GFAP (1:1000)	AVES	Cat# aves-GFAP; RRID:AB_2313547
rabbit anti-IBA1 (1:500)	WAKO	Cat# 019-19741; RRID:AB_839504
rat anti-LAMP2 (1:300)	Abcam	Cat# ab13524; RRID:AB_2134736
goat anti-MERTK (Mouse brain IHC 1:100, Mouse astrocyte & Brain organoid WB 1:1000)	R&D System	Cat# AF591; RRID:AB_2098565
rabbit anti-GR(NR3C1) (Mouse brain IHC/WB 1:500 Brain organoid WB 1:1000, IF 1:100)	Cell Signaling	Cat# 12041; RRID:AB_2631286
rabbit anti-PSD95 (1:500)	Invitrogen	Cat# 51-6900; RRID:AB_2533914
anti-guinea pig VGAT (1:500)	Synaptic System	Cat# 131 004; RRID:AB_887873
guinea pig anti-VGLUT1 (1:1000)	Millipore	Cat# AB5905; RRID:AB_2301751
guinea pig anti-VGLUT2	Synaptic System	Cat# 135 404; RRID:AB_887884
rabbit anti-S100β (1:500)	Abcam	Cat# ab52642; RRID:AB_882426
guinea pig anti-S100β (1:500)	Synaptic Systems	Cat# 287 004; RRID:AB_2620025
rabbit anti-TagBFP (anti-tRFP) (1:500)	Evrogen	Cat# AB233; RRID:AB_2571743
mouse anti-NeuN (1:500)	Millipore	Cat# MAB377; RRID:AB_2298772
chicken anti-NeuN (1:500)	Millipore	Cat# ABN91; RRID:AB_11205760
rabbit anti-NG2 (1:400)	Millipore	Cat # ab5320; RRID:AB_11213678
goat anti-CathepsinD (1:300)	R&D systems	Cat# AF1029; RRID:AB_2087094
rat anti-mCherry (1:800)	Invitrogen	Cat# M11217; RRID:AB_2536611
rabbit anti-c-Fos (1:500)	Cell signaling	Cat# 2250S, RRID:AB_2247211
rabbit anti-CaMKII (1:500)	Abcam	Cat# ab52476; RRID:AB_868641
mouse anti-GAD67 (1:500)	Millipore	Cat# MAB5406; RRID:AB_2278725
goat anti-SOX9 (1:200)	R&D systems	Cat# AF3075; RRID:AB_2194160
rabbit anti-PSD95 (1:100)	Cell Signaling	Cat# 3450; RRID:AB_2292883
Rabbit anti-Homer1 (1:200)	Synaptic Systems	Cat# 160 003; RRID:AB_887730
mouse anti-LAMP2 (1:500)	Santa Cruz	Cat# 18822; RRID:AB_626858
rabbit anti-MERTK (1:100)	Abcam	Cat# ab52968; RRID:AB_2143584
Donkey anti-rabbit IgG (H+L) secondary antibody, Alexa Fluor 405 (1:400)	Abcam	Cat# Ab175649; RRID:AB_2715515
Donkey anti-mouse IgG (H+L) secondary antibody, Alexa Fluor 405 (1:400)	Abcam	Cat# Ab175658; RRID:AB_2687445
Donkey anti-guinea pig IgG (H+L) secondary antibody, Alexa Fluor 488 (1:1000)	Jackson Laboratory	Cat# 706-545-148; RRID:AB_2340472
Donkey anti-mouse IgG (H+L) secondary antibody, Alexa Fluor 488 (1:1000)	Invitrogen	Cat# A-21202; RRID:AB_141607
Donkey anti-chicken IgY (IgG) (H+L) secondary antibody, Alexa Fluor 488 (1:1000)	Jackson Laboratory	Cat# 703-545-155; RRID:AB_2340375

(*Continued on next page*)

Continued

REAGENT or RESOURCE	SOURCE	IDENTIFIER
Donkey anti-rabbit IgG (H+L) secondary antibody, Alexa Fluor 488 (1:1000)	Invitrogen	Cat# A-21206; RRID:AB_2535792
Donkey anti-rat IgG (H+L) secondary antibody, Alexa Fluor 488 (1:1000)	Invitrogen	Cat# A-21208; RRID:AB_2535794
Donkey anti-rat IgG (H+L) secondary antibody, Alexa Fluor 594 (1:1000)	Invitrogen	Cat# A-21209; RRID:AB_2535795
Donkey anti-goat IgG (H+L) secondary antibody, Alexa Fluor 594 (1:1000)	Invitrogen	Cat# A-11058; RRID:AB_2534105
Donkey anti-chicken IgY (IgG) (H+L) secondary antibody, Alexa Fluor 594 (1:1000)	Jackson Laboratory	Cat# 703-585-155; RRID:AB_2340377
Donkey anti-rabbit IgG (H+L) secondary antibody, Alexa Fluor 594 (1:1000)	Invitrogen	Cat# A-21207; RRID:AB_141637
Goat anti-guinea pig IgG (H+L) secondary antibody, Alexa Fluor 647 (1:400)	Invitrogen	Cat# A-21450; RRID:AB_141882
Donkey anti-mouse IgG (H+L) secondary antibody, Alexa Fluor 647 (1:400)	Invitrogen	Cat# A-31571; RRID:AB_162542
Donkey anti-rat IgG (H+L) secondary antibody, Alexa Fluor 647 (1:400)	Abcam	Cat# Ab150155; RRID:AB_2813835
Donkey anti-goat IgG (H+L) secondary antibody, Alexa Fluor 647 (1:400)	Abcam	Cat# Ab150131; RRID:AB_2732857
beta-actin (C4) (1:1000)	Santa Cruz	Cat# sc-47778; RRID:AB_626632
m-IgGκ BP-HRP (1:1000)	Santa Cruz	Cat# sc-516102; RRID:AB_2687626
Goat anti-rabbit IgG-HRP (1:1000)	Santa Cruz	Cat# sc-2004; RRID:AB_631746
Rabbit anti-goat IgG (H+L) secondary antibody, HRP (1:5000)	Invitrogen	Cat# 31402, RRID:AB_228395
Anti-mouse IgG, HRP-linked Antibody (1:2000)	Cell signaling	Cat# 7076; RRID:AB_330924
Anti-rabbit IgG, HRP-linked Antibody (1:2000)	Cell signaling	Cat# 7074; RRID:AB_2099233
Mouse anti-GAPDH (1:1000)	Santa Cruz	Cat# sc-47724; RRID:AB_627678
Anti-Megf10 antibody (1:1000)	Millipore	Cat# ABC10; RRID:AB_11204003
Anti-rabbit PSD95 (D27E11) (Brain organoid IF 1:100, WB 1:1000)	Cell signaling	Cat# 3450; RRID:AB_2292883
Anti-rabbit Axl (C89E7) (Brain organoid WB 1:1000)	Cell signaling	Cat# 8661; RRID:AB_11217435
Donkey anti-goat IgG (H+L)	Jackson ImmunoResearch	Cat# 705-005-003; RRID:AB_2340384
Goat anti-mouse IgG+IgM (H+L)	Jackson ImmunoResearch	Cat# 115-005-044; RRID:AB_2338451
Goat anti-mouse IgM (μ-chain)	Jackson ImmunoResearch	Cat# 115-005-020; RRID:AB_2338450
Goat anti-rat IgG (H+L)	Jackson ImmunoResearch	Cat# 112-005-167; RRID:AB_2338101
Human HepaCAM antibody	R&D systems	Cat# MAB4108; RRID:AB_2117687
Integrin beta 5 monoclonal antibody (KN52)	eBioscience	Cat# 14-0497-82; RRID:AB_467288
O4 hybridoma supernatant (mouse IgM)	N/A	Bansal and Pfeiffer[62]
Purified mouse anti-rat CD45	BD Pharmingen	Cat# 554875; RRID:AB_395568

(*Continued on next page*)

Continued

REAGENT or RESOURCE	SOURCE	IDENTIFIER
Purified rat anti-mouse CD45	BD Pharmingen	Cat# 550539; RRID:AB_2174426
Chemicals, peptides, and recombinant proteins		
Vectashield Hardset™ Antifade mounting Medium with DAPI	Vector Laboratories	Cat# H-1500-10
Vectashield Hardset™ Antifade mounting Medium	Vector Laboratories	Cat# H-1400-10
Dulbecco's Modified Eagle's Medium	Welgene	Cat# LV001-05
Neurobasal medium	Gibco	Cat# 21103-049
Fetal Bovine Serum (FBS)	Gibco	Cat# 16000-044
Fetal Bovine Serum (FBS)	Welgene	Cat# S001-07
Trypsin-EDTA	Gibco	Cat# 25200-056
Penicillin-Streptomycin (10,000U/mL)	Gibco	Cat# 15140-122
L-glutamine	Gibco	Cat# 25030-081
Sodium pyruvate (100mM)	Gibco	Cat# 11360-070
N-acetyl cysteine (NAC)	Sigma	Cat# A8199
Progesterone	Sigma	Cat# P8783
Putrescine dihydrochloride	Sigma	Cat# P5780
Sodium selenite	Sigma	Cat# S5261
Apo-Transferrin, human	Sigma	Cat# T1147
Heparin-Binding EGF-like growth factor human	Sigma	Cat# E4643
1M Tris-HCl (pH 9)	Enzynomics	Cat# EBT010-250
10X DPBS	Welgene	Cat# LB 201-02
DNase1	Worthington	Cat# LS002007
Papain (suspension)	Worthington	Cat# LS003126
Trypsin	Sigma	Cat# T9935
Trypsin inhibitor	Worthington	Cat# LS0003068
L-cystein hydrochloride monohydrate	Sigma	Cat# C7880
10X EBSS	Sigma	Cat# E7510
Bovine serum albumin (BSA)	Goldbio	Cat# A-420-100
D-(+)-Glucose	Sigma	Cat# G7021
Sodium bicarbonate	J.T.Baker	Cat# 3506-01
EDTA disodium	LPS solution	Cat# EDTA05
Griffonia (Bandeiraea) simplicifolia lectin 1 (BSL1)	Vector Laboratories	Cat# L-1100
Poly-D-lysine	Sigma	Cat# P6407
Sucrose	Sigma	Cat# S1888
Dithiothreitol (DTT)	Amresco	Cat# 0281
Percoll	GE healthcare life sciences	Cat# 17-0891-01
Tris	LPS solution	Cat# TRI05
Sodium chloride	Sigma	Cat# S7653
HEPES, minimum 99.5% titration	Sigma	Cat# H3375
Potassium chloride	Sigma	Cat# P9541
Magnesium chloride, anhydrous	Sigma	Cat# M8266
Sodium phosphate monobasic	Sigma	Cat# S5011
pHrodo succinimidyl ester	Molecular probe	Cat# P36600
Sodium carbonate	Duksan science	Cat# D949
DMSO	LPS solution	Cat# DMSO100
Approved & Investigational drugs	Korea Chemical Bank (KCM)	Provided by KCM
Corticosterone	Sigma	Cat# 27840
Hydrocortisone	Sigma	Cat# H0888

(*Continued on next page*)

Continued

REAGENT or RESOURCE	SOURCE	IDENTIFIER
Eplerenone	Tocris	Cat# 2397
Mifepristone	Tocris	Cat# 1479
Lipofectamine 3000	Thermo Fisher	Cat# L3000008
DMEM/F12	Invitrogen	Cat# 12500062
Knock-Out™ SR	Invitrogen	Cat# 10828028
Sodium bicarbonate	Sigma	Cat# S6297
L-glutamine	Sigma	Cat# 49419
Nonessential amino acids	Invitrogen	Cat# 11140050
Penicillin-streptomycin	Invitrogen	Cat# 10378016
β-mercaptoethanol	Sigma	Cat# 63689
FGF2	R&D systems	Cat# 233-FB
Collagenase type IV	Invitrogen	Cat# 17104019
Y-27632	A.G. Scientific	Cat# Y-1004
SB431542	Cayman Chemical	Cat# 13031
Dorsomorphin	A.G. Scientific	Cat# D-1310
B-27 supplement without vitamin A	Invitrogen	Cat# 12587010
GlutaMAX	Invitrogen	Cat# 35050038
EGF	Peprotech	Cat# AF-100-15
BDNF	Peprotech	Cat# 450-02
NT3	Peprotech	Cat# 450-03
Terrell™ Isoflurane	Piramal healthcare	N/A
4-hydroxytamoxifen	Sigma	Cat# H6278
Absolute ethanol	Merck	Cat# 100983
Koliphor EL	Sigma	Cat# C5135
(Avertin) 2,2,2-Tribromethanol	Sigma	Cat# T48402
(Avertin) 2-Methyl-2-butanol	Sigma	Cat# 240486
4% paraformaldehyde (4% PFA)	Wako	Cat# 163-20145
4% formalin solution	Sigma	Cat# HT5012
BSA	GenDEPOT	Cat# A0100
FSC 22 Frozen Section Media	Leica biosystems	Cat# 3801480
Optimal Cutting Temperature (OCT) compound	SAKURA	Cat# 4583
Fluorescent mounting medium	Dako	Cat# S302380-2
Triton™ X-100	Sigma	Cat# X100
Triton X-100	Sigma	Cat# T8787
Tween® 20	Sigma	Cat# P1379
EzRIPA lysis buffer	Atto	Cat# WSE-7420
RIPA buffer	GenDEPOT	Cat# R4100-010
Protease and Phosphatase inhibitor cocktail	GenDEPOT	Cat# P3300-001
PhosSTOP™ EASYpack	Roche	Cat# 04906845001
cOmplete™ Protease inhibitor cocktail	Roche	Cat# 04693116001
5X SDS-PAGE loading buffer	LPS solution	Cat# CBS002
Precast Gradient polyacrylamide gel	Bio-Rad	Cat# BR456-1095
Difco skim milk	BD	Cat# 232100
10X Tris Glycine SDS buffer	LPS solution	Cat# CBT015
20X Tris-buffered saline (TBS)	LPS solution	Cat# CBT008
Methanol	Merck	Cat# 1.06009.1011
Glycine	LPS solution	Cat# GLY05
TRIzol™ reagent	Invitrogen	Cat# 15596026

(*Continued on next page*)

Continued

REAGENT or RESOURCE	SOURCE	IDENTIFIER
Critical commercial assays		
RNeasy Mini Kit	Qiagen	Cat# Qia-74134
TOPscript reverse transcriptase	Enzynomics	Cat# RT002L
SYBR Green RT-PCR master mix	Toyobo	Cat# TOQ-201
NucleoBond Xtra Midi kit	Macherey-Nagel	Cat# MN-740410.100
Quick Start™ Bradford Protein Assay Kit 2	Bio-Rad	Cat# 5000202
SuperSignal West Dura Extended Duration Substrate	Thermo Fisher	Cat# 37071
Immobilon Western Chemiluminescent HRP Substrate	Millipore	Cat# WBKLS0500
Myelin removal beads	Miltenyi Biotec	Cat# 130-096-733
Anti-ACSA-2 microbead kit	Miltenyi Biotec	Cat# 130-097-679
Quant-it™ RiboGreen RNA Assay Kit	Invitrogen	Cat# R11490
TruSeq® Standard mRNA Library prep	Illumina	Cat# 20020595
SuperScript™ II Reverse Transcriptase	Invitrogen	Cat# 18064022
KAPA Library Quantification Kit – Illumina® Platforms	KAPABIOSYSTEMS	Cat# KR0405
D1000 ScreenTape	Agilent Technologies	Cat# 5067-5582
Deposited data		
Raw and analyzed RNA sequencing data	This paper	GEO: GSE234945 and See Tables S2, S3, and S4
Experimental models: Cell lines		
HEK 293 T cell	Korean Cell Line Bank	Cat# 293[HEK-293]
Human embryonic stem cells (hESCs, H9)	WiCell,	Cat# WA09
Experimental models: Organisms/strains		
Rat: Sprague-Dawley	NIH	NTac:SD
Mouse: C57BL/6	The Jackson Laboratory	C57BL/6NTac
Mouse: B6;129-*Mertk*^{tm1Grl}/J	Gift from Ben Barres	Chung et al.[6]
Mouse: *Megf10*$^{tm1(KOMP)Vlcg}$	Gift from Ben Barres	Chung et al.[6]
Mouse: B6N.FVB-Tg(Aldh1l1-cre/ERT2)1Khakh/J	The Jackson Laboratory	Cat# 031008
Mouse: B6.Cg-*Nr3c1*$^{tm1.1Jda}$/J	The Jackson Laboratory	Cat# 021021
Mouse: *loxp floxed Mertk (Mertk*$^{f/f}$*)*	N/A	Park et al.[12]
Mouse: B6.129P2(Cg)-*Cx3cr1*$^{tm2.1(cre/ERT2)Litt}$/WganJ	Gift from Seyun Kim	Park et al.[12]
Oligonucleotides		
Nr3c1 FW 5'-GAAAAGCCATCGTCAAA AGGG-3' and RV 5'-TGGAAGCAGTAG GTAAGGAGA-3'	van der Doelen et al.[63]	N/A
Nr3c2 FW 5'-TCGCTTTGAGTTGGAGA TCG-3' and RV 5'-ACGAATTGAAGGC TGATCTGG-3'	van der Doelen et al.[63]	N/A
Mertk FW 5'-CTGCTTCTGCGGGTTTG TTC-3' and RV 5'-GGCTTTGCAAGGTA AGCTCG-3'	Liddelow et al.[64]	N/A
Megf10 FW 5'-TACCGCCATGGGGAG AAAAC-3' and RV 5'-TTATCAGCGCA GTGAGGGAC-3'	Liddelow et al.[64]	N/A
Axl FW 5'-GACACCCCCGAGGTAC TTATG-3' and RV 5'-TGGGGGTTCA CTCACTGGG-3'	Liddelow et al.[64]	N/A
Tfeb FW 5'-GTGCTGAAGGTGCAGT CCTA-3' and RV 5'-CCGTAGGTCTC GGACAGGTA-3	NCBI Primer-BLAST	N/A
Recombinant DNA		
pAAV-hSyn-PSD95Δ1.2-tagBFP-EGFP	Subcloned	N/A

(*Continued on next page*)

Continued		
REAGENT or RESOURCE	SOURCE	IDENTIFIER
pAAV-hSyn-Gq-mCherry	Addgene	Cat# 50474
pAAV-CamK2a-PSD95 Δ1.2-mCherry-EGFP	Subcloned	N/A
pAAV-GAD67-PSD95 Δ1.2-mCherry-EGFP	Subcloned	N/A
pLV-GfaABC1D-Mertk-IRES-ZsGreen	Subcloned	N/A
Software and algorithms		
CFX Maestro 1.1	Bio-Rad	Version 4.1.2433.1219
SnapGene®	SnapGene	Version 4.0.8
Imaris x64	Oxford Instruments	Version 9.5.1
FIJI (Image J)	NIH	Version 1.52p
GraphPad Prism	GraphPad	Version 7.00
EthoVision XT	Noldus	Version 14.0.1326
Illumina NovaSeq platform	Illumina	https://www.illumina.com
MATLAB & code	MathWorks	Kim et al.[65]
Klusters software	Developed at the Buzzsaki Lab	http://neurosuite.sourceforge.net/
Distance analysis (DiAna) plugin	N/A	Gilles et al.[66]
ZEISS Image acquisition software, ZEN v2.3 from LSM780 and LSM880	ZEISS	https://www.zeiss.com/
IncuCyte S3	Sartorius	Version 2018B
g:Profiler	g:Profiler	https://biit.cs.ut.ee/gprofiler/
R 3.6.1	R Core Team	https://www.r-project.org
Other		
Glass Replacement Capillaries for Microdispensers	Drummond Scientific	Cat# 3-000-210-G
Open-Top Thinwall Ultra-Clear Tube	Beckman Coulter	Cat# 344059
SW 41 Ti Swinging-Bucket Rotor	Beckman Coulter	Cat# 331362
Optima XE-100 ultracentrifuge	Beckman Coulter	Cat# A94516
100kDa Amicon® Ultra15 centrifugal Filter Unit	Millipore	Cat# UFC910024
Electrodes for Electroporation	Nepa Gene	Cat# CUY650P5
NEPA21 Super Electroporator	Nepa Gene	Cat# NPG-NEPA21
Cryostat	Leica Biosystems	Cat# CM1860
Microslideglass	Matsunami	Cat# HMA-MAS-11
Cover glass	Vector Laboratories	Cat# 01 012 22
PVDF membrane	Atto	Cat# WSE-4053
Filter paper	Atto	Cat# CB-09A
LS columns	Miltenyi Biotec	Cat# 130-042-401
MS columns	Miltenyi Biotec	Cat# 130-042-201
CFX connect Real-Time PCR Detection system	Bio-Rad	https://www/bio-rad.com/

RESOURCE AVAILABILITY

Lead contact

Further information and requests for resources and reagents should be directed to the lead contact, Won-Suk Chung (wonsuk.chung@kaist.ac.kr).

Materials availability

All data are available upon request. For further inquiries, please contact the Lead Contact.

Data and code availability

- RNA-seq data have been deposited at GEO and are publicly available as of the date of publication. Accession numbers are listed in the key resources table.
- This paper does not report original code.
- Any additional information required to reanalyze the data reported in this paper is available from the lead contact upon request.

EXPERIMENTAL MODEL AND STUDY PARTICIPANT DETAILS

Mice

All experimental procedures performed in the study were approved by the Institutional Animal Care and Use Committee (IACUC) of the Korea Advanced Institute of Science and Technology (KAIST). B6;129-*Mertk*^{tm1Grl}/J mice and *Megf10*$^{tm1(KOMP)Vlcg}$ mice were obtained from the Barres laboratory.[6] FVB-Tg(Aldh1l1-cre/ERT2)1Khakh/J mice and B6.Cg-*Nr3c1*$^{tm1.1Jda}$/J mice were obtained from the Jackson Laboratory. To generate astrocyte-specific GR (*Nr3c1*) cKO mice, Tg(Aldh1l1-cre/ERT2)1Khakh/J mice were crossed with B6.Cg-*Nr3c1*$^{tm1.1Jda}$/J mice. To ablate *Mertk* specifically in astrocytes and microglia, *loxp floxed Mertk (Mertk*$^{f/f}$*)* mice[12] were crossed with Tg(Aldh1l1-cre/ERT2)1Khakh/J and B6.129P2(Cg)-*Cx3cr1*$^{tm2.1(cre/ERT2)Litt}$/WganJ mice (gifted from Dr Seyun Kim), respectively. C57BL/6 mice and Sprague–Dawley (SD) rats were purchased from Samtaco and Daehan BioLink (DBL). All mouse lines were maintained on the C57BL/6 background and 2-20-week-old mice were used. For the *in vitro* experiment, western blotting, IUE, and behavioral tests, mice of both sexes were used. For RNAseq and *in vivo* recording, only male mice were used. For confocal imaging, either both sexes or only male were used. With mice of both sexes, GR and MERTK correlation analysis/S100β^{+} OPC analysis/microglial synapse engulfment analysis/*Cx3cr1-creERT2; Mertk*$^{f/f}$ mice validation were performed. With only male mice, synaptic density/GR, MERTK, lysosomes, and engulfed synapses in astrocytes/reactive gliosis/GR, MERTK, and lysosomes in microglia/c-Fos analysis were performed.

METHOD DETAILS

Synaptosome purification and pHrodo conjugation

Synaptosomes were purified from twelve-week-old C57BL/6J mice using a Percoll density gradient[67] with several modifications to improve the yield.[13] Briefly, the olfactory bulb and cerebellum were resected from the whole brain. The remaining brains were homogenized using a glass homogenizer with homogenization buffer (0.32 M sucrose, 1 mM EDTA, 5 mM Tris and 0.25 mM DTT (pH 7.4)). The supernatants of the homogenates were obtained by centrifugation and added to Percoll (GE Healthcare) gradient solutions (Percoll, 0.32 M sucrose, 1 mM EDTA, 0.25 mM DTT and 5 mM Tris (pH 7.4)) in ultracentrifugation tubes. The synaptosome-containing fraction between 10% and 23% Percoll gradients was carefully collected. To remove the remaining Percoll solution from the collected synaptosomes, the synaptosomes were further centrifuged in sucrose/EDTA buffer (0.32 M sucrose, 1 mM EDTA, and 5 mM Tris (pH 7.4)). The synaptosome pellets were resuspended in 5% DMSO containing isotonic buffer (140 mM NaCl, 10 mM HEPES, 10 mM glucose, 3 mM KCl, 1.2 mM MgCl2, and 1.2 mM NaH2PO4 (pH 7.4)) and stored at -80°C until pHrodo conjugation. To obtain pH-sensitive fluorogenic synaptosomes, 0.6 mg of synaptosomes were incubated with 2 μl of pHrodo Red, succinimidyl ester (Invitrogen) and 200 μl of 0.1 M sodium carbonate buffer (pH 9.0) for 2 hours at room temperature (RT) with gentle agitation. To remove the unconjugated pHrodo Red, the pHrodo-Syn pellets were further washed multiple times by centrifugation in 1X Dulbecco's phosphate-buffered saline (DPBS, Welgene). Then, 0.6 mg of the pH-Syn pellet was resuspended in 200 μl of 5% DMSO/DPBS and stored at -80°C.

In vitro live-imaging phagocytosis assay for compound screening

Astrocytes were purified from the cortices of P7-P10 SD rats by immunopanning.[16] Briefly, the cerebral cortices were dissected out in DPBS and digested with papain (Worthingtons). The digested cortices were triturated serially with 5 mL and 1 mL pipettes in to dissociate them into single cells. Then, the single-cell suspension was immunopanned in cell type-specific antibody-coated dishes. Finally, astrocytes were collected from Integrin β5 (eBioscience)-coated dishes with trypsin (Sigma–Aldrich) and suspended in astrocyte growth medium (AGM) for cell counting and plating. The AGM consisted of 50% neurobasal medium (Gibco), 50% DMEM (Welgene), 100 U/ml penicillin & 100 μg/ml streptomycin (Gibco), 292 μg/ml, L-glutamine (Gibco), 1 mM sodium pyruvate (Gibco), 5 μg/ml N-acetyl cysteine (Sigma–Aldrich), 1× SATO and 5 ng/ml HBEGF (Sigma–Aldrich). For screening of FDA-approved clinical compounds (Korea Chemical Bank), 50 μl of AGM containing 5∼6x10^{3} purified astrocytes was added to PDL-coated 384-well microplates by using an automated liquid handling workstation (Biomek). After 40 min, 40 μl of medium was aspirated to remove the unattached cells, and 90 μl of fresh AGM was added. At 5-8 days *in vitro* (DIV), when the astrocytes reached approximately 80∼90% confluence, 80∼85 μl of AGM was replaced with 90 μl of fresh AGM containing pHrodo-Syns (22.5 μg/ml) and clinical compounds (final concentrations of 0.5, 1, and 1.5 μM for independent experiments). After 40 min, 95 μl of pHrodo-Syn-containing AGM was replaced with 95 μl of fresh AGM and clinical compounds. The plates were placed in the IncuCyte system (Satorius) and imaged every 2 hours for 3-5 days. In each experiment, 6 images were collected per group at a single time point and all 6 data points were plotted. The phagocytic index was measured as the area of red fluorescence emitted from the engulfed pH-Syns in astrocytes, normalized to the area of astrocytes in the imaging fields.

In vitro live-imaging phagocytosis assay for stress hormones

Astrocytes were purified from P7-P10 SD rats as described above. Purified astrocytes ($5x10^4$) were plated in 24-well plates. Stocks of 10 mM corticosterone (Sigma–Aldrich), mifepristone (Tocris), and eplerenone (Tocris) in DMSO (LPS Solution) were serially diluted to a concentration of 100 μM using 50%, 25%, and 12.5% DMSO/DPBS. At 7-10 DIV, astrocytes were preincubated with AGM containing combinations of compounds (DMSO control; corticosterone alone; corticosterone and eplerenone; corticosterone and mifepristone; or corticosterone, eplerenone and mifepristone) for 24 hours. The final concentration of corticosterone was 1 μM, and the final concentration of eplerenone and mifepristone was 2 μM. Then, the medium was replaced with fresh AGM containing pHrodo-Syns (30 μg/ml) and compounds. After 40 min of pHrodo-Syns incubation, the astrocytes were washed twice with DPBS to remove the unbound pHrodo-Syns, and fresh AGM containing compounds were added. Then, the plates were placed in the IncuCyte system (Satorius) and imaged every 2 hours for 3-5 days. The phagocytic index was measured as described above. To identify the phagocytic receptors involved in stress hormone-induced astrocytic phagocytosis, mouse astrocytes were purified from WT (C57BL/6J), *Mertk*$^{-/-}$, and *Megf10*$^{-/-}$ mice using the modified immunopanning method for mice.[68] Mouse astrocytes ($5x10^4$) were plated in 48-well plates and maintained in AGM supplemented with astrocyte-conditioned medium (ACM, 3 μg/ml, see below). Treatment with pH-Syns (30 μg/ml) and compounds (final concentration of 2 μM for corticosterone, eplerenone and mifepristone), imaging analysis, and phagocytic index measurement were conducted as described above for rat astrocytes.

Astrocyte-Conditioned Medium (ACM)

Astrocytes were purified from the cortices of P7-P10 SD rats as described above, and $1x10^6$ cells were plated in 100 mm dishes. When the cells reached 90-100% confluence, the AGM was replaced with conditioning medium (50% neurobasal, 50% DMEM, 100 U/ml penicillin, 100 μg/ml streptomycin, 292 μg/ml L-glutamine, 1 mM sodium pyruvate, and 5 μg/ml N-acetyl cysteine). After 5-7 days of incubation, the conditioning medium was collected and concentrated in a 30 kDa Vivaspin tube (Sartorius). The ACM concentration was measured by the Bradford assay (Bio–Rad).

Real-time PCR (qPCR)

To obtain RNA from astrocytes, rat astrocytes were purified from the rat cortex as described above, and $5x10^5$ cells were plated in 60 mm culture dishes. When the astrocytes reached 80-90% confluence, compounds (final concentration of 1 μM for corticosterone and 2 μM for mifepristone) and pHrodo-Syns (30 μg/ml) were applied as described above. At 24 or 48 hours after pH-Syn treatment, total RNA was extracted using a RNeasy Mini Kit (Qiagen) following the manufacturer's instructions. A total of 800 ng of total RNA was used for reverse transcription using TOPscript reverse transcriptase (Enzynomics) according to the manufacturer's instructions. qPCR was performed using SYBR Green RT–PCR master mix (Toyobo) and the CFX Connect Real-Time PCR Detection System (Bio–Rad). The mRNA expression of the target genes was normalized to that of GAPDH. The following qPCR primers were used:[64,63] *Nr3c1*, 5-GAAAAGCCATCGTCAAAAGGG-3' and 5'-TGGAAGCAGTAGGTAAGGAGA-3'; *Nr3c2*, 5'-TCGCTTTGAGTTG GAGATCG-3' and 5'-ACGAATTGAAGGCTGATCTGG-3'; *Mertk*, 5'-CTGCTTCTGCGGGTTTGTTC-3' and 5'-GGCTTTGCAAGGTA AGCTCG-3'; *Megf10*, 5'-TACCGCCATGGGGAGAAAAC-3' and 5'-TTATCAGCGCAGTGAGGGAC-3'; *Axl*, 5'-GACACCCCCGAGGT ACTTATG-3' and 5'-TGGGGGTTCACTCACTGGG-3'; *Tfeb*, 5'-GTGCTGAAGGTGCAGTCCTA-3' and 5'-CCGTAGGTCTCGGACA GGTA-3'. The *Tfeb* primers were designed by using the NCBI Primer-BLAST program (http://www.ncbi.nlm.nih.gov/tools/primer-blast/).

Lentivirus (LV) production

An LV vector encoding MERTK-IRES-ZsGreen under the control of the GfaABC1D promoter was cotransfected with envelope and packaging vectors (VSV-G, Gag-Pol, Rev, and Tat) into HEK293T cells using Lipofectamine 3000 (Thermo Fisher) following the manufacturer's instructions. The supernatants were collected 24 and 52 hours posttransfection. To obtain a high titer, the supernatants were preconcentrated to 12.5∼13 ml by centrifugation at 3,300 × g in a 100 kDa Amicon tube (Millipore). The concentrated supernatants were then transferred to a 13.5 ml Ultra-clear centrifuge tube (Beckman Coulter) on top of 0.5 ml of 20% sucrose/DPBS. The LV particles were centrifuged at 33,000 rpm using an Optima XE-100 ultracentrifuge (Beckman Coulter) and an SW 41 Ti Swinging-Bucket rotor (Beckman Coulter). The LV particles were resuspended in DPBS. To remove the insoluble fraction, the resuspended LV particles were centrifuged at 2000 x g for 5 min at 4°C. The supernatant was then aliquoted and stored at -80°C. For all centrifuge steps, the temperature was set at 4°C.

Maintenance of human embryonic stem cells

Experiments using human embryonic stem cells (hESCs, H9, Sex: XX)[69] were approved by the KAIST Institutional Review Board (approval No.: KH2018-114). hESCs were maintained in ESC medium on a mitomycin-C (A.G. Scientific)-treated mouse embryonic fibroblast layer at 37 °C with 5% CO2. The ESC medium consisted of 80% basal DMEM/F12 (Invitrogen) plus 20% Knock-Out™ SR (Invitrogen) supplemented with 1.2 g/L sodium bicarbonate (Sigma–Aldrich), 1 mM L-glutamine (Sigma–Aldrich), 1% nonessential amino acids (Invitrogen), 1% penicillin–streptomycin (Invitrogen), 0.1 mM β-mercaptoethanol (Sigma–Aldrich), and 10 ng/ml FGF2 (R&D Systems). The medium was changed daily to retain the pluripotency of the hESCs. To expand the cell population, undifferentiated hESC colonies were passaged at a ratio of 1:5 through dissection into small clumps using 10 mg/ml collagenase type IV (Invitrogen) every 6 days and cultured as described above.

Development of cortical organoids from human embryonic stem cells

Human cortical organoids (hCOs) were generated from hESCs as previously described.[70] Briefly, an hESC colony was dissected into approximately 10 clumps using a syringe needle, transferred to low-attachment petri dishes (SPL Lifesciences), and incubated in FGF2-free ESC medium supplemented with 10 μM Y-27632 (A.G. Scientific) for 24 hours. For neural induction, the clumps were incubated in FGF2-free ESC medium supplemented with 5 μM SB431542 (Cayman Chemical) and 10 μM dorsomorphin (A.G. Scientific) for 5 days with daily medium changes. Suspended spheroids were cultured in neural medium (NM) for 10 days with daily medium changes. The NM consisted of neurobasal medium (Invitrogen), 1× B-27 supplement without vitamin A (Invitrogen), 1× GlutaMAX (Invitrogen), 20 ng/ml FGF2, and 20 ng/ml EGF. Then, the spheroids were incubated in the same medium, and the medium was changed every other day for 9 days. To induce the differentiation of neural precursor cells into neurons, the cells were cultured in NM supplemented with 20 ng/ml BDNF (Peprotech) and 20 ng/ml NT3 (Peprotech) instead of FGF2 and EGF for 19 days. After 43 days of culture, the hCOs were maintained in NM medium without any growth factors. The medium was changed every 4 days.

In utero electroporation (IUE)

IUE was performed as previously described[71] with minor modifications. In brief, timed-pregnant C57BL/6J mice were anesthetized on embryonic day 15.5 (E15.5) with isoflurane (induction, 3.0%; surgery, 2.0%), and the uterine horns were exposed by laparotomy. Then, approximately 2.0 to 3.0 μl of DNA plasmids (hSyn-PSD95Δ1,2-tagBFP-EGFP (2.0 μg/μl in DPBS), hSyn-Gq-mCherry (2.0 μg/μl in DPBS), CaMKIIα - PSD95Δ1,2-mCherry-EGFP (2.0 μg/μl in DPBS), and GAD67- PSD95Δ1,2-mCherry-EGFP (2.0 μg/μl in DPBS)) were injected through the uterine wall into one of the lateral ventricles of each embryo with a 10 μm diameter glass microcapillary tube (Drummond). PSD95Δ1,2, which has a systemic deletion of PDZ domain of PSD-95, does not affect the ability of PSD95Δ1,2 to localize to dendritic spines but minimize the undesirable effects of PSD-95 overexpression.[29,30] After soaking the uterine horn with 5% penicillin/streptomycin-containing DPBS solution, the embryo's head was carefully positioned between tweezer-type platinum plate electrodes (Nepa Gene, CUY650P5), and a total of eight electrical pulses (poring pulse: voltage 43.0: V, pulse length: 30.0 msec, pulse interval: 450.0 msec, number of pulses: 3, decay rate: 10%, polarity: +; transfer pulse: voltage: 43.0 V, pulse length: 50.0 msec, pulse interval: 450.0 msec, number of pulses: 5, decay rate: 40%, polarity: +) were delivered with a NEPA21 Super Electroporator (Nepa Gene). Immediately after electroporation, the uterine horns were placed back in the abdominal cavity and the wound was sutured to allow normal development of the embryos.

Early social deprivation (ESD) protocol and 4-hydroxytamoxifen (4-OHT) injection

The ESD protocol was performed as previously described.[27] Briefly, after female WT (C57BL/6J) or Cre^- AGR, AMer and MMer mice were impregnated by male Cre^+ mice, and the pregnant female mice were separately caged with chow, unlimited water and nesting blocks. Pups in the ESD group were separated from their mothers and control littermates for 3 hours a day from P1 to P14. During stress induction, the pups in the ESD group were placed in a 6-chambered acryl box with clean bedding and transferred to an isolated room with a constant temperature and humidity. Then, at P5-P7, 75 μg of 4-OHT (Sigma–Aldrich) per 1 g of body weight was administered to all littermates by intraperitoneal (i.p.) injection to generate control and ESD-exposed Cre^-, AGR cKO, AMer cKO, and MMer cKO mice. To make 4-OHT stock, 50 mg of 4-OHT was dissolved in 1.25 ml of absolute ethanol (Merck) and 1.25 ml of Kolliphor EL (Sigma) to 20 mg/ml and stored at -80°C until use. The 100 μl of 20 mg/ml stock was diluted in 300 μl of 1X DPBS to 5 mg/ml before use. The 5 mg/ml 4-OHT was used up to 1 week.

Immunohistochemistry (IHC) and image analysis

Mice

Mice were anesthetized with avertin (0.2 g/ml, Sigma–Aldrich) by i.p. injection. The mice were perfused with DPBS followed by 4% paraformaldehyde (PFA, Wako). The isolated brains were postfixed in 4% PFA overnight at 4°C and then transferred to 30% sucrose (Sigma–Aldrich)/DPBS for 48 hours. The brains were embedded in Optimal Cutting Temperature (OCT) compound (Leica microsystems) and quick-frozen on dry ice. Four 30 μm brain sections were obtained with a cryostat (Leica MICROSYSTEMS) and placed in DPBS in one well of a 48-well plate. The sections were blocked with blocking solution for 1 hour at RT and incubated with primary antibodies for 48 hours at 4°C with gentle agitation. The blocking solution consisted of 4% bovine serum albumin (BSA, Goldbio), 0.3∼1% Triton X-100 (Sigma), and DPBS. The following primary antibodies were used: rabbit anti-S100β (1:500, Abcam), guinea pig anti-S100β (1:500, Synaptic Systems), chicken anti-GFAP (1:1000, Aves Labs), rabbit anti-NG2 (1:400, Millipore), rat anti-LAMP2 (1:300, Abcam), goat anti-CathepsinD (1:300, R&D systems), rabbit anti-GR (1:500, Cell signaling), goat anti-MERTK (1:100, R&D systems), rabbit anti-IBA1 (1:500, WAKO), rat anti-CD68 (1:500, BMS), rabbit anti-TagBFP (1:500, Evrogen), chicken anti-GFP (1:2500, Aves Labs), rat anti-mCherry (1:800, Invitrogen), mouse anti-NeuN (1:500, Millipore), chicken anti-NeuN (1:500, Millipore), anti-rabbit c-Fos (1:500, Cell signaling), rabbit anti-PSD95 (1:500, Invitrogen), guinea pig anti-VGLUT1 (1:1000, Millipore), anti-guinea pig VGAT (1:500, Synaptic Systems), anti-rabbit Gephyrin (1:500, Synaptic Systems), rabbit anti-CaMKII (1:500, Abcam), mouse anti-GAD67 (1:500, Millipore), rabbit anti-Homer1 (1:200, Synaptic Systems). The brain sections were washed in DPBST (DPBS containing 0.1% Tween 20) and treated with Alexa fluorophore-conjugated secondary antibodies (1:1000 Alexa Fluor 488 & Alexa Fluor 594, 1:400 Alexa Fluor 405 & Alexa Fluor 647, Abcam, Jackson Laboratory, and Invitrogen) in blocking solution for 2 hours at RT with gentle agitation. The sections were washed five times with DPBST and then mounted on a slide glass (Matsunami) with a coverglass and Vectashield with or without DAPI (Vector Lab).

hCOs

hCOs were fixed in 4% formalin solution (Sigma–Aldrich) for 24 hours and placed in 30% sucrose/DPBS for 72 hours at 4°C. Subsequently, the samples were embedded in OCT compound (Tissue-Tek), sectioned at 20 μm using a cryostat and directly attached to glass slides. The slices were blocked in blocking solution (PBS containing 3% BSA and 0.5% Triton X-100) for 2 hours at RT. The samples were then incubated with primary antibodies in blocking solution overnight at 4°C. The following primary antibodies were used: chicken anti-GFAP (1:1000, Aves Labs), rabbit anti-GR (1:100, Cell Signaling), goat SOX9 (1:200, R&D systems), rabbit anti-PSD95 (1:100, Cell Signaling), mouse anti-LAMP2 (1:500, Santa Cruz) and mouse anti-MERTK (1:100, Santa Cruz). After washing with PBS, the samples were treated with Alexa fluorophore-conjugated secondary antibodies (1:300∼1:1000 Alexa Fluor 488, 1:500 Alexa Fluor 594, 1:1000 Alexa Fluor 647, Abcam) in blocking solution for 2 hours at RT. After washing with PBS, fluorescent mounting medium (Dako) was used for mounting with cover glass.

Images were acquired with a Nikon upright microscope and Zeiss LSM 780 inverted and Zeiss LSM 880 upright confocal microscopes. Confocal imaging analysis were performed with two different brain slices per a mouse. For each brain slice, two sets of confocal z-stacks containing multiple single-plane confocal images were obtained from the regions of interest (ROIs). Imaging analysis was performed using individual single plane confocal images, which were averaged to produce one data points per a z-stack, thus producing four data points per a mouse. All images and representative z-stack images were processed using Fiji (ImageJ). For colocalization analysis and synaptic density measurement, the Distance Analysis (DiAna) plugin[66] was used. For 3D reconstruction, Imaris software was used.

For colocalization analysis, the volumes of GR, lysosomes, MERTK, PSD95, Homer1 and glial cells were isolated with a set value using DiAna plugin. To set the correct value, threshold was adjusted to cover fluorescent signals and the remaining background signals were excluded based on puncta size. The same set values were used for each group of images to get a consistent data. With the isolated signals after thresholding, the colocalized GR, lysosomes, MERTK or PSD95 within glial cells were analyzed by using DiAna plugin.

To compensate the differences in the area of astrocytes in the quantifying images, the area of $LAMP2^+$ lysosomes, $PSD95^+$ or $Homer1^+$ puncta inside astrocytic lysosomes, and MERTK localized in astrocytes was normalized by the area of astrocytes.

To compensate the differences in the area of microglia in the quantifying images, the colocalized $CD68^+$ lysosomes, $PSD95^+$ puncta in microglial lysosomes, MERTK area in microglia was normalized by the area of microglia.

To compensate the differences in efficiency of *in utero* electroporation, $tagBFP^+$ or $mCherry^+$ alone puncta in lysosomes was normalized by the area of astrocytes or microglia as well as by the area of total intact synapses labeled by the transgenes.

To compensate the differences in cell numbers in the quantifying images, the colocalized GR and c-Fos area were normalized by the number of cells in a ROI.

The AU (Average Unit) was calculated by dividing every value by the mean value of control (or Cre^- control).

Western blotting

Mouse astrocytes

WT (C57BL/6J) pups were subjected to ESD as described above. After the final ESD session on P14, the cortices of control and ESD mice were isolated and dissected in DPBS. To purify astrocytes, the immunopanning method was used as described above. Astrocyte pellets were lysed in EzRIPA lysis buffer (Atto) supplemented with phosphatase inhibitor (Roche) and protease inhibitor (Roche) for 1 hour at 4°C with gentle agitation. After lysis, the lysates were centrifuged at 15,000 rpm for 10 min at 4°C, and the supernatants were transferred to a new tube. The concentration of proteins extracted from the astrocytes was quantified by the Bradford assay (Bio–Rad), and the proteins were mixed with 5× SDS–PAGE loading buffer (LPS solution). The protein samples were loaded on a gradient polyacrylamide gel (Bio Rad) and transferred to a methanol-activated PVDF membrane (Atto). For blocking, the membrane was transferred to a cassette containing 3% Difco skim milk (BD)/TBST (Tris-buffered saline containing 0.1% Tween 20) for 1 hour at RT with gentle agitation. The membranes were incubated with primary antibodies in 1% skim milk/TBST overnight at 4°C with gentle agitation. The membranes were washed with TBST three times at RT with gentle agitation and incubated with HRP-conjugated secondary antibodies (1:1000 for mouse and rabbit, 1:5000 for goat, Santa Cruz and Invitrogen) in 1% skim milk/TBST for 1 hour with gentle agitation. The membranes were washed three times in TBST at RT with gentle agitation. The antibody-bound proteins were visualized by exposure to SuperSignal West Dura Extended Duration Substrate (Thermo Fisher).

hCOs

hCOs were sonicated in RIPA buffer (GenDEPOT) containing a protease and phosphatase inhibitor cocktail (GenDEPOT) using a sonicator (20 amplitude, 2 secs) and lysed at 4 °C for 1 hour with gentle agitation. After centrifugation at 13,000 × g for 15 min, the supernatant was collected. The protein concentration was measured using a Bradford assay (Bio–Rad), and the proteins were denatured in SDS–PAGE loading buffer at 95°C for 5 min. The proteins (1 mg/ml) were resolved on a 10% SDS–PAGE gel by electrophoresis and then transferred to a nitrocellulose membrane (Whatman). The samples were blocked in 5% BSA (GenDEPOT)/TBST for 1 hour at RT. Antibody incubation and band detection were performed as described above. The primary antibody-bound proteins were treated with HRP-conjugated secondary antibodies (1:2000, Cell signaling) and visualized by exposure to Immobilon Western Chemiluminescent HRP substrate (Millipore).

The following primary antibodies were used: mouse anti-GAPDH (1:1000, Santa Cruz), mouse anti-β-actin (1:1000, Santa Cruz), rabbit anti-GR (1:1000, Cell Signaling), and goat anti-MERTK (1:1000, R&D Systems) for mouse astrocytes; rabbit anti-MERTK

(1:1000 Abcam) and rabbit anti-MEGF10 (1:1000, Sigma–Aldrich), rabbit anti-AXL (1:1000, Cell signaling), rabbit anti-PSD95 (1:1000, Cell Signaling) for cortical organoids. The protein bands were analyzed with Fiji software (ImageJ).

Sample preparation for RNA sequencing

To obtain samples for RNAseq, the immunopanning method using Miltenyi Biotec beads was performed with minor modifications. Briefly, the cortices of mice from the four groups (Cre^- control, Cre^- ESD, AGR cKO control, AGR Cko ESD) were dissected in DPBS on P14 and enzymatically dissociated with papain for 45 min at 34°C with 5% CO2 and 95% O2. After digestion, the tissues were mechanically dissociated to obtain a single cell suspension by using a 1 ml pipette, and the cell debris was removed by density gradient centrifugation. According to the manufacturer's instructions, myelin removal beads (Miltenyi Biotec) were used to removed myelin debris and myelin-bound cell aggregates from single cell suspensions, and an anti-ACSA-2 microbead kit (Miltenyi Biotec) was used for astrocyte purification. To isolate total RNA, the astrocyte pellets were suspended in TRIzol (Invitrogen) and stored at -80°C. The total RNA concentration was calculated with a Quant-IT RiboGreen Kit (Invitrogen). To assess the integrity of the total RNA, samples were run on TapeStation RNA ScreenTape (Agilent). Only high-quality RNA with an RIN greater than 7.0 was used for RNA library construction. A library was independently prepared using 1 μg of total RNA from each sample with an Illumina TruSeq Stranded mRNA Sample Prep Kit (Illumina, Inc.). The first step in the workflow involved purifying the poly-A-containing mRNA molecules using poly-T-attached magnetic beads. Following purification, the mRNA was fragmented into small pieces using divalent cations under elevated temperature. The cleaved RNA fragments were transcribed into first strand cDNA using SuperScript II reverse transcriptase (Invitrogen) and random primers. Then, second strand cDNA synthesis was performed using DNA Polymerase I, RNase H and dUTP. The cDNA fragments then underwent an end repair process, the addition of a single 'A' base, and adapter ligation. The products were then purified and enriched by PCR to create the final cDNA library. The libraries were quantified by using KAPA Library Quantification Kits for the Illumina Sequencing platform according to the qPCR Quantification Protocol Guide (KAPA BIOSYSTEMS) and qualified using TapeStation D1000 ScreenTape (Agilent Technologies). The indexed libraries were then subjected to paired-end (2×100 bp) sequencing on the Illumina NovaSeq platform (Illumina, Inc.) by Macrogen Incorporated.

RNA sequencing data analysis

Raw reads were preprocessed to remove low-quality and adapter sequences before analysis, and the processed reads were aligned to Mus musculus (mm10) genome using HISAT v2.1.0.[72] HISAT utilizes two types of indexes for alignment (a global, whole-genome index and tens of thousands of small local indexes). These two types of indexes are constructed using the same BWT (Burrows–Wheeler transform)/graph FM index (GFM) as Bowtie2. Because it uses these efficient data structures and algorithms, HISAT generates aligned reads several times faster than the widely used programs Bowtie and BWA. The reference genome sequence of Mus musculus (mm10) and annotation data were downloaded from NCBI. Then, transcript assembly of known transcripts was performed with StringTie v1.3.4b.[73,74] Based on the results, the abundance of transcripts and genes was calculated as read counts or (fragments per kilobase of exon per million fragments mapped (FPKM) values for each sample. The expression profiles were used to perform additional analyses, such as differentially expressed gene (DEG) analysis. DEGs or differentially abundant transcripts between different groups were filtered through statistical hypothesis testing. RNA sequencing data were uploaded to GEO with accession number GEO: GSE234945.

Differentially expressed genes (DEGs) analysis

The expression profile determined with the HISAT-StringTie pipeline was used to analyze DEGs between comparable samples. In the data preprocessing step, genes with one more than zeroed read count values in the samples were excluded. To facilitate comparison between samples without bias, size factors and gene-wised variation were estimated from the read count data, and the read count data were normalized using the relative log expression (RLE) method using the DESeq2 R library. The statistical significance of the differential expression data was determined using the DESeq2 nbinomWaldTest[75] with a normalized count. The false discovery rate (FDR) was controlled by adjusting the p value using the Benjamini–Hochberg algorithm. For DEGs with a $|\text{fold change}| \geq 2$ and raw $p < 0.05$, hierarchical clustering analysis was performed using the complete linkage method and Euclidean distance as a measure of similarity. Gene enrichment analysis was performed based on biologically and functionally known gene sets, such as Gene Ontology, with gProfiler (https://biit.cs.ut.ee/gprofiler/), which uses a one-sided hypergeometric test.

All data analysis and visualization of DEGs were conducted using R 3.6.1 (www.r-project.org).

Experimental design for c-Fos analysis

The experiment was performed using age-matched 16- to 20-week-old Cre^- control, Cre^- ESD, AGR cKO control, and AGR cKO ESD groups. For habituation, the experimental mouse was placed in the open field chamber (40 × 40 × 40 cm) and allowed to freely explore chamber for 5 min. During the session, an empty wire cage was place in the object group chamber, and a wire cage with an age- and sex-matched C57BL/6 mouse to which the experimental mouse had never been exposed was placed in the social group chamber for 10 min. 1 hour after the session, the mouse was perfused, and fixed for IHC and confocal imaging as described above.

Behavior analysis

Behavioral tests were performed using age-matched 16- to 20-week-old animals.

Tail suspension test (TST)

The mice were individually suspended from a vertical bar with adhesive tape placed 2.0 cm from the tip of the tail for 6 min. The total time spent immobile, defined as the absence of movement to escape, and the latency to the first immobility episode were recorded during the last 5 min of the test.

Forced swim test (FST)

The experiment was performed in a glass cylinder (15 cm high × 13.5 cm diameter) filled with water (23±2°C) to a depth of 12 cm. The mice were allowed to swim for 6 min, and the total time spent immobile, defined as the absence of struggling movements and motionless floating in the water, and the latency to the first immobility episode were recorded during the last 5 min of the test.

Open field test for locomotor activity

The mice were placed in an open field chamber (40 × 40 × 40 cm) and allowed to freely explore the chamber. The animals were recorded with a video camera for 30 min. The movements of the mice, including the total distance traveled and vertical activity (rearing), were analyzed using EthoVision software (Noldus, Wageningen, Netherlands).

Elevated plus maze (EPM) test

The EPM consisted of four arms (30-cm long and 5-cm wide) arranged in the shape of a plus sign and was elevated 70 cm above the floor. Mouse behavior in the EPM was recorded with a video camera for 5 min. The time spent in the open and closed arms and the number of entries made into each arm were automatically analyzed with EthoVision software (Noldus, Wageningen, Netherlands). The degree of anxiety was assessed by calculating the time spent in the open arms.

Sociability and social novelty tests

Sociability and social novelty tests were performed in a partitioned three-chamber apparatus. Each chamber was 20 cm (length) x 40 cm (width) x 22 cm (height). Each side chamber contained a cylindrical wire cage, which was used to house a live mouse. For habituation, the experimental mouse was placed in the center of the empty three-chamber box and allowed to freely explore each chamber for 5 min. In session 1, an age- and sex-matched C57BL/6 mouse (S1) to which the experimental mouse had never been exposed was placed in one of the two wire cages. The wire cage on the other side was kept empty. In session 2, a second age- and sex-matched C57BL/6 stranger mouse (S2, novel) to which the experimental mouse had never been exposed was placed in the wire cage that had been empty in the previous session. In each session, the experimental mouse was placed in the center of the apparatus and allowed to freely explore all chambers for 10 min and was able to choose between the familiar and the stranger mouse. The movement of the mouse was recorded with a video camera and analyzed by EthoVision software (Noldus, Wageningen, Netherlands). The preference index was measured by following equations as previously reported.[76,77]

Session 1 (sociability): (time in novel mouse − time in object)/(time in novel mouse + time in object)

Session 2 (social novelty): (time in novel mouse − time in familiar mouse)/(time in novel mouse + time in familiar mouse)

Novel object recognition (NOR) test

Mice were habituated to an open box (30 × 30 × 35 high cm) for 5 min on the day before the test. During the training session, two objects were placed in the open box, and the animals were allowed to explore the for 10 min. In the test session, the animals were placed into the same box, which contained one of the familiar objects and one novel object. The mice were then allowed to explore freely for 10 min and recorded with a video camera. The time spent exploring each object was automatically calculated with EthoVision software (Noldus, Wageningen, Netherlands). The preference index in the test session and the ratio of the amount of time spent exploring the novel object to the total time spent exploring both objects were analyzed.

In vivo multichannel (extracellular) recording

All recordings were performed using head-fixed and awake mice as previously reported.[78] The left orbitofrontal cortex (OFC) of each mouse was marked, and custom-designed head plates were implanted using dental cement and small screws. After 6-7 days of recovery, awake mice were habituated to head fixation for 20 min before the test day. On the recording day, a small craniotomy was made in previously zmarked left OFC, and 32 channel silicon probes (A1X32-Poly2-10mm-50-177 or A1X32-Poly3-10mm-50-177, Neuronexus) were vertically inserted into the target site using a microdrive manipulator (Siskiyou). After waiting 30 min for the silicon electrode to stabilize at the targeting site, spiking activity was measured during each object-sniffing session in the absence of a stranger mouse ($object_{sniffing}$ session, 10 min) and continuously measured after a head plate-implanted stranger mouse was placed in front of the experimental mouse ($social_{sniffing}$ session, 10 min). During the recording, the sniffing behavior of the mouse was recorded with a camera (G3-GM11-M2020-Genie, Teledyne DALSA) and lens (TEC-M55 2/3" 55-mm telecentric lens, C-Mount) by illuminating the left side of the face of the animal with infrared light (850 nm, S-IR5850, Skycares). Images were recorded at 30 Hz via the Image Acquisition Toolbox provided by MATLAB. All extracellular signals were filtered between 500∼5000 Hz at a sampling rate of 30 kHz and amplified with a miniature digital headstage (CerePlex μ, Blackrock Microsystems) for offline single-unit isolation. To confirm the recording site and for post hoc histological analysis, a silicon electrode was coated with lipophilic dye (1,1′-dioctadecyl-3,3,3′,3′-tetramethylindocarbocyanine perchlorate (DiI), Invitrogen).

Neural activity analysis

The spike-sorting procedure was executed by separating 32 channels on the silicon probe into eight groups (four channels per group) and sorting distinct spike clusters based on three principal components displayed on Klusters software (http://neurosuite.sourceforge.net/). The autocorrelogram of each cluster, which had a 2 msec refractory period, was assessed to rule out the possibility of multiunit contamination. All other analyses were performed using MATLAB (MathWorks). The onset of sniffing behavior during $object_{sniffing}$ and $social_{sniffing}$ sessions was automatically determined using MATLAB. Sniffing trials were considered object-sniffing

trials, which were conducted during the object session, or social-sniffing trials, which were conducted during the social session. To avoid neural activity contamination between sniffing trials, trials that satisfied the following two criteria were used: 1) an intersniffing interval (time between the onset of sniffing in the current trial and the onset of sniffing in the next trial) > 5 sec and 2) a sniffing duration (time between the onset and offset of sniffing in one trial) > 1 sec. To plot the peri-event time histogram (PETH) of activity in example cells (firing rate, Hz) and in populations (Z scored), data from $object_{sniffing}$ and $social_{sniffing}$ trials were collected, the firing rates were averaged, and neural activity was normalized to 1 sec baseline activity (3 to 2 sec before the onset of sniffing). The normalized firing rate was convolved with a Gaussian filter (σ = 50 ms) for visualization purposes and then aligned by comparing the activity (Z) in the 1 sec post-period (0 to 1 sec after the onset of sniffing). Since the total population includes neurons exhibiting the increased or decreased activity induced by either $object_{sniffing}$ or $mouse_{sniffing}$, the sniff-induced activity of the top or bottom 20% of responsive neurons during 0$\sim$2 sec (Z) after the onset of sniffing was selectively quantified to observe the tendency of neuronal responsiveness depending on targets.

Automatic quantification of sniffing behaviors by using VME

Sniffing events during object- and social-sniffing sessions were automatically measured by applying a custom-written MATLAB code as previously reported.[65] First, a region of interest (ROI) including the nose, whiskers and background of the mouse being recorded was selected, and a binary image was made by filling in each pixel with the black and white values according to the threshold (im-binarize, built-in MATLAB function). To measure sniffing movement, the video motion energy (VME) of the mouse nose images was measured using the following equation:

$$\sum_{pixels\ within\ ROI} abs(i_t - i_{t-1})$$

where i_t is the grayscale intensity of the pixel on frame t. The product of the median of the absolute VME and 2.8 was set as the threshold, and sniffing events were included if the VME crossed the threshold.

Illustrations

Illustrations were generated with Biorender (http://www.biorender.com).

QUANTIFICATION AND STATISTICAL ANALYSIS

All statistical analyses were processed using GraphPad Prism 7 software. The statistical tests used are specified in the figure legends. Unpaired *t*-test with 95% confidence was used to compare two samples. One-way ANOVA with Tukey's multiple comparisons test was used for *in vitro* phagocytosis analysis and qPCR data analysis. Two-way ANOVA with Sidak's multiple comparisons test or with Tukey's test was used for multiple samples and behavior tests. To identify outliers, the ROUT method with Q=1% was used for all data.

Immunity, Volume *56*

Supplemental information

Stress induces behavioral abnormalities by increasing expression of phagocytic receptor MERTK in astrocytes to promote synapse phagocytosis

Youkyeong Gloria Byun, Nam-Shik Kim, Gyuri Kim, Yi-Seon Jeon, Jong Bin Choi, Chan-Woo Park, Kyungdeok Kim, Hyunsoo Jang, Jinkyeong Kim, Eunjoon Kim, Yong-Mahn Han, Ki-Jun Yoon, Seung-Hee Lee, and Won-Suk Chung

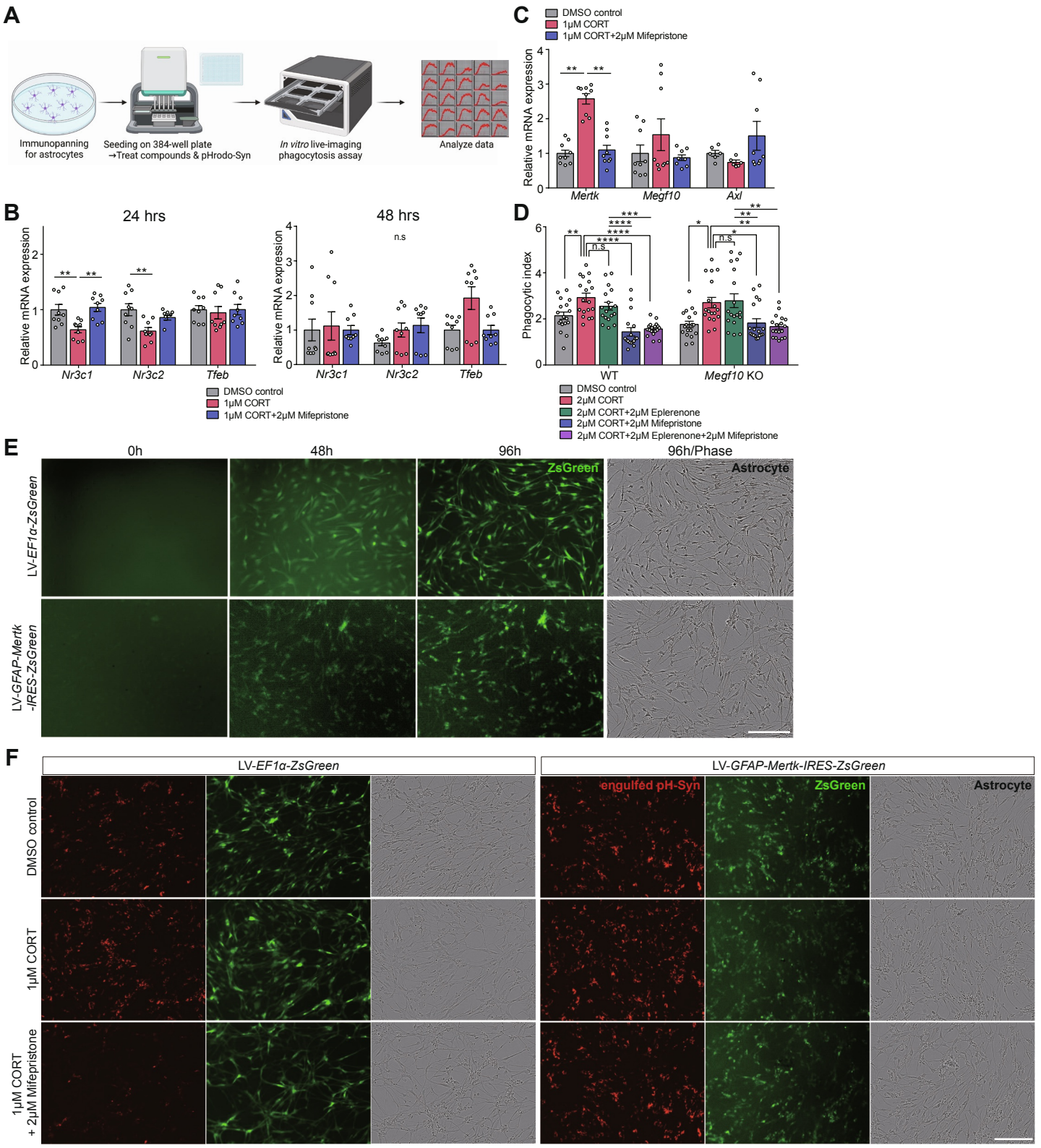
A
Immunopanning for astrocytes
Seeding on 384-well plate →Treat compounds & pHrodo-Syn
In vitro live-imaging phagocytosis assay
Analyze data
B
24 hrs
48 hrs
n.s
Relative mRNA expression
Nr3c1
Nr3c2
Tfeb
DMSO control
1μM CORT
1μM CORT+2μM Mifepristone
C
DMSO control
1μM CORT
1μM CORT+2μM Mifepristone
Relative mRNA expression
Mertk
Megf10
Axl
D
Phagocytic index
WT
Megf10 KO
DMSO control
2μM CORT
2μM CORT+2μM Eplerenone
2μM CORT+2μM Mifepristone
2μM CORT+2μM Eplerenone+2μM Mifepristone
E
0h
48h
96h
96h/Phase
ZsGreen
Astrocyte
LV-EF1α-ZsGreen
LV-GFAP-Mertk -IRES-ZsGreen
F
LV-EF1α-ZsGreen
LV-GFAP-Mertk-IRES-ZsGreen
engulfed pH-Syn
ZsGreen
Astrocyte
DMSO control
1μM CORT
1μM CORT + 2μM Mifepristone

Figure S1. Stress hormones enhance *Mertk*-dependent phagocytosis of astrocytes, related to Figure 1

(**A**) Schematic illustration of compound screening protocol using astrocytes with pHrodo-Syns.

(**B**) Quantitative PCR data showing the mRNAs of CORT-binding receptors (*Nr3c1, Nr3c2*) and a lysosome biogenesis-related gene (*Tfeb*) in cultured rat astrocytes treated with CORT and mifepristone along with pHrodo-Syns for 24 hours and 48 hours.

(**C**) Quantitative PCR data showing the mRNAs of phagocytic receptors (*Mertk, Megf10, Axl*) in cultured rat astrocytes treated with corticosterone (CORT) and mifepristone along with pH-Syns for 24 hours.

(**D**) Bar graphs showing the phagocytic index of WT and *Megf10* KO mouse astrocytes treated with CORT along with mifepristone and/or eplerenone.

(**E**) Representative images of *in vitro* cultured astrocytes (phase) infected with either control or *Mertk* overexpression LV. Both LVs express ZsGreen (green) under the control of the *EF1α* (upper) and *GFAP* (lower) promoters. Scale bar, 200 μm.

(**F**) Representative images showing engulfed pHrodo-Syns (red) by astrocytes (phase) infected with either control or *Mertk* overexpression LV (green). The images were taken at 60 hours after pHrodo-Syns application and pretreatment with CORT with or without mifepristone. Scale bar, 200 μm.

Seven- to ten-day-old male and female littermates were used. (B-D) Representative data from three independent experiments. Six data points were obtained from each independent experiment.

Data shown as mean ± SEM. *P<0.05, **P<0.005, ***P<0.001 ****P<0.0001, ns, non-significant (P>0.05); one-way ANOVA with Tukey's multiple comparisons test.

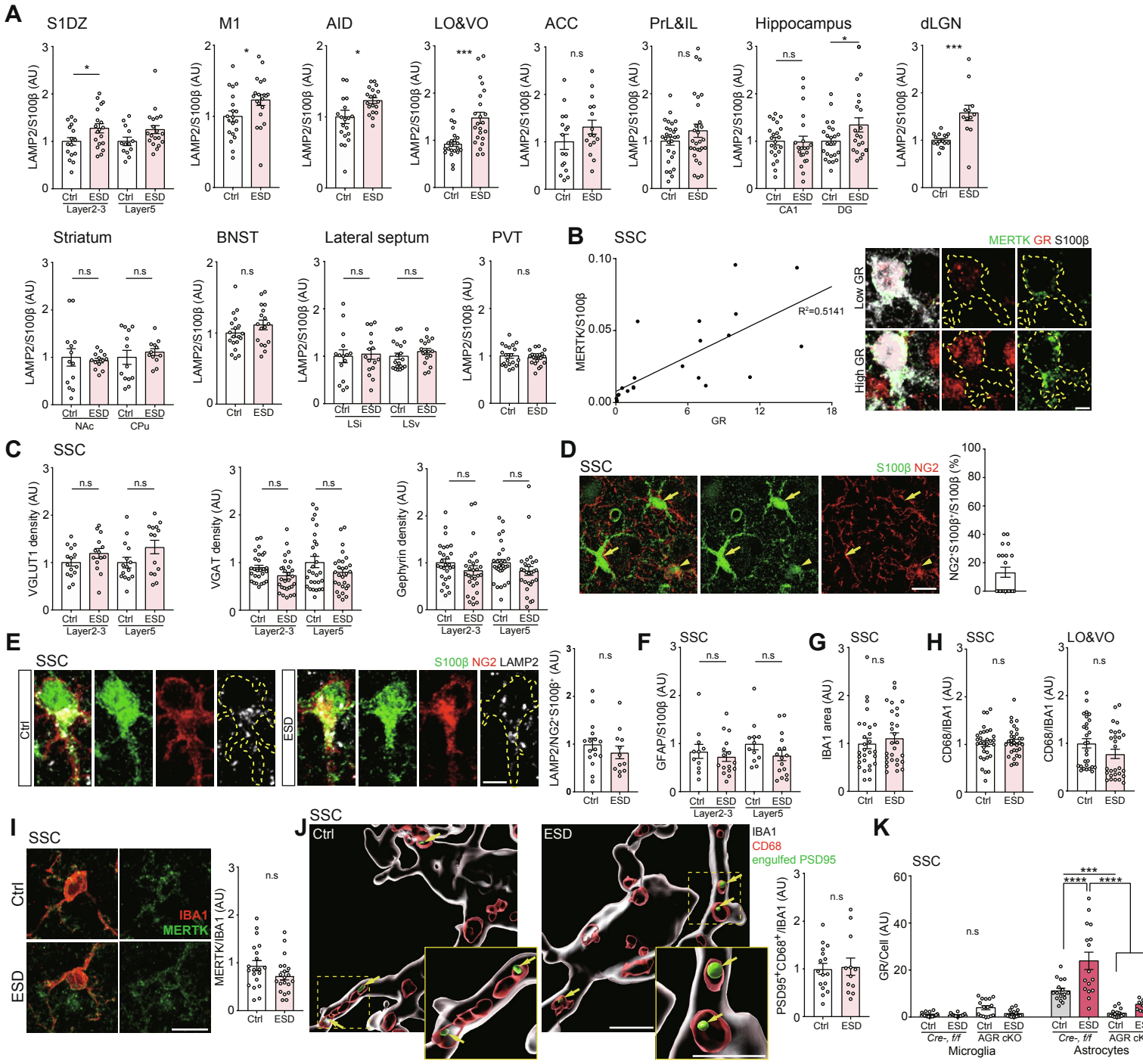
A
S1DZ
M1
AID
LO&VO
ACC
PrL&IL
Hippocampus
dLGN
Striatum
BNST
Lateral septum
PVT
LAMP2/S100β (AU)
Ctrl
ESD
Layer2-3
Layer5
NAc
CPu
LSi
LSv
CA1
DG
n.s
B
SSC
MERTK/S100β
GR
R²=0.5141
MERTK GR S100β
Low GR
High GR
C
SSC
VGLUT1 density (AU)
VGAT density (AU)
Gephyrin density (AU)
D
SSC
S100β NG2
NG2⁺S100β⁺/S100β (%)
E
SSC
S100β NG2 LAMP2
Ctrl
ESD
LAMP2/NG2⁺S100β⁺ (AU)
F
SSC
GFAP/S100β (AU)
G
SSC
IBA1 area (AU)
H
SSC
LO&VO
CD68/IBA1 (AU)
I
SSC
IBA1
MERTK
MERTK/IBA1 (AU)
J
SSC
Ctrl
ESD
IBA1
CD68
engulfed PSD95
PSD95⁺CD68⁺/IBA1 (AU)
K
SSC
GR/Cell (AU)
Cre-, f/f
AGR cKO
Microglia
Astrocytes

Figure S2. ESD enhances astrocyte-mediated phagocytosis in various brain regions, related to Figure 2

(**A**) Bar graphs showing that the amount of lysosomes in astrocytes from the S1DZ layer2-3, M1, AID, LO&VO, and dLGN of mice exposed to ESD was increased. Note that the amount of astrocytic lysosomes was not changed in the S1DZ layer5, ACC, PrL&IL, hippocampus (CA1), striatum (NAc and CPu), BNST, lateral septum (LSi and LSv) or PVT after ESD (n=3-5 for each group).

(**B**) Dot plots and representative confocal z-stack images showing correlation between MERTK (green) expression and GR (red) activation from individual astrocytes (S100β, white) in the ESD SSC. The linear regression shows positive correlation between MERTK and GR (total 26 astrocytes). The yellow dotted lines outline astrocytes. Scale bar, 5 μm.

(**C**) Bar graphs showing that the numbers of VGLUT1$^+$ excitatory pre-synapses, VGAT$^+$ inhibitory pre-synapses, and Gephyrin$^+$ inhibitory post-synapses were unchanged in layers 2-3 and 5 of the SSC after ESD (n=5-7 for each group).

(**D**) Representative confocal z-stack images showing astrocytes (S100β$^+$ only, green, yellow arrows) and OPCs (S100β$^+$ and NG2$^+$, green and red, yellow arrowhead). Bar graph showing that S100β$^+$NG2$^+$ OPCs were 12.7% among S100β$^+$ cells (n=5). Note that S100β$^+$NG2$^+$ OPCs express S100β lower than those of astrocytes. Scale bar, 15 μm.

(**E**) Representative confocal z-stack images of lysosomes (LAMP2, white) in S100β$^+$NG2$^+$ OPCs (S100β and NG2, green and red) in the control and ESD SSC. The yellow dotted lines outline OPCs. Bar graphs showing that the amount of lysosomes was unchanged in S100β$^+$NG2$^+$ OPCs in ESD model mice (n=4 and 3). Scale bar, 5 μm.

(**F**-**G**) Bar graph showing that the GFAP$^+$ (F), IBA1$^+$ (G) areas were unchanged in the SSC in mice exposed to ESD (n=3-4 for each group).

(**H**) Bar graph showing that the CD68$^+$ lysosomal areas in the SSC and LO&VO were unchanged in mice exposed to ESD (n=7 and 7).

(**I**) Representative confocal z-stack images showing MERTK (green) expression in microglia (IBA1, red) in the SSC of control and ESC mice. Bar graph showing microglial MERTK expression was unchanged after ESD (n=3 and 3). Scale bar, 10 μm.

(**J**) Representative 3D reconstructed images showing engulfed PSD95 (green, yellow arrow) inside microglial (IBA1, white) lysosomes (CD68, red). The yellow boxes indicate the magnified 3D reconstructed areas. Bar graphs showing that the amount of engulfed PSD95$^+$ puncta inside lysosomes was unchanged in microglia from the ESD SSC (n=4 and 3). Scale bar, 4 μm.

(**K**) Bar graphs showing that the GR activation were much lower in microglia than those of astrocytes. Note that microglial GR activation was unchanged by either ESD condition or GR depletion in astrocytes (n= 4 for each group).

(A, F-I, K) Fourteen- and (C) thirty-day-old male littermates were used. (B, D-E, J) Fourteen-day-old male and female littermates were used. n values represent the number of mice per each group. Four data points were obtained from each mouse, and outliers were removed.

Data shown as mean ± SEM. *P<0.05, ***P<0.001, ****P<0.0001, ns, non-significant (P>0.05); unpaired *t*-test (A, E, G-J), Two-way ANOVA with Sidak's multiple comparisons test (A, C, F), and Two-way ANOVA with Tukey's multiple comparisons test (K).

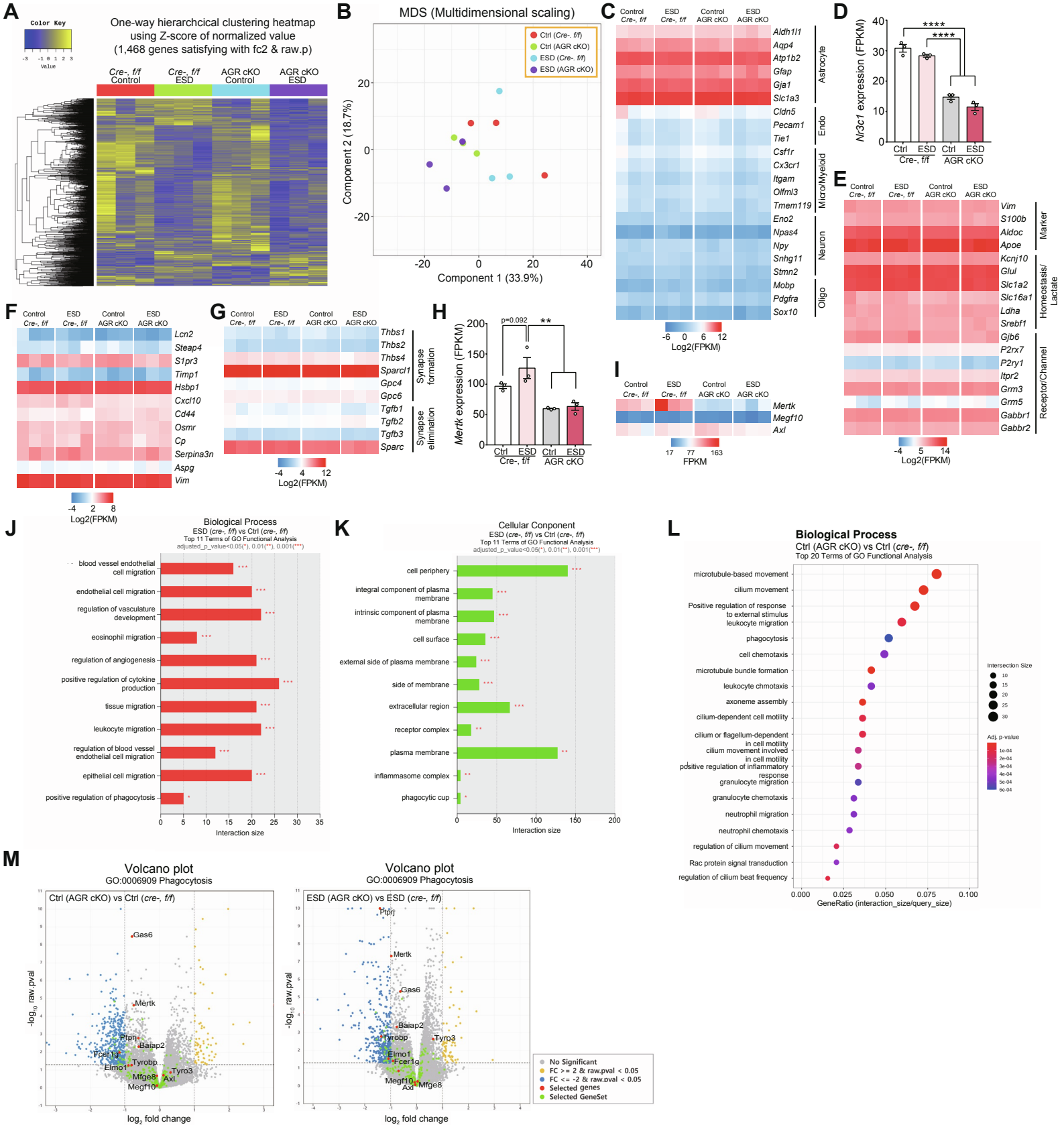
A
Color Key
Value
One-way hierarchcical clustering heatmap
using Z-score of normalized value
(1,468 genes satisfying with fc2 & raw.p)
Cre-, f/f Control
Cre-, f/f ESD
AGR cKO Control
AGR cKO ESD
B
MDS (Multidimensional scaling)
Ctrl (Cre-, f/f)
Ctrl (AGR cKO)
ESD (Cre-, f/f)
ESD (AGR cKO)
Component 1 (33.9%)
Component 2 (18.7%)
C
Aldh1l1
Aqp4
Atp1b2
Gfap
Gja1
Slc1a3
Cldn5
Pecam1
Tie1
Csf1r
Cx3cr1
Itgam
Olfml3
Tmem119
Eno2
Npas4
Npy
Snhg11
Stmn2
Mobp
Pdgfra
Sox10
Astrocyte
Endo
Micro/Myeloid
Neuron
Oligo
Log2(FPKM)
D
Nr3c1 expression (FPKM)
****
****
Ctrl
ESD
Ctrl
ESD
Cre-, f/f
AGR cKO
E
Vim
S100b
Aldoc
Apoe
Kcnj10
Glul
Slc1a2
Slc16a1
Ldha
Srebf1
Gjb6
P2rx7
P2ry1
Itpr2
Grm3
Grm5
Gabbr1
Gabbr2
Marker
Homeostasis/ Lactate
Receptor/Channel
Log2(FPKM)
F
Lcn2
Steap4
S1pr3
Timp1
Hsbp1
Cxcl10
Cd44
Osmr
Cp
Serpina3n
Aspg
Vim
Log2(FPKM)
G
Thbs1
Thbs2
Thbs4
Sparcl1
Gpc4
Gpc6
Tgfb1
Tgfb2
Tgfb3
Sparc
Synapse formation
Synapse elimination
Log2(FPKM)
H
Mertk expression (FPKM)
p=0.092
**
Ctrl
ESD
Ctrl
ESD
Cre-, f/f
AGR cKO
I
Mertk
Megf10
Axl
FPKM
J
Biological Process
ESD (cre-, f/f) vs Ctrl (cre-, f/f)
Top 11 Terms of GO Functional Analysis
adjusted_p_value<0.05(*), 0.01(**), 0.001(***)
blood vessel endothelial cell migration
endothelial cell migration
regulation of vasculature development
eosinophil migration
regulation of angiogenesis
positive regulation of cytokine production
tissue migration
leukocyte migration
regulation of blood vessel endothelial cell migration
epithelial cell migration
positive regulation of phagocytosis
Interaction size
K
Cellular Conponent
ESD (cre-, f/f) vs Ctrl (cre-, f/f)
Top 11 Terms of GO Functional Analysis
adjusted_p_value<0.05(*), 0.01(**), 0.001(***)
cell periphery
integral component of plasma membrane
intrinsic component of plasma membrane
cell surface
external side of plasma membrane
side of membrane
extracellular region
receptor complex
plasma membrane
inflammasome complex
phagocytic cup
Interaction size
L
Biological Process
Ctrl (AGR cKO) vs Ctrl (cre-, f/f)
Top 20 Terms of GO Functional Analysis
microtubule-based movement
cilium movement
Positive regulation of response to external stimulus
leukocyte migration
phagocytosis
cell chemotaxis
microtubule bundle formation
leukocyte chmotaxis
axoneme assembly
cilium-dependent cell motility
cilium or flagellum-dependent in cell motility
cilium movement involved in cell motility
positive regulation of inflammatory response
granulocyte migration
granulocyte chemotaxis
neutrophil migration
neutrophil chemotaxis
regulation of cilium movement
Rac protein signal transduction
regulation of cilium beat frequency
GeneRatio (interaction_size/query_size)
Intersection Size
Adj. p-value
M
Volcano plot
GO:0006909 Phagocytosis
Ctrl (AGR cKO) vs Ctrl (cre-, f/f)
ESD (AGR cKO) vs ESD (cre-, f/f)
-log10 raw.pval
log2 fold change
Gas6
Mertk
Ptprj
Baiap2
Fcer1g
Tyrobp
Elmo1
Mfge8
Tyro3
Axl
Megf10
No Significant
FC >= 2 & raw.pval < 0.05
FC <= -2 & raw.pval < 0.05
Selected genes
Selected GeneSet

Figure S3. GR regulates the expression of *Mertk* and phagocytosis-related genes in astrocytes, related to Figure 4

(**A**) Heatmaps showing one-way hierarchical clustering of astrocytic gene expression in the four groups (Cre$^-$ Control, Cre$^-$ ESD, AGR cKO Control, AGR cKO ESD).

(**B**) Dot plots showing multidimensional scaling of variability in astrocytes in the four groups.

(**C**) Heatmaps showing the mRNA expression of cell type-specific marker genes. Note that our samples were highly enriched in astrocyte-specific genes.

(**D**) Bar graphs showing astrocytic *Nr3c1* mRNA expression in the four groups. Note that the *Nr3c1* mRNA expression was much reduced in astrocytes from AGR cKO (Control and ESD) mice compared to Cre$^-$ (Control and ESD) mice (n=3 for each group).

(**E-G**) Heatmaps showing the expression of general astrocyte property-related genes (E: astrocytic, homeostatic/lactate, and receptor/channel markers), PAN astrocyte reactive genes (F), and genes related to astrocyte-mediated synapse formation and non-phagocytic elimination (G). The expression of these astrocyte-specific genes was not changed by ESD and/or GR deletion.

(**H**) Bar graphs showing the expression of phagocytic receptor genes in astrocytes. Note that among phagocytic receptor genes, only *Mertk* expression was increased in Cre$^-$ ESD mice compared to Cre$^-$ control mice and was conversely decreased in both AGR cKO control and ESD mice.

(**I**) Heatmaps showing that *Mertk* mRNA expression in astrocytes in the four groups. Note that the *Mertk* mRNA expression was increased in astrocytes from Cre$^-$ ESD mice compared to astrocytes from Cre- control mice. Conversely, the *Mertk* mRNA expression was decreased in astrocytes from AGR cKO control and ESD mice compared to Cre$^-$ ESD mice (n=3 for each group).

(**J**) Bar graphs showing the term-size filtered top 11 enriched biological process GO terms in astrocytes from Cre$^-$ ESD mice compared to astrocytes from Cre$^-$ control mice. Note that the expression of phagocytosis-related genes was upregulation in astrocytes from Cre$^-$ ESD mice.

(**K**) Bar graphs showing the size filtered top 11 enriched cellular component GO terms in astrocytes from Cre$^-$ ESD mice compared to astrocytes from Cre$^-$ control mice. Note that the expression of phagocytic cup-related genes was increased in astrocytes from Cre$^-$ ESD mice.

(**L**) A dot graph showing the term-size filtered top 20 enriched biological process GO terms in astrocytes from Cre$^+$ control mice compared to Cre$^-$ control mice.

(**M**) Volcano plots showing gene expression changes (blue: decreased and yellow: increased) in Cre$^+$ control compared to Cre$^-$ control mice (left, decreased: 428 genes, increased: 71 genes), and ESD control compared to ESD Cre$^-$ mice (right, decreased: 474 genes, increased: 69 genes). Green dots indicate selected GO term genes (GO:0006909, Phagocytosis) and red dots represent selected genes including astrocyte phagocytosis related genes such as *Mertk, Megf10, Axl, Gas6, Mfge8, Baiap2, Ptprj, Elmo1, Fcer1g* and *Tyrobp*. Note that *Nr3c1* depletion in astrocytes down-regulated *Mertk* and *Gas6* as well as astrocytic phagocytosis related genes without changing other phagocytic receptors, including *Megf10*, *Axl* and *Tyro3*.

Fourteen-day-old male littermates were used. (J-L) Interaction size indicate the number of unique DEGs corresponding to individual GO term. n values represent the number of mice per each group.
Data shown as mean ± SEM. **P<0.005, ****P<0.0001; Two-way ANOVA with Tukey's multiple comparisons test.

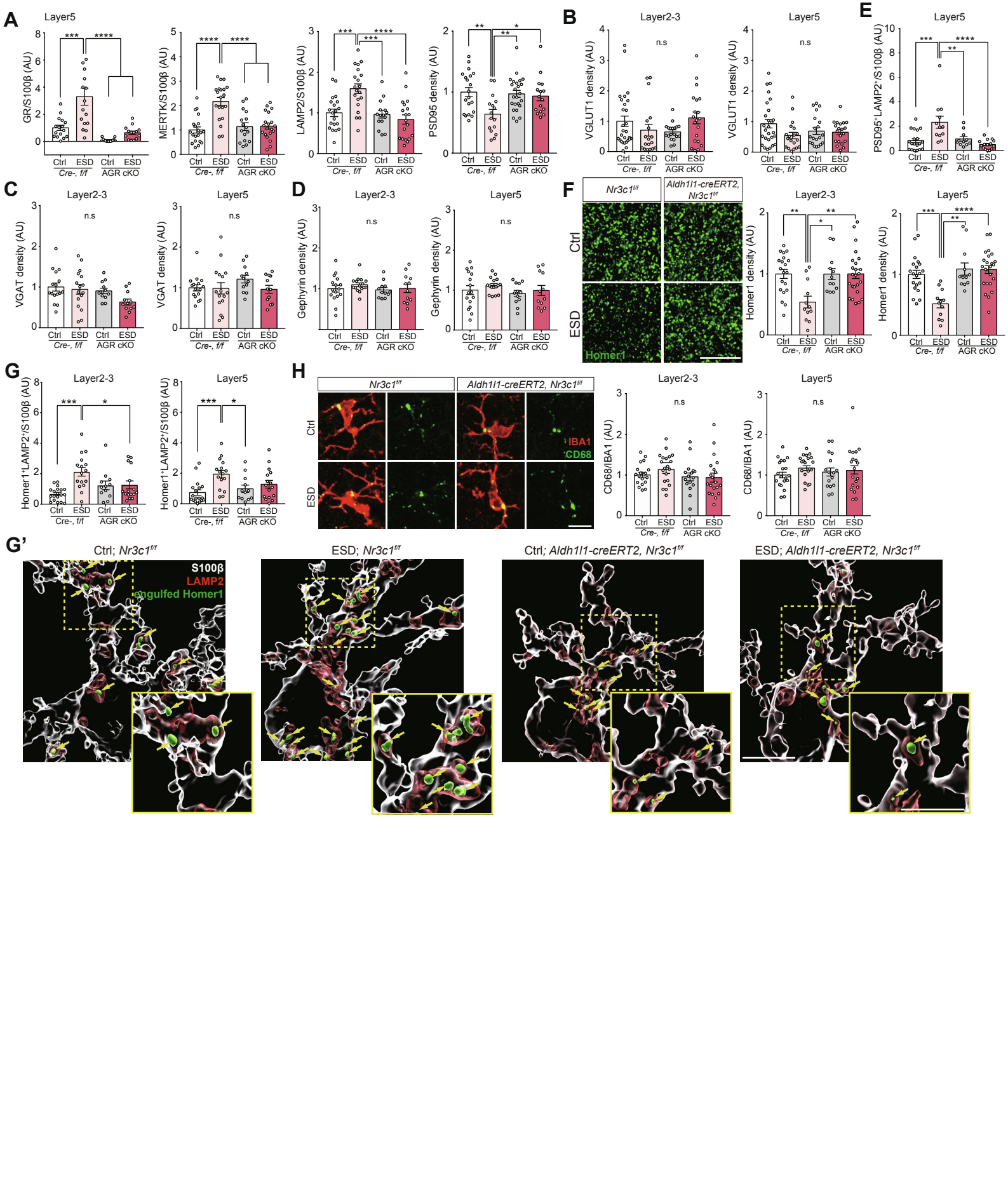
A
Layer5
GR/S100β (AU)
MERTK/S100β (AU)
LAMP2/S100β (AU)
PSD95 density (AU)
Ctrl
ESD
Cre-, f/f
AGR cKO
B
Layer2-3
Layer5
VGLUT1 density (AU)
n.s
E
PSD95+LAMP2+/S100β (AU)
C
VGAT density (AU)
D
Gephyrin density (AU)
F
Nr3c1f/f
Aldh1l1-creERT2, Nr3c1f/f
Ctrl
ESD
Homer1
Homer1 density (AU)
G
Homer1+LAMP2+/S100β (AU)
H
IBA1
CD68
CD68/IBA1 (AU)
G'
Ctrl; Nr3c1f/f
ESD; Nr3c1f/f
Ctrl; Aldh1l1-creERT2, Nr3c1f/f
ESD; Aldh1l1-creERT2, Nr3c1f/f
S100β
LAMP2
engulfed Homer1

Figure S4. Astrocyte-specific GR ablation attenuates changes in astrocytic GR-MERTK expression and the synaptic density in layer 2-3 and 5 of SSC after ESD, related to Figure 4

(**A**) Bar graphs showing changes in astrocytic GR activation, MERTK expression, and lysosomal numbers as well as PSD95$^+$ synaptic density in layer 5 of the SSC from the four groups (Cre$^-$ control, Cre$^-$ ESD, AGR cKO control, AGR cKO ESD) (n=4-7 for each group). Note that the same pattern of changes was observed in layer 5 and layer 2-3 of the SSC.
(**B**-**D**) Bar graphs showing the VGLUT1$^+$ excitatory pre-synapse (B), VGAT$^+$ inhibitory pre-synapse (C), and Gephyrin$^+$ inhibitory post-synapse (D) density in layer 2-3 and layer 5 of the SSC (n=4-7 for each group). Note that the numbers of these synapses were not changed by ESD and/or GR deletion.
(**E**) Bar graphs showing that the amount of phagocytosed PSD95$^+$ synaptic puncta inside lysosomes was increased in astrocytes from Cre$^-$ ESD mice but not in astrocytes from AGR cKO ESD mice (n=4, 3, 3 and 4).
(F) Representative confocal z-stack images and bar graphs showing Homer1$^+$ excitatory post-synapse density in layer 2-3 and layer 5 of the SSC from the four groups (n=5, 4, 3 and 5)
(**G**) Bar graphs showing that the amount of phagocytosed Homer1$^+$ synaptic puncta inside lysosomes was increased in astrocytes from Cre$^-$ ESD mice but not in astrocytes from AGR cKO ESD mice (n=5, 4, 3 and 5).
(**G'**) Representative confocal 3D reconstructed images showing the amount of phagocytosed Homer1$^+$ puncta (green, yellow arrows) inside lysosomes (LAMP2, red) in astrocytes (S100β, white) from layer 2-3 of the SSC. The yellow boxes indicate the magnified 3D reconstructed areas. Scale bar, 5 μm.
(**H**) Representative confocal z-stack images showing lysosomes (CD68, green) in microglia (IBA1, red) from the SSC of the four groups. Bar graphs showing that the amount of CD68$^+$ lysosomes in microglia was unchanged in the ESD SSC of Cre$^-$ and AGR cKO mice (n=5, 5, 4 and 5). Scale bar, 10 μm.
(A, E, H) Fourteen- and (B-D) thirty-day-old male littermates were used. (G, G') Fourteen- and (F) thirty-day-old male and female littermates were used. (A-H) n values represent the number of mice per each group. Four data points were obtained from each mouse, and outliers were removed.
Data shown as mean ± SEM. *P<0.05, **P<0.005, ***P<0.001, ****P<0.0001, ns, non-significant (P>0.05); Two-way ANOVA with Tukey's multiple comparisons test.

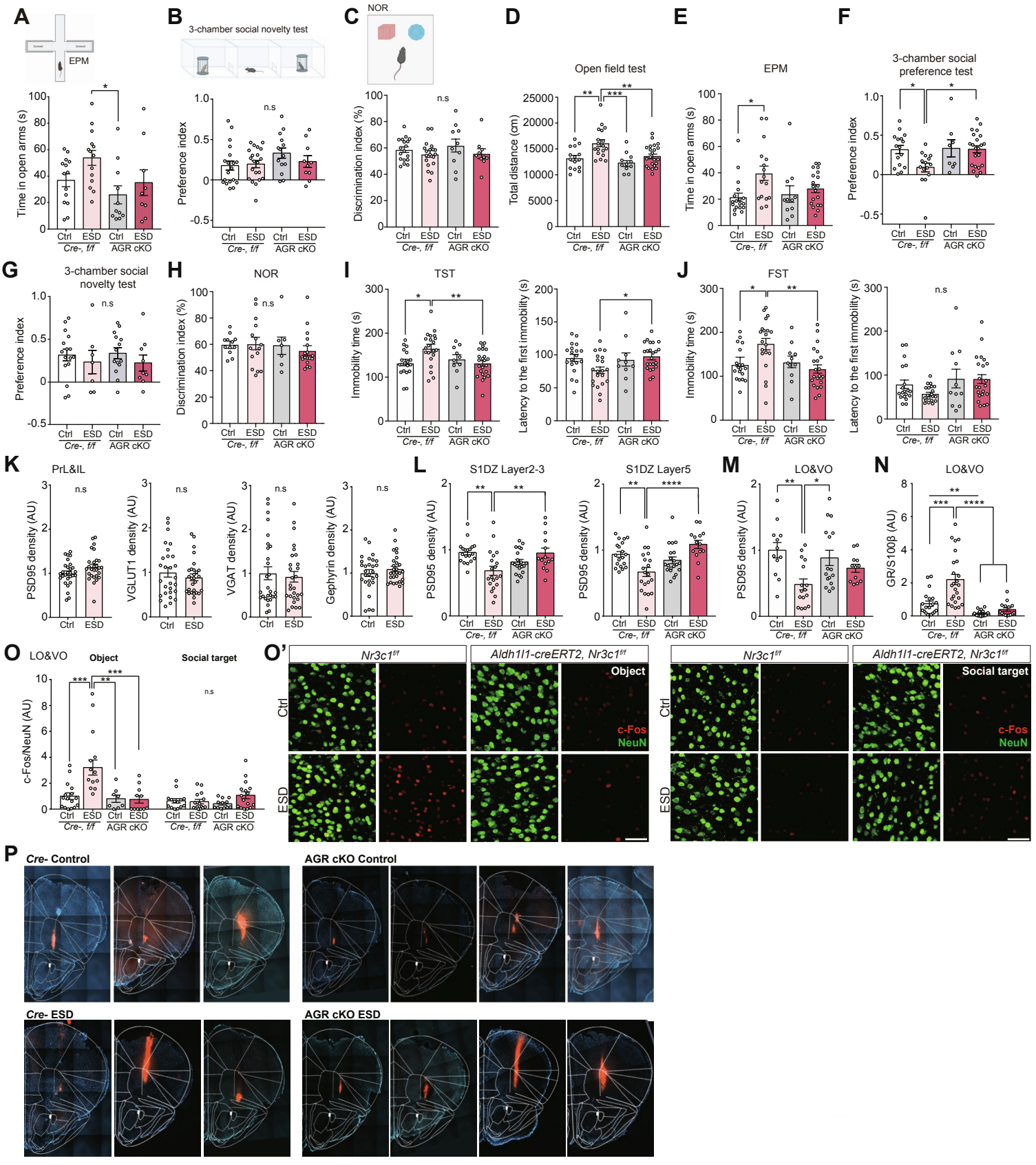
A
EPM
Time in open arms (s)
B
3-chamber social novelty test
Preference index
n.s
C
NOR
Discrimination index (%)
n.s
D
Open field test
Total distance (cm)
E
EPM
Time in open arms (s)
F
3-chamber social preference test
Preference index
G
3-chamber social novelty test
Preference index
n.s
H
NOR
Discrimination index (%)
n.s
I
TST
Immobility time (s)
Latency to the first immobility (s)
J
FST
Immobility time (s)
Latency to the first immobility (s)
n.s
K
PrL&IL
PSD95 density (AU)
VGLUT1 density (AU)
VGAT density (AU)
Gephyrin density (AU)
n.s
L
S1DZ Layer2-3
S1DZ Layer5
PSD95 density (AU)
M
LO&VO
PSD95 density (AU)
N
LO&VO
GR/S100β (AU)
O
LO&VO
Object
Social target
c-Fos/NeuN (AU)
n.s
O'
Nr3c1f/f
Aldh1l1-creERT2, Nr3c1f/f
Ctrl
ESD
Object
Social target
c-Fos
NeuN
P
Cre- Control
AGR cKO Control
Cre- ESD
AGR cKO ESD
Ctrl ESD Ctrl ESD
Cre-, f/f
AGR cKO

Figure S5. Astrocyte-specific GR ablation reduces abnormal behaviors and neuronal activity after ESD, related to Figure 5

(**A**) Schematic illustration and bar graphs showing the results of the EPM test (n = 14 Cre^- control mice, n=14 Cre^- ESD mice, n=11 AGR cKO control mice and n=9 AGR cKO ESD mice).

(B) Schematic illustration and bar graph showing the results of the three-chamber social novelty test. Normal social novelty preference was observed in all the groups (n = 19 Cre^- control mice, n=21 Cre^- ESD mice, n=14 AGR cKO control mice and n=10 AGR cKO ESD mice).

(**C**) Schematic illustration and bar graph showing the results of the NOR test. No defects were observed in any group (n = 18 Cre^- control mice, n=19 Cre^- ESD mice, n=10 AGR cKO control mice and n=10 AGR cKO ESD mice).

(**D-J**) Bar graph showing the behavior test results for female AGR cKO mice exposed to ESD or not. Basal locomotor activity measured by the open field test (D); basal anxiety measured by the EPM test (E); sociability (F) and social novelty preference (G) measured by the three-chamber social preference test, NOR test (H); and depressive behaviors measured by the TST (I: mean duration of immobility (left) and mean latency to the first immobility episode (right)) and FST (J: mean duration of immobility (left) and mean latency to the first immobility episode (right)). Note that all behavioral symptoms observed in Cre^- ESD mice were substantially normalized in AGR cKO ESD mice (D-J) n=15 (D), 18 (E), 16 (F, G), 12 (H), 19 (I), 19 (J) for Cre^- control mice; n=18 (D), 11 (E), 15 (F, G), 15 (H), 21 (I), 20 (J) for Cre^- ESD mice; n=12 (D), 16 (E), 8 (F, G), 7 (H), 10 (I), 11 (J) AGR cKO control mice; n=21 (D), 19 (E), 22 (F, G), 18 (H), 23 (I), 22 (J) AGR cKO ESD mice.

(K) Bar graphs showing that the numbers of $PSD95^+$ excitatory post-synapses, $VGLUT1^+$ excitatory pre-synapses, $VGAT^+$ inhibitory pre-synapses, and $Gephyrin^+$ inhibitory post-synapses were unchanged in PrL&IL after ESD (n=7 and 7).

(L) Bar graphs showing the $PSD95^+$ excitatory post-synapse and $VGLUT1^+$ excitatory pre-synapse density in layer2-3 and layer 5 of the S1DZ (n=4 for each group).

(**M-N**) Bar graphs showing changes in the $PSD95^+$ synaptic density (M) and GR activation (N) in the LO&VO in AGR cKO ESD mice. Note that the same pattern of changes was observed in the LO&VO and the SSC (n=3-5 for each group).

(**O-O'**) Bar graphs (O) and representative confocal z-stack images (O') of c-Fos (red) in neurons (NeuN, green) in the LO&VO. Note that after exposing to object, Cre^- ESD mice showed highly increased c-Fos expression in LO&VO neurons, which was largely prevented in AGR cKO ESD mice (n=2-4 for each group).

(**P**) Histological images showing the placement of the multi-electrode in the LO&VO. Note that the targeted regions were visualized with lipophilic dye (red) and DAPI (blue) in the four groups (Cre^- Control, Cre^- ESD, AGR cKO Control, AGR cKO ESD).

(A-C, O-P) Sixteen- to eighteen-week-old male littermates were used. (D-J) Sixteen- to eighteen-week-old female littermates were used. (N) Fourteen- and (K-M) thirty-day-old male littermates were used. (K-O) n values represent the number of mice per each group. Four data points were obtained from each mouse, and outliers were removed.

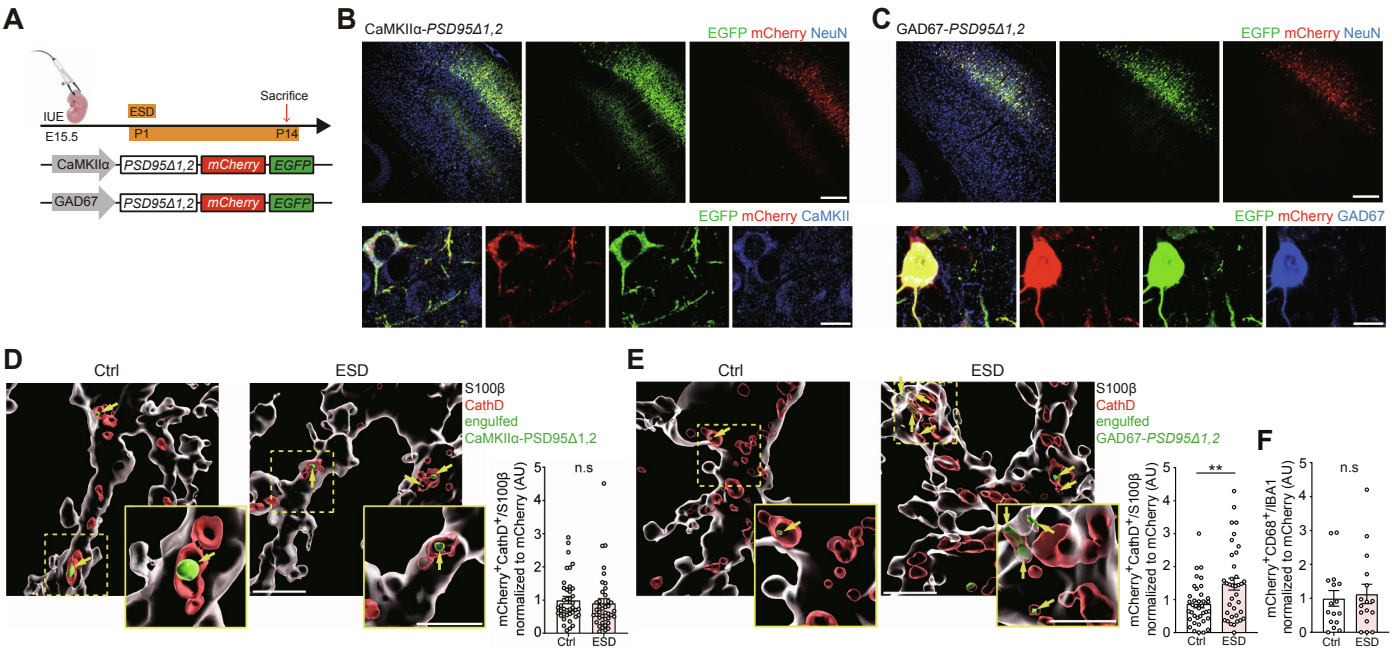

Figure S6. Stress hormones preferentially induce astrocytic elimination of excitatory synapses on GABAergic neurons, related to Figures 5 and 7

(**A**) Schematic illustration of the IUE and ESD experiments using the synapse elimination reporters.

(**B**) Representative confocal single-plane (upper) and z-stack (lower) images showing layer 2-3 of the SSC labeled with CaMKIIα -PSD95Δ1,2-mCherry-EGFP (red and green) costaining with NeuN (blue, upper) and CaMKII (blue, lower) in P14 mice after IUE. Scale bar, 10 μm (lower), 200 μm (upper).

(**C**) Representative confocal single-plane (upper) and z-stack (lower) images showing layer 2-3 of the SSC labeled with GAD67-PSD95Δ1,2-mCherry-EGFP (red and green) costaining with NeuN (blue, upper) and GAD67 (blue, lower) in P14 mice after IUE. Scale bar, 10 μm (lower), 200 μm (upper).

(**D-E**) Representative 3D reconstructed images and bar graphs showing the amount of mCherry-alone puncta (green, yellow arrows) derived from excitatory post-synapses on either CaMKIIα$^+$ (D) or GAD67$^+$ (E) neurons. mCherry-alone puncta are co-localized with lysosomes (CathD, red) in astrocytes (S100β, white) from layer 2-3 of the SSC in control and ESD mice (n=8-10 for each group). The yellow boxes indicate the magnified 3D reconstructed areas. Scale bar, 5 μm.

(**F**) Bar graphs showing that the amount of mCherry-alone puncta in microglial lysosomes, which were derived from excitatory post-synapses on GAD67$^+$ neurons was unchanged in ESD model mice (n=4 and 4).

Fourteen-day-old male and female littermates were used. (D-F) n values represent the number of mice per each group. Four data points were obtained from each mouse, and outliers were removed.

Data shown as mean ± SEM. **P<0.005, ns, non-significant (P>0.05); unpaired *t*-test.

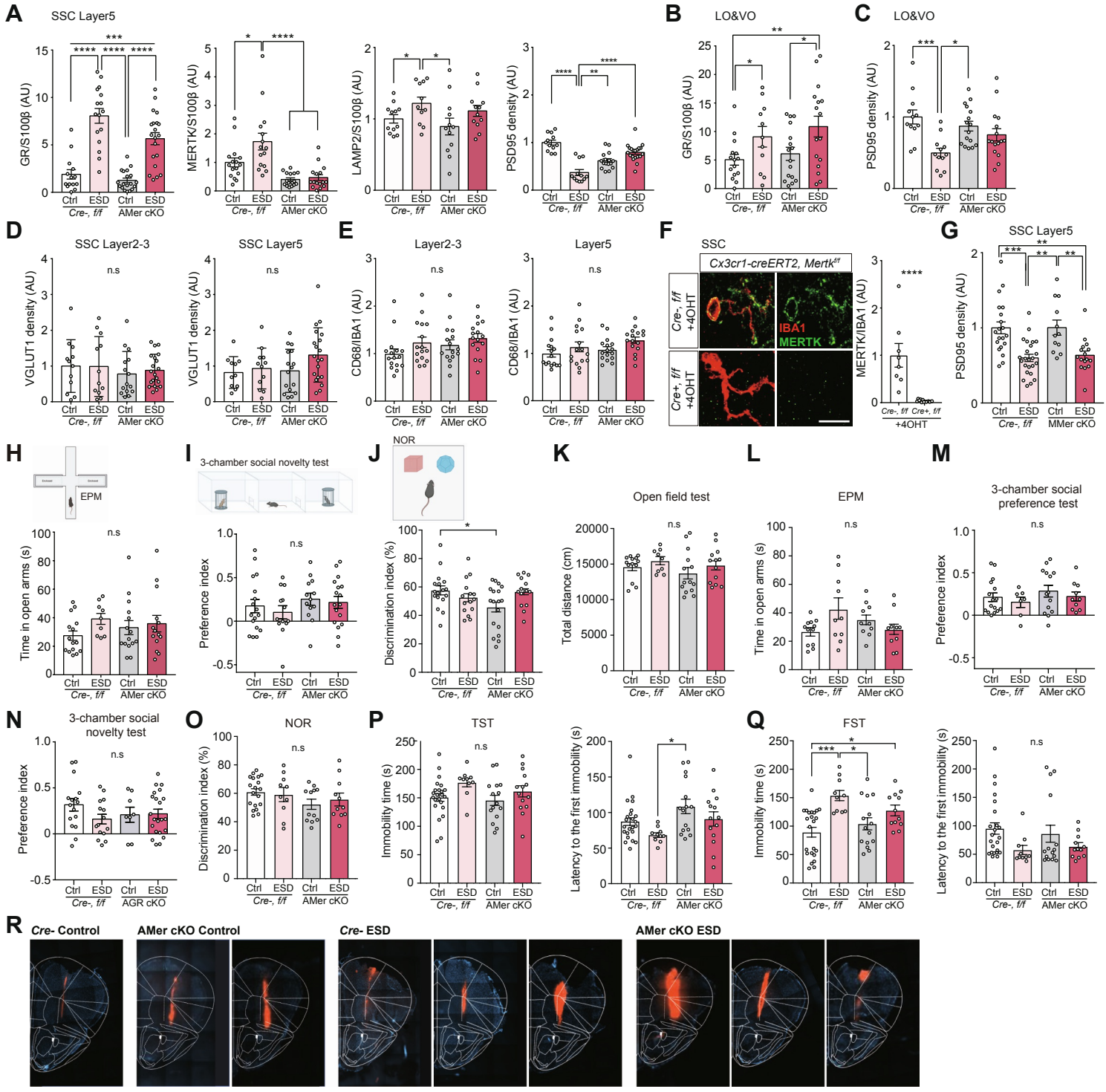
A
SSC Layer5
GR/S100β (AU)
MERTK/S100β (AU)
LAMP2/S100β (AU)
PSD95 density (AU)
B
LO&VO
GR/S100β (AU)
C
LO&VO
PSD95 density (AU)
Ctrl
ESD
Cre-, f/f
AMer cKO
D
SSC Layer2-3
SSC Layer5
VGLUT1 density (AU)
n.s
E
Layer2-3
Layer5
CD68/IBA1 (AU)
F
SSC
Cx3cr1-creERT2, Mertk f/f
Cre-, f/f +4OHT
Cre+, f/f +4OHT
IBA1
MERTK
MERTK/IBA1 (AU)
+4OHT
G
SSC Layer5
PSD95 density (AU)
MMer cKO
H
EPM
Time in open arms (s)
I
3-chamber social novelty test
Preference index
J
NOR
Discrimination index (%)
K
Open field test
Total distance (cm)
L
EPM
Time in open arms (s)
M
3-chamber social preference test
Preference index
N
3-chamber social novelty test
Preference index
AGR cKO
O
NOR
Discrimination index (%)
P
TST
Immobility time (s)
Latency to the first immobility (s)
Q
FST
Immobility time (s)
Latency to the first immobility (s)
R
Cre- Control
AMer cKO Control
Cre- ESD
AMer cKO ESD

Figure S7. Astrocyte-specific MERTK ablation normalizes changes in astrocytic phagocytosis and behaviors after ESD, related to Figures 6 and 7

(**A**) Bar graphs showing changes in astrocytic GR activation, MERTK expression, and the lysosomal numbers as well as PSD95$^+$ synaptic density in layer 5 of the SSC from the four groups (Cre$^-$ control, Cre$^-$ ESD, AMer cKO control, AMer cKO ESD) (n=3-5 for each group). Note that the same pattern of changes was observed in layer 5 of the SSC and layer 2-3 of the SSC.

(**B-C**) Bar graphs showing changes in GR activation (B) and the PSD95$^+$ synaptic density (C) in the LO&VO of the four groups. Note that the same pattern of changes was observed in the LO&VO and the SSC (n=3-5 for each group).

(**D**) Bar graphs showing that the VGLUT1$^+$ excitatory pre-synapse density in layer 2-3 and layer 5 of the SSC was not changed by ESD and/or *Mertk* deletion (n=3, 3, 4 and 4).

(**E**) Bar graphs showing that the amount of CD68$^+$ lysosomes in microglia was unchanged in the ESD SSC of Cre$^-$ and AMer cKO mice (n=3 for each group).

(**F**) Representative confocal z-stack images showing MERTK (green) in microglia (IBA1, red). Bar graph showing that MERTK was effectively ablated in microglia from 4-OHT injected MMer cKO mice (n=2 and 4). Scale bar, 10 μm.

(**G**) Bar graphs showing that the PSD95$^+$ synaptic density was decreased in layer 5 of the SSC in both Cre$^-$ mice and MMer cKO mice after ESD (n=5, 6, 3 and 4).

(**H**) Schematic illustration and bar graph showing the results of the EPM test (n = 15 Cre$^-$ control mice, n=9 Cre$^-$ ESD mice, n=15 AMer cKO control mice and n=14 AMer cKO ESD mice).

(**I**) Schematic illustration and bar graph showing the results of the three-chamber social novelty test. Normal social novelty preference was observed in all the groups (n = 17 Cre$^-$ control mice, n=12 Cre$^-$ ESD mice, n=13 AMer cKO control mice and n=16 AMer cKO ESD mice).

(**J**) Schematic illustration and bar graph showing the results of the NOR test. No defects were observed in any group (n = 17 Cre$^-$ control mice, n=15 Cre$^-$ ESD mice, n=18 AMer cKO control mice and n=14 AMer cKO ESD mice).

(**K-Q**) Bar graph showing the behavior test results for female AMer cKO mice exposed to ESD or not. Basal locomotor activity measured by the open field test (K); basal anxiety measured by the EPM test (L); sociability (M) and social novelty preference (N) measured by the three-chamber social preference test, NOR test (O); and depressive behaviors measured by the TST (P: mean duration of immobility (left) and mean latency to the first immobility episode (right)) and FST (Q: mean duration of immobility (left) and mean latency to the first immobility episode (right)). Note that all behavioral symptoms observed in Cre$^-$ ESD mice were substantially normalized in AMer cKO ESD mice. n=13 (K), 12 (L), 16 (M, N), 19 (O), 23 (P), 23 (Q) for Cre$^-$ control mice; n= 9 (K), 10 (L), 7 (M, N), 10 (O), 10 (P), 10 (Q) for Cre$^-$ ESD mice; n=14 (K), 10 (L), 14 (M, N), 12 (O), 15 (P), 15 (Q) for AMer cKO control mice; n=13 (K), 10 (L), 9 (M, N), 11 (O), 14 (P), 12 (Q) for AMer cKO ESD mice.

(**R**) Histological images showing the placement of the multi-electrode in the LO&VO in the four groups. Note that the targeted regions were visualized with lipophilic dye (red) and DAPI (blue).

(A, B, E) Fourteen- and (A, C, D, G) thirty-day-old male littermates were used. (F) Fourteen-day-old-male and female littermates were used. (A-G) n values represent the number of mice per each group. Four data points were obtained from each mouse, and outliers were removed. (H-J, R) Sixteen- to eighteen-week-old male littermates were used. (K-Q) Sixteen- to eighteen-week-old female littermates were used.
Data shown as mean ± SEM. *P<0.05, **P<0.005, ***P<0.001, ****P<0.0001, ns, non-significant (P>0.05); unpaired *t*-test (F) and Two-way ANOVA with Tukey's multiple comparisons test.

Table S1. List of astrocytic phagocytosis-inhibiting FDA-approved clinical compounds, related to Figure 1

Categories	FDA-approved clinical compounds		
DNA related agents	Berberine chloride	Bleomycin	Clorgiline hydrochloride
	Luteolin	Pentamidine isethionate	
Estrogen Rc related agents	Clomiphene citrate	Mestranol	Tamoxifen citrate
Histone deacetylase	Entinostat	Vorinostat	
Neuronal channel blocker	Phenacemide	RX 821002 hydrochloride	
Neuronal Rc antagonists	Perphenazine	RO 25-6981	
Etc.	BIBX 1382 dihydrochloride	Clobenztropine	

* Rc indicates receptor